Department of Signal Processing and Acoustics

Wavefield modeling and signal processing for sensor arrays of arbitrary geometry

Mário Jorge Costa

Aalto University

DOCTORAL DISSERTATIONS

Aalto University publication series
DOCTORAL DISSERTATIONS 149/2013

Wavefield modeling and signal processing for sensor arrays of arbitrary geometry

Mário Jorge Costa

A doctoral dissertation completed for the degree of Doctor of Science in Technology to be defended, with the permission of the Aalto University School of Electrical Engineering, at a public examination held at the lecture hall S4 of the school on 1 November 2013 at 12 o'clock noon.

Aalto University
School of Electrical Engineering
Department of Signal Processing and Acoustics

Supervising professor
Academy Prof. Visa Koivunen

Thesis advisor
Academy Prof. Visa Koivunen

Preliminary examiners
Prof. Marius Pesavento, Technische Universität Darmstadt, Germany
Associate Prof. Mats Bengtsson, Kungliga Tekniska Högskolan, Sweden

Opponents
Prof. A. Lee Swindlehurst, University of California at Irvine, USA
Prof. Marius Pesavento, Technische Universität Darmstadt, Germany

Aalto University publication series
DOCTORAL DISSERTATIONS 149/2013

ISBN 978-952-60-5346-2
ISBN 978-952-60-5347-9 (pdf)
ISSN-L 1799-4934
ISSN 1799-4934 (printed)
ISSN 1799-4942 (pdf)
http://urn.fi/URN:ISBN:978-952-60-5347-9

Unigrafia Oy
Helsinki 2013

Finland

441 697
Printed matter

Aalto University

Abstract

Aalto University, P.O. Box 11000, FI-00076 Aalto www.aalto.fi

Author
Mário Jorge Costa

Name of the doctoral dissertation
Wavefield modeling and signal processing for sensor arrays of arbitrary geometry

Publisher School of Electrical Engineering

Unit Department of Signal Processing and Acoustics

Series Aalto University publication series DOCTORAL DISSERTATIONS 149/2013

Field of research Signal Processing for Communications

Manuscript submitted 7 June 2013 **Date of the defence** 1 November 2013

Permission to publish granted (date) 11 September 2013 **Language** English

☐ **Monograph** ☒ **Article dissertation (summary + original articles)**

Abstract

Sensor arrays and related signal processing methods are key technologies in many areas of engineering including wireless communication systems, radar and sonar as well as in biomedical applications. Sensor arrays are a collection of sensors that are placed at distinct locations in order to sense physical phenomena or synthesize wavefields. Spatial processing from the multichannel output of the sensor array is a typical task. Such processing is useful in areas including wireless communications, radar, surveillance and indoor positioning.

In this dissertation, fundamental theory and practical methods of wavefield modeling for radio-frequency array processing applications are developed. Also, computationally-efficient high-resolution and optimal signal processing methods for sensor arrays of arbitrary geometry are proposed. Methods for taking into account array nonidealities are introduced as well. Numerical results illustrating the performance of the proposed methods are given using real-world antenna arrays.

Wavefield modeling and manifold separation for vector-fields such as completely polarized electromagnetic wavefields and polarization sensitive arrays are proposed. Wavefield modeling is used for writing the array output in terms of two independent parts, namely the sampling matrix depending on the employed array including nonidealities and the coefficient vector depending on the wavefield. The superexponentially decaying property of the sampling matrix for polarization sensitive arrays is established. Two estimators of the sampling matrix from calibration measurements are proposed and their statistical properties are established.

The array processing methods developed in this dissertation concentrate on polarimetric beamforming as well as on high-resolution and optimal azimuth, elevation and polarization parameter estimation. The proposed methods take into account array nonidealities such as mutual coupling, cross-polarization effects and mounting platform reflections. Computationally-efficient solutions based on polynomial rooting techniques and fast Fourier transform are achieved without restricting the proposed methods to regular array geometries. A novel expression for the Cramér-Rao bound in array processing that is tight for real-world arrays with nonidealities in the asymptotic regime is also proposed.

A relationship between spherical harmonics and 2-D Fourier basis, called equivalence matrix, is established. A novel fast spherical harmonic transform is proposed, and a one-to-one mapping between spherical harmonic and 2-D Fourier spectra is found. Improvements to the minimum number of samples on the sphere that are needed in order to avoid aliasing are also proposed.

Keywords Sensor array signal processing, parameter estimation, beamforming, manifold separation, harmonic analysis, array calibration, array nonidealities

ISBN (printed) 978-952-60-5346-2 **ISBN (pdf)** 978-952-60-5347-9

ISSN-L 1799-4934 **ISSN (printed)** 1799-4934 **ISSN (pdf)** 1799-4942

Location of publisher Helsinki **Location of printing** Helsinki **Year** 2013

Pages 204 **urn** http://urn.fi/URN:ISBN:978-952-60-5347-9

Acknowledgments

Many people have contributed, either directly or indirectly, to this dissertation. The research work presented herein has been carried out under the supervision of Academy Prof. Visa Koivunen at the Department of Signal Processing and Acoustics, Aalto University (former Signal Processing Laboratory, Helsinki University of Technology) during the years 2008-2013. The statistical signal processing group is led by Prof. Koivunen and it is part of SMARAD (Smart Radios and Wireless Research), a center of excellence in research appointed by the Academy of Finland. This research work has also included an external-researcher position at the Nokia Research Center from January to July 2011.

First and foremost, I would like to express my deepest gratitude to my supervisor Academy Prof. Visa Koivunen. The guidance, constructive criticism, and technical insight that have been given by Prof. Koivunen are truly remarkable. Secondly, I would like to express my sincere gratitude to Dr. Andreas Richter for all the discussions we had. Most of these discussions were technical but some of them were less pragmatic, though still extremely helpful. Both Prof. Koivunen and Dr. Richter have provided valuable guidance and insight throughout the research work, and I have learned so much from them. Dr. Fabio Belloni is also acknowledged here for the great discussions during the course of this research. I am also indebted to Prof. Carlos Lima for all the useful advices and help in contacting Prof. Koivunen, allowing me to continue my studies in this outstanding research group. Nokia Foundation and Ulla Tuominen Foundation also deserve my gratitude for the financial support.

I would like to thank the preliminary examiners Prof. Marius Pesavento and Associate Prof. Mats Bengtsson. Their comments and suggestions have helped to improve the quality and clarity of the dissertation. The time and effort they have put in reviewing this dissertation is also highly

acknowledged.

Many thanks to my current and former colleagues at the Department of Signal Processing and Acoustics. It has been a great learning experience working with such exceptional people. They include Dr. Jussi Salmi, Dr. Traian Abrudan, Dr. Sachin Chaudhari, Dr. Alexandra Oborina, Dr. Jarmo Lunden, Dr. Jan Eriksson, Dr. Esa Ollila, Dr. Hyon-Jung Kim-Ollila, Jan Oksanen, Marian Mică, Adriana Chis, Pramod Mathecken, Taneli Riihonen, Tuomas Aittomäki, Mei-Yen Cheong, Azadeh Haghparast, Jayaprakash Rajasekharan, Hassan Naseri, among others. Dr. Stefan Werner, Prof. Risto Wichman, Prof. Sergiy Vorobyov, and Abdullah Azremi also deserve my gratitude. The help of secretaries Mirja Lemetyinen, Heidi Koponen, and Marja Leppäharju in all the bureaucratic issues is greatly appreciated. Also, special thanks to my good friends Varun Singh, Jakub Gronicz, and Javier Martinez.

My family has had an important role during these years. I thank my parents for having taught me the importance of integrity and humanistic values. My sisters deserve my gratitude for all the good advices. I also thank my uncle José Mário for his persistence in teaching me the importance, and beauty, of *língua Lusófona*. Finally, I thank Susana for helping me understanding that happiness is attained through commitment to noble ideals.

Espoo, September 19, 2013,

Mário Jorge Costa

Contents

List of publications

I M. Costa, A. Richter, F. Belloni, and V. Koivunen, "Polynomial rooting-based direction finding for arbitrary array configurations," in *Proceeding of the 5th IEEE Sensor Array and Multichannel Signal Processing Workshop (SAM)*, pp. 58-62, Darmstadt, Germany, July 21-23, 2008.

II M. Costa, A. Richter, and V. Koivunen, "Low complexity azimuth and elevation estimation for arbitrary array configurations," in *Proceeding of the IEEE International Conference on Acoustics, Speech and Signal Processing (ICASSP)*, pp. 2185-2188, Taipei, Taiwan, April 19-24, 2009.

III M. Costa, A. Richter, and V. Koivunen, "Azimuth, elevation, and polarization estimation for arbitrary polarimetric array configurations," in *Proceeding of the 15th IEEE Workshop on Statistical Signal Processing (SSP)*, pp. 261-264, Cardiff, Wales, August 31-September 3, 2009.

IV M. Costa, A. Richter, and V. Koivunen, "Unifying spherical harmonic and 2-D Fourier decompositions of the array manifold," in *Proceeding of the 43rd Asilomar Conference on Signals, Systems, and Computers*, pp. 99-103, Pacific Grove, CA, USA, November 1-4, 2009.

V M. Costa, A. Richter, and V. Koivunen, "Unified array manifold decomposition based on spherical harmonics and 2-D Fourier basis," *IEEE Transactions on Signal Processing*, vol. 58, no. 9, pp. 4634-4645, September, 2010.

VI M. Costa, A. Richter, and V. Koivunen, "Steering vector modeling for polarimetric arrays of arbitrary geometry," in *Proceeding of the 6th IEEE Sensor Array and Multichannel Signal Processing Workshop (SAM)*, pp. 265-268, Kibutz, Israel, October 4-7, 2010.

VII M. Costa, A. Richter, and V. Koivunen, "DoA and polarization estimation for arbitrary array configurations," *IEEE Transactions on Signal Processing*, vol. 60, no. 5, pp. 2330-2343, May, 2012.

VIII M. Costa and V. Koivunen, "Incorporating array nonidealities into adaptive Capon beamformer for source tracking," in *Proceeding of the 7th IEEE Workshop on Sensor Array and Multichannel Signal Processing (SAM)*, pp. 445-448, Hoboken, New Jersey, June 17-20, 2012.

List of abbreviations

AWGN	additive white Gaussian noise
BIC	Bayesian information criterion
CLSE	constrained least-squares estimator
CRB	Cramér-Rao lower bound
DF	direction-finding
DFT	discrete Fourier transform
DoA	direction-of-arrival
DoD	direction-of-departure
DSP	digital signal processor
DVSHT	discrete vector spherical harmonic transform
EADF	effective aperture distribution function
EEF	exponentially embedded families
EEG	electroencephalography
EM	electromagnetic
ES	element-space
EVD	eigenvalue decomposition
FFT	fast Fourier transform
GPS	global positioning system
GNSS	global navigation satellite systems
IEEE	Institute of Electrical and Electronics Engineers
i.i.d.	independent and identically distributed
I/Q	in-phase/quadrature
LS	least-squares
LSE	least-squares estimator
MDL	minimum description length
MEG	magnetoencephalography
MIMO	multiple-input-multiple-output
MODE	method of direction estimation

MSE	mean-squared error
ML	maximum likelihood
MLE	maximum likelihood estimator
MUSIC	multiple signal classification
NLS	nonlinear least-squares
PES	polarimetric element-space
PRIME	polynomial rooting intersection for multidimensional estimation
RARE	rank reduction estimator
RF	radio frequency
SINR	signal-to-interference-plus-noise ratio
SNR	signal-to-noise ratio
SOI	signal-of-interest
SO(3)	3-D rotation group
SVD	singular value decomposition
UCA	uniform circular array
ULA	uniform linear array
URA	uniform rectangular array
VSHT	vector spherical harmonic transform
WSF	weighted subspace fitting

List of symbols

$\hat{a}$	estimate of scalar a
a^*	complex-conjugate of scalar a
$\|a\|$	absolute-value of scalar a
$\angle a$	phase-angle of scalar a
$\lfloor a \rfloor$	nearest integer smaller than or equal to scalar a
$\boldsymbol{a}$	column vector
$[\boldsymbol{a}]_n$	nth element of vector $\boldsymbol{a}$
$[\boldsymbol{a}]_\theta$	component of vector $\boldsymbol{a}$ along the spherical unit-vector $\boldsymbol{e}_\theta$
$[\boldsymbol{a}]_\phi$	component of vector $\boldsymbol{a}$ along the spherical unit-vector $\boldsymbol{e}_\phi$
$\|\boldsymbol{a}\|$	Euclidean norm of vector $\boldsymbol{a}$
$\|\boldsymbol{a}\|_1$	ℓ_1-norm of vector $\boldsymbol{a}$
$\mathrm{FFT}\{\boldsymbol{a}\}$	FFT of vector $\boldsymbol{a}$
$\mathrm{IFFT}\{\boldsymbol{a}\}$	inverse FFT of vector $\boldsymbol{a}$
$\mathrm{diag}\{\boldsymbol{a}\}$	diagonal matrix composed of elements in vector $\boldsymbol{a}$
$\boldsymbol{A}$	matrix
$\boldsymbol{A}^{-1}$	inverse of matrix $\boldsymbol{A}$
$\boldsymbol{A}^T$	transpose of matrix $\boldsymbol{A}$
$\boldsymbol{A}^H$	conjugate-transpose of matrix $\boldsymbol{A}$
$\boldsymbol{A}^\dagger$	Moore-Penrose pseudo-inverse of matrix $\boldsymbol{A}$
$[\boldsymbol{A}]_{m,n}$	(m,n)th element of matrix $\boldsymbol{A}$
$\mathrm{tr}(\boldsymbol{A})$	trace of matrix $\boldsymbol{A}$
$\det(\boldsymbol{A})$	determinant of matrix $\boldsymbol{A}$
$\mathrm{vec}(\boldsymbol{A})$	stacks the elements of matrix $\boldsymbol{A}$ on a vector
$\mathcal{R}\{\boldsymbol{A}\}$	row-space of matrix $\boldsymbol{A}$
$\|\boldsymbol{A}\|_F$	Frobenius norm of matrix $\boldsymbol{A}$

$\boldsymbol{A} \otimes \boldsymbol{B}$	Kronecker product of matrices $\boldsymbol{A}$ and $\boldsymbol{B}$
$\boldsymbol{A} \odot \boldsymbol{B}$	Hadamard-Schur product of matrices $\boldsymbol{A}$ and $\boldsymbol{B}$
$\boldsymbol{I}_n$	n-dimensional identity matrix
$\boldsymbol{0}$	matrix of zeros with appropriate dimensions
j	imaginary unit
$J_m(\cdot)$	Bessel function of the first kind and order m
$j_\ell(\cdot)$	spherical Bessel function of the first kind and order ℓ
k	discrete time index
K	number of snapshots
L	highest level index
N	number of array elements
M	highest mode index
P	number of sources
Q	number of samples on the 2-sphere
Q_a	number of samples in azimuth
Q_e	number of samples in co-elevation
t	continuous time index
$\mathcal{A}$	array manifold
$\mathbb{C}$	set of complex numbers
$\mathbb{E}\{\cdot\}$	expectation operator
$\mathcal{H}$	(infinite dimensional) Hilbert sequence space ℓ^2
$\mathcal{L}$	number of vector spherical harmonic coefficients
$\mathcal{M}$	number of modes
$\mathbb{N}$	set of natural numbers
$\mathbb{R}$	set of real numbers
$\mathcal{S}^1$	domain of a circle
$\mathcal{S}^2$	domain of a sphere
β	polarization parameter
γ	polarization parameter
$\delta(\cdot)$	Dirac delta
ϑ	co-elevation angle
κ	angular wavenumber
λ	wavelength
σ^2	measurement noise power
σ^2_{cal}	calibration measurement noise power
τ	time delay
φ	azimuth angle

1. Introduction

1.1 Motivation

Sensor arrays and related signal processing methods are employed in many areas of engineering, including advanced wireless communication systems such as multiple-input-multiple-output (MIMO) systems [13, 49, 113, 130, 137], radar systems for both military and civilian applications such as remote sensing [75, 103], radio astronomy and cosmology [17, 89, 177], as well as in global navigation satellite systems (GNSSs) and indoor positioning [8, 54, 70]. Measurement based modeling of the radio propagation channel as well as of the acoustic and underwater channels also employ sensor arrays [81, 84, 125, 131]. Sensor arrays are also used in biomedical measurement systems such as electroencephalography (EEG) and magnetoencephalography (MEG), in surveillance systems and in geophysical exploration [20].

Sensor arrays are a collection of sensors that are placed at distinct locations in order to sense physical phenomena and synthesize fields. Passive sensor arrays may observe propagating wavefields while active arrays may transmit energy and generate a desired wavefield. For example, sensing an electromagnetic wavefield with an antenna array may provide information regarding the location of radiating sources relative to the antenna array. Similarly, the polarization of the sources generating the wavefield may be estimated by employing antenna arrays. The angular direction of the sources relative to the antenna array is known as direction-of-arrival (DoA) and may be used for enhancing signals and attenuating interferers from a particular direction. Antenna arrays may also enhance desired signals or cancel interference based on the polarization state of the Electric-field or use polarization as a source of diversity.

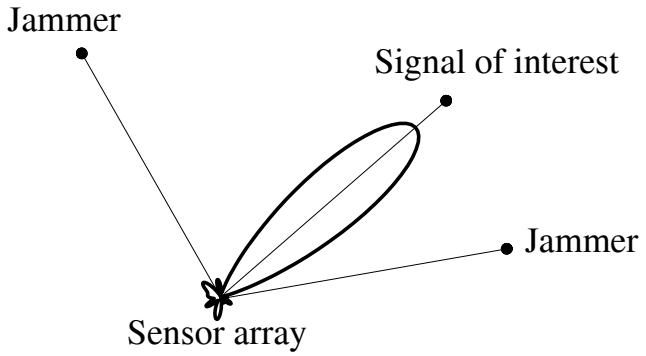

Figure 1.1. Illustration of a beamforming example.

These tasks based on directional and polarimetric information are known as polarimetric receive beamforming. Transmit beamforming aims at synthesizing fields using antenna arrays such that the transmitted signals may be coherently combined at the location and polarization of the receivers while attenuating the signals in undesired directions. Figure 1.1 illustrates a beamforming example.

Array processing methods typically require information regarding the array manifold. The array manifold may be understood as the overall characterization of the response of the antenna array system in sensing and generating wavefields. The following ideal simplifying assumptions are commonly made in the array processing literature, since they make the derivation and analysis of signal processing methods more tractable:

- The antenna array geometry is known, namely the relative placements and phase-centers of the antennas composing the array are known exactly.

- The array elements have omnidirectional beampatterns and are free from interactions among neighboring elements, the platform where the array is mounted as well as from the array structure.

The above assumptions are often too simplistic in real-world sensor array systems and applications. For example, omnidirectional antennas are not physically realizable [65], and each array element has an individual directional beampattern. Antenna arrays are also subject to complex electromagnetic interactions among the array elements and mounting platform. These nonidealities include mutual coupling, cross-polarization effects, and mounting platform reflections. The phase-centers of array el-

ements may be displaced from their intended locations because of nonidealities. Phase-centers of the array elements provide the relative phase information of a sensor array that is needed in DoA estimation and beamforming. Array processing methods that rely on the ideal assumptions listed above typically experience a loss of performance. For example, such a sensor array may receive signals from undesired directions and transmit excessive energy. Array processing methods may not be able to attenuate intentional or unintentional interference and may even cancel the desired signals. When the sensor array is used for parameter estimation, the estimates of the DoA and polarization of the sources may be biased and have excess variance when the array nonidealities are not taken into account.

1.2 Objectives and scope

The first objective of this dissertation is to develop fundamental theory and derive practical methods of wavefield modeling for electromagnetic based array processing applications. By employing wavefield modeling and manifold separation principle, the wavefield dependent part may be decoupled from the array dependent part in the employed signal model. Particular attention is given to array calibration measurements in developing practical methods of wavefield modeling. The focus is on antenna arrays and radio-frequency signals. Scalar-fields such as acoustic pressure and microphone arrays may be seen as a special case of the more general vector-field model. The second objective is to develop high-resolution and optimal array processing methods that are based on wavefield modeling for diversely polarized antenna arrays and electromagnetic wavefields. Emphasis is given to processing in the elevation, azimuth, and polarimetric domains. Note that processing of scalar-fields may be seen as a special case of the more general scenario considered in this dissertation. The proposed signal processing methods may not rely on the specific array geometry in achieving computationally-efficient implementations. Solutions based on the fast Fourier transform and polynomial rooting techniques are particularly desirable. Moreover, the proposed methods should take into account array nonidealities such as mutual coupling, cross-polarization effects, and elements' misplacements. Antenna arrays with individual directional beampatterns that may not be described in a closed-form should also be taken into account by the proposed array processing methods.

1.3 Contributions

This dissertation contributes to the areas of array signal processing, wavefield modeling and harmonic analysis (on the sphere). The contributions are the following:

- Wavefield modeling and manifold separation for vector-fields including completely polarized electromagnetic wavefields are proposed. Vector spherical harmonics are employed since they are orthogonal on the sphere and do not require sector-by-sector processing. The superexponential decay of the array sampling matrix is also established. Such a result shows that a few vector spherical harmonics describe most of the characteristics of diversely polarized antenna arrays, including nonidealities. These results are general in the sense that they include scalar-fields such as acoustic pressure and microphone arrays as special cases.

- Two estimators of the sampling matrix from array calibration measurements are proposed. The Cramér-Rao Bound (CRB) for the corresponding problem is established as well. The estimators are based on least-squares method and discrete vector spherical harmonic transform. Their statistical properties are established and compared to the CRB.

- A simple closed-form expression for the stochastic CRB in array processing that is based on manifold separation for vector-fields is proposed. The proposed bound is exact for ideal arrays such as uniform rectangular arrays and tight for real-world arrays with nonidealities at high SNR regime.

- A novel relationship among vector spherical harmonics and 2-D Fourier basis that is called equivalence matrix is established. The equivalence matrix provides a bijective mapping between vector spherical harmonic spectra and 2-D Fourier spectra. Wavefield modeling and manifold separation are reformulated in terms of 2-D Fourier basis using the equivalence matrix. The use of 2-D Fourier basis facilitates deriving computationally efficient array processing methods.

- A novel fast spherical harmonic transform that is based on the equivalence matrix is proposed. The proposed method employs the fast Fourier

transform in both elevation and azimuth angles. Improvements to well-known equiangular sampling rules on the sphere are also proposed. A reduction of the minimum number of samples in order to avoid aliasing is achieved.

- High-resolution and optimal array processing methods are extended to elevation, azimuth, and polarimetric domains using wavefield modeling. The proposed methods do not rely on the array geometry in order to exploit the convenient Vandermonde structure of Fourier basis. In addition, they take into account array nonidealities. In particular, the proposed methods are extensions of the Capon beamformer, MUSIC and root-MUSIC methods, and weighted subspace fitting (WSF) technique. Computationally-efficient implementations of the proposed methods based on the fast Fourier transform and polynomial rooting techniques are proposed.

1.4 Dissertation structure

This dissertation consists of an introductory part and eight original publications. The introductory part provides on overview of the work in publications I–VII and a survey of the state-of-the-art of the topics considered in this thesis. The introductory part also includes novel results that are not available in the original publications. These are given in the appendix and explained in detail in the introductory part.

This dissertation is organized as follows. In Chapter 2, ideal sensor arrays commonly used in signal processing are briefly described, and the real-world antenna arrays employed in this work are shown. The signal model used in array processing and related assumptions are also provided.

Chapter 3 provides a review of the most relevant techniques for dealing with array nonidealities. Auto-calibration techniques and robust methods based on uncertainty sets are briefly described. Array calibration measurements and array mapping techniques such as array interpolation and beamspace transform are also reviewed. A summary of wavefield modeling and manifold separation is also given.

Chapter 4 is dedicated to wavefield modeling and manifold separation. The equivalence matrix is described in detail as well. The emphasis is

on elevation and azimuth processing for vector-fields such as completely polarized electromagnetic wavefields. The state-of-the-art of fast computational methods for harmonic analysis on the sphere is also described and novel results are established. An illustrative example of a typical array calibration task is provided.

In Chapter 5, high-resolution and optimal array processing methods are extended to arrays of arbitrary geometry by incorporating wavefield modeling and manifold separation for completely polarized electromagnetic wavefields. Emphasis is given to receive beamforming and subspace methods. The proposed array processing methods may be implemented in a computationally-efficient manner using the fast Fourier transform and polynomial rooting methods regardless of the array geometry and nonidealities. A simple closed-form expression for the stochastic CRB in array processing that is tight in the high SNR regime for real-world arrays with nonidealities is also provided. Numerical examples of typical array processing tasks are included.

Chapter 6 provides the concluding remarks and future work. The appendix includes details on novel results that are not available in the original publications. In particular, improvements to the minimum number of samples on the sphere that are needed in order to avoid aliasing are proposed. Results showing that discrete vector spherical harmonic transforms employing equiangular sampling schemes may be implemented using the 2-D fast Fourier transform are established as well. Publications I–VII can be found in the appendix.

1.5 Summary of the publications

A brief overview of the original publications [I–VII] is given next.

In Publication I, a generalization of the beamspace transform using manifold separation is proposed. The proposed mapping technique is not restricted to uniform circular arrays, unlike the original beamspace transform [100], and avoids sector-by-sector processing as opposed to array interpolation based on virtual arrays [40]. The polynomial rooting based weighted subspace fitting method [164], also known as MODE [148, 149], is extended to arbitrary array geometries by using the proposed mapping technique.

In Publication II, manifold separation based on 2-D Fourier basis is employed in order to derive computationally-efficient methods for azimuth

and elevation angle estimation. The polynomial rooting intersection for multidimensional estimation (PRIME) method [56,57] is extended to sensor arrays of arbitrary geometry, including conformal arrays. The proposed method, called element-space PRIME, provides automatically paired azimuth and elevation angle estimates. The estimates obtained by using the ES-PRIME method are refined by an extension of the weighted subspace fitting (WSF) method. The proposed ES-WSF method employs closed-form derivatives of the azimuth and elevation angles even for real-world sensor arrays with nonidealities. This is useful in gradient-based optimization methods as well as in establishing performance bounds.

In Publication III, manifold separation for vector-fields using 2-D Fourier basis is employed in order to derive a novel MUSIC method for joint elevation, azimuth, and polarization parameter estimation. The proposed method employs a 2-D fast Fourier transform based line search regardless of the array geometry and nonidealities, including conformal arrays. In case that the elevation angle of the sources is known, azimuth angles and polarization parameters may be found by polynomial rooting. Alternatively, the elevation angles of the sources may be found from the roots of a polynomial by holding the azimuth angles fixed. Therefore, the proposed method may be seen as an extension of the root-MUSIC method to sensor arrays of arbitrary geometries and polarimetric domain.

In Publication IV, a novel mapping called equivalence matrix is proposed. The emphasis is on scalar-fields such as acoustic pressure. It is shown that the equivalence matrix establishes a connection between (scalar) spherical harmonics and 2-D Fourier basis. A one-to-one mapping between spherical harmonic spectra and 2-D Fourier spectra is also established using the equivalence matrix. It is shown that decomposing the array steering vector in terms of spherical harmonics or 2-D Fourier basis achieves the same modeling accuracy.

In Publication V, a detailed analysis of the equivalence matrix and its properties in the context of array processing for scalar-fields is conducted. Recurrence expressions for finding the equivalence matrix are proposed. It is shown that the equivalence matrix is independent of the sensor array and it may be computed once in an offline manner, stored, and used when needed by appropriate selection of its columns and rows. The equivalence matrix is also shown to be sparse, and an upper-bound on the number of nonzero entries is established. A novel fast spherical harmonic transform that is based on the equivalence matrix and 2-D FFT is proposed.

The rows of the 2-D Fourier spectrum of the "full-periodic" array steering vector are shown to span the row-space of the equivalence matrix. Such a result allows for a reduction of the estimation variance of the 2-D effective aperture distribution function (EADF).

In Publication VI, wavefield modeling and manifold separation are extended to vector-fields such as completely polarized electromagnetic waves and diversely polarized antenna arrays. The equivalence matrix and the mapping it provides is also extended to vector-fields. It is shown that the equivalence matrix establishes a connection between vector spherical harmonics and 2-D Fourier basis. A bijective mapping between vector spherical harmonic spectra and 2-D Fourier spectra using the equivalence matrix is also established. It is shown that wavefield modeling and manifold separation may be formulated in terms of vector spherical harmonics or 2-D Fourier basis with identical accuracy.

In Publication VII, array processing methods for elevation and azimuth angles, and polarization estimation are proposed. The proposed methods are based on manifold separation for vector-fields and equivalence matrix. They extend the MUSIC method, noise subspace fitting as well as the signal subspace fitting technique for polarization sensitive antenna arrays with nonidealities. The proposed methods exploit the convenient Vandermonde structure of 2-D Fourier basis in order to reduce their computational complexity. A novel expression for the stochastic CRB in array processing that is based on manifold separation is derived. The proposed bound is appropriate for assessing the limiting performance of real-world antenna arrays with nonidealities in the high SNR regime.

In Publication VIII, a novel Capon beamformer based on manifold separation is proposed. The proposed method is based on inverse QR-updates and finds the azimuth angles of the sources from the roots of a real-valued polynomial. The proposed Capon method is appropriate for source tracking since one may employ computationally-efficient root-tracking methods for real-valued polynomials. This is useful in tracking airplanes, vessels or mobile users in indoor environments, for example.

The author of this dissertation is responsible for the theoretical and numerical results in all the publications, including programming related tasks and writing process. The co-authors have provided valuable guidance and insight throughout the research work as well as in writing and structuring the publications. The generalized beamspace transform based on manifold separation proposed in Publication I was suggested by the co-

authors.

2. Array processing models

In array signal processing one is typically interested in characterizing, synthesizing, enhancing or attenuating certain aspects of propagating wavefields by employing a collection of sensors, known as a *sensor array*. Characterizing a propagating wavefield refers to determining its *spatial spectrum*, i.e. the angular distribution of energy, so that information regarding the location of the sources generating the wavefield can be obtained, for example [143]. Synthesizing or producing a wavefield refers to generating a propagating wavefield with a desired spatial spectrum in order to focus the transmitted energy towards certain locations in space. Finally, attenuating or enhancing a received wavefield based on its spatial spectrum refers to the ability of canceling interfering sources or improving the signal-to-interference-plus-noise ratio (SINR) and maximizing the energy received from certain directions.

The propagating wavefield is typically parameterized by the angular location of sources generating such a wavefield, their polarization state, bandwidth, delay profile and Doppler shift [2, 125]. The angular parameterization of the propagating wavefield is commonly known as the directions-of-arrival (DoAs) or directions-of-departure (DoDs), and characterizes the spatial spectrum of the wavefield received or transmitted by the sensor array, respectively.

In addition to the propagating wavefield, a model describing the response of the sensor array as a function of the angular location of the sources is typically required in array processing. Such a model is known as *array steering vector* and allows us to estimate the DoAs from data acquired by the sensor array, for example. Similarly, steering vectors are used to synthesize a desired wavefield and employ transmit beamforming techniques.

This chapter includes the signal model, describing the wavefield re-

ceived by a sensor array, that is commonly used in array processing as well as related assumptions. Typical steering vector models found in the array processing literature are also provided. Emphasis is given to the limitations of such ideal array models in describing common nonidealities that are found in real-world arrays.

2.1 Signal model

Consider that a propagating electromagnetic (EM) wavefield is generated by $P \in \mathbb{N}$ radiating sources and received by an array composed of $N \in \mathbb{N}$ EM sensors. Examples of EM sensors include Electric and Magnetic dipoles, loop antennas as well as patch (also known as microstrip) antennas. The radiating sources are assumed to be point emitters in the sense that the field radiated by each source can be assumed to have origin at a single location. Furthermore, the radiating sources are assumed to be located in the far-field region of the employed sensor array. In particular, the curvature of the propagating wavefield across the array aperture may be neglected and the radial component of the Electric-field is negligible compared to its tangential components [55]. This corresponds to plane wave assumption where the delays (and attenuation) experienced by the wavefront among array elements suffice in determining the angular location of the sources. Finally, the propagation medium is assumed to be linear in the sense that the superposition principle holds as well as homogeneous.

The signals transmitted by the sources generating the propagating wavefield are assumed to be narrowband in the sense that the signals' bandwidth B_s is "small" compared to the inverse of the propagation time τ of the wavefield across the array aperture. This means that the delays experienced by the signals across the array aperture are not frequency dependent. A common rule of thumb is based on the time-bandwidth product $B_s\tau$ [74]. In particular, narrowband in array processing may be defined when $\mathrm{sinc}(B_s\tau) \approx 1$ [141] [67, Ch.4]. The physical dimension of the sensor array is known as array aperture and it is typically measured in wavelengths λ. The effective aperture of a sensor array refers to the projection of the array aperture onto a line perpendicular to the direction vector, denoted by $\boldsymbol{\kappa} \in \mathbb{R}^{3\times 1}$. Figure 2.1 illustrates a typical array processing task.

The angular location of the sources relative to the employed sensor array is known as direction-of-arrival (DoA). Under the above assumptions,

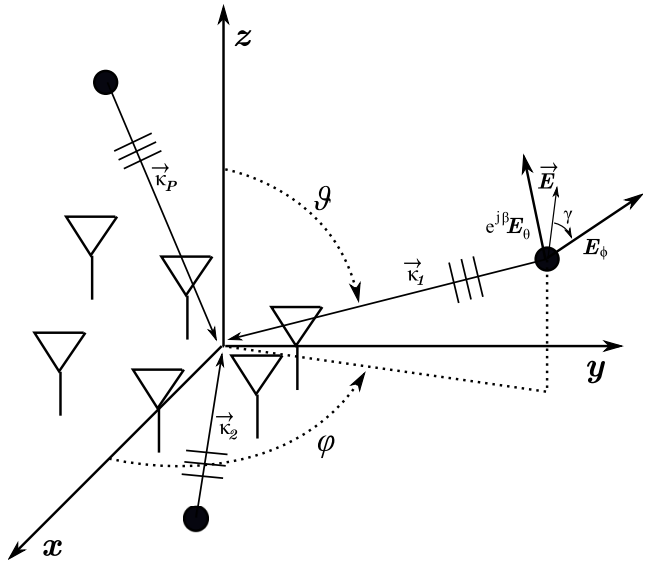

Figure 2.1. Illustration of the array processing task considered in this research work.

the DoAs of the sources may be obtained from the spatial spectrum of the EM wavefield received by a sensor array. Conversely, receivers equipped with a single antenna may determine its location relative to a transmitting array when the array response is known at the receivers. Such a task is called direction-of-departure (DoD) estimation and finds applications in measurement based radio channel modeling as well as in indoor positioning [8, 70, 125, 133]. Despite the focus of this work being on DoA estimation and beamforming, the array models discussed herein and the contributions presented in chapters 4 and 5 are applicable for DoD estimation as well.

In case of receiving arrays, each source generating the propagating EM wavefield is characterized by a co-elevation and azimuth angles, denoted by $\vartheta \in [0, \pi]$ and $\varphi \in [0, 2\pi)$, as well as by the polarization state of the transmitted Electric-field. Polarization is a source of diversity for wireless communications and radar. It may be used for target identification since the state of the Electric-field changes depending on scatterers composing the reflecting surface [60]. Polarization also provides robustness against jammers in GNNSs by matching the receiving array to the polarization state of the Electric-field transmitted by satellites. In the far-field, any polarization state may be described by the relative magnitude and phase angle between the orthogonal tangential components of the Electric-field,

namely [26]:

$$\gamma = \arctan\left(\frac{|\boldsymbol{E}_\phi(\vartheta,\varphi)|}{|\boldsymbol{E}_\theta(\vartheta,\varphi)|}\right), \quad \beta = \angle\left(\frac{\boldsymbol{E}_\phi(\vartheta,\varphi)}{\boldsymbol{E}_\theta(\vartheta,\varphi)}\right), \tag{2.1}$$

where $\gamma \in [0, \pi/2]$ and $\beta \in [0, 2\pi)$ parameterize the polarization ellipse of the Electric-field. Angles and polarization parameters of the P sources generating the propagation wavefield are called *wavefield parameters*, and may be collected in vector $\boldsymbol{\xi} \in \mathbb{R}^{4P\times 1}$ as $\boldsymbol{\xi} = [\boldsymbol{\vartheta}^T, \boldsymbol{\varphi}^T, \boldsymbol{\gamma}^T, \boldsymbol{\beta}^T]^T$. The parameterization of the polarization state of the Electric-field using (2.1) is sometimes called Jones vector representation. Alternatively, one may describe the polarization of the Electric-field by parameterizing the polarization ellipse using the so-called ellipticity and orientation angles [104,105]. Both representations are related in a bijective manner [26].

In this work the polarization state of the Electric-field is assumed to be a deterministic unknown quantity, as opposed to the random zero-mean complex Gaussian assumption used in [61,91]. The latter approach is motivated by the central limit theorem and convenient in array processing methods when polarization can be assumed to be wide-sense stationary. The approach taken herein is usually preferred when no assumptions regarding the probability distribution of the polarization state can be made but requires the polarization state to remain fixed when estimating the array covariance matrix.

Assume that the typical nonidealities of receiver front-ends, such as I/Q-imbalances and nonlinear distortion of low-noise amplifiers, are either negligible compared with sensor noise variance or have been compensated for [107, 161]. Then, the baseband discrete-time representation of the array output at the kth time instant is a multivariate observation $\boldsymbol{x}(k) \in \mathbb{C}^{N\times 1}$ known as *snapshot* and may be modeled as:

$$\boldsymbol{x}(k) = \boldsymbol{A}(\boldsymbol{\vartheta},\boldsymbol{\varphi},\boldsymbol{\gamma},\boldsymbol{\beta})\boldsymbol{s}(k) + \boldsymbol{n}(k), \tag{2.2}$$

where $\boldsymbol{s}(k) \in \mathbb{C}^{P\times 1}$ and $\boldsymbol{n}(k) \in \mathbb{C}^{N\times 1}$ denote the transmitted signals and sensor noise, respectively. In (2.2), $\boldsymbol{A}(\boldsymbol{\vartheta},\boldsymbol{\varphi},\boldsymbol{\gamma},\boldsymbol{\beta}) \in \mathbb{C}^{N\times P}$ is known as *array steering matrix* and contains the (noise-free) array responses to the P sources generating the wavefield as follows:

$$\boldsymbol{A}(\boldsymbol{\vartheta},\boldsymbol{\varphi},\boldsymbol{\gamma},\boldsymbol{\beta}) = [\boldsymbol{a}(\vartheta_1,\varphi_1,\gamma_1,\beta_1),\ldots,\boldsymbol{a}(\vartheta_P,\varphi_P,\gamma_P,\beta_P)]. \tag{2.3}$$

In (2.3), $\boldsymbol{a}(\vartheta,\varphi,\gamma,\beta) \in \mathbb{C}^{N\times P}$ is known as *array steering vector* and it describes the array response as a function of the wavefield parameters. The collection of array steering vectors over the entire parameter space is

known as *array manifold* $\mathcal{A}$, and it is given by:

$$\mathcal{A} = \{\boldsymbol{a}(\vartheta, \varphi, \gamma, \beta) \mid \varphi, \beta \in [0, 2\pi),\ \vartheta \in [0, \pi],\ \gamma \in [0, \pi/2]\}\,. \tag{2.4}$$

Let $\boldsymbol{a}_\phi(\vartheta, \varphi) \in \mathbb{C}^{N\times 1}$ denote the array steering vector due to a polarized wavefield given by $\boldsymbol{E}_\phi(\vartheta, \varphi)$. Similarly, let $\boldsymbol{a}_\theta(\vartheta, \varphi) \in \mathbb{C}^{N\times 1}$ denote the steering vector due to $\boldsymbol{E}_\theta(\vartheta, \varphi)$. Vectors $\boldsymbol{E}_\phi(\vartheta, \varphi) \in \mathbb{C}^{2\times 1}$ and $\boldsymbol{E}_\theta(\vartheta, \varphi) \in \mathbb{C}^{2\times 1}$ denote an Electric-field with a component along one of the spherical unit-vectors $\boldsymbol{e}_\phi$ and $\boldsymbol{e}_\theta$, respectively. Figure 2.1 illustrates that $\boldsymbol{E}_\phi(\vartheta, \varphi)$ and $\boldsymbol{E}_\theta(\vartheta, \varphi)$ may be understood as an horizontally and vertically polarized wavefield when the signal sources lie in the xy-plane. In particular, the array steering vector in the far-field may be written as follows:

$$\boldsymbol{a}(\vartheta, \varphi, \gamma, \beta) = \boldsymbol{a}_\phi(\vartheta, \varphi) v_\phi(\gamma) + \boldsymbol{a}_\theta(\vartheta, \varphi) v_\theta(\gamma, \beta), \tag{2.5}$$

where the polarization is described by $v_\phi(\gamma) = \cos(\gamma)$ and $v_\theta(\gamma, \beta) = \sin(\gamma)\mathrm{e}^{\mathrm{j}\beta}$.

The array steering matrix in (2.3) can then be written as:

$$\boldsymbol{A}(\boldsymbol{\vartheta}, \boldsymbol{\varphi}, \boldsymbol{\gamma}, \boldsymbol{\beta}) = \Big[\boldsymbol{A}_\phi(\boldsymbol{\vartheta}, \boldsymbol{\varphi}),\quad \boldsymbol{A}_\theta(\boldsymbol{\vartheta}, \boldsymbol{\varphi})\Big]\, \boldsymbol{V}(\boldsymbol{\gamma}, \boldsymbol{\beta}), \tag{2.6}$$

where $\boldsymbol{A}_\phi(\boldsymbol{\vartheta}, \boldsymbol{\varphi}) \in \mathbb{C}^{N\times P}$ and $\boldsymbol{A}_\theta(\boldsymbol{\vartheta}, \boldsymbol{\varphi}) \in \mathbb{C}^{N\times P}$ contain the array responses to an horizontally and vertically polarized wavefield, respectively. Moreover, matrix $\boldsymbol{V}(\boldsymbol{\gamma}, \boldsymbol{\beta}) \in \mathbb{C}^{2P\times P}$ is given by $\boldsymbol{V}(\boldsymbol{\gamma}, \boldsymbol{\beta}) = [\boldsymbol{V}_\phi(\boldsymbol{\gamma}), \boldsymbol{V}_\theta(\boldsymbol{\gamma}, \boldsymbol{\beta})]^T$, and contains the polarization parameters as:

$$\boldsymbol{V}_\phi(\boldsymbol{\gamma}) = \operatorname{diag}\left\{\cos(\gamma_1),\ \ldots,\ \cos(\gamma_P)\right\}, \tag{2.7a}$$

$$\boldsymbol{V}_\theta(\boldsymbol{\gamma}, \boldsymbol{\beta}) = \operatorname{diag}\left\{\sin(\gamma_1)\mathrm{e}^{\mathrm{j}\beta_1},\ \ldots,\ \sin(\gamma_P)\mathrm{e}^{\mathrm{j}\beta_P}\right\}. \tag{2.7b}$$

The employed sensor array is assumed to be *unambiguous* in the sense that any matrices $\boldsymbol{A}_\phi(\boldsymbol{\vartheta}, \boldsymbol{\varphi})$ and $\boldsymbol{A}_\theta(\boldsymbol{\vartheta}, \boldsymbol{\varphi})$ are full column-rank, and that $\boldsymbol{a}_\phi(\vartheta, \varphi) \neq \boldsymbol{a}_\theta(\vartheta, \varphi),\ \forall(\vartheta, \varphi)$ [85, 155].

Throughout this research work, sensor noise $\boldsymbol{n}(k)$ in (2.2) is assumed to be zero-mean complex-circular Gaussian distributed $\mathcal{N}_c(\boldsymbol{0}, \sigma^2\boldsymbol{I}_N)$. The transmitted signals $\boldsymbol{s}(k)$ are modeled as random vectors obeying a zero-mean complex-circular Gaussian distribution $\mathcal{N}_c(\boldsymbol{0}, \boldsymbol{R}_s)$. The signal covariance matrix $\boldsymbol{R}_s \in \mathbb{C}^{P\times P}$ has rank $P'(P' \leq P)$, which may be due to specular multipath propagation or correlated source signals. In particular, if the delay between two signal replicas is larger than the coherence time of the propagation channel then the received signals may be considered uncorrelated, otherwise they are typically fully correlated. In the latter case, the received signals are called *coherent*.

The array signal model in (2.2) is known as conditional or unconditional model depending whether the transmitted signals are modeled as unknown deterministic or random quantities, respectively. From an optimality viewpoint the unconditional model is usually preferred since one can derive asymptotically optimal estimators of the wavefield parameter vector $\boldsymbol{\xi}$ that achieve the unconditional Cramér-Rao lower Bound (CRB) [109,146]. The CRB is a lower bound on the estimation variance of any unbiased estimator, and may be understood as a benchmark for comparing the statistical performance of unbiased estimators [69]. Asymptotically unbiased estimators that achieve the CRB are called asymptotically statistically efficient. The conditional CRB is typically too optimistic and, in general, no estimator can achieve it [146]. This follows from the fact that, under the conditional signal model, the number of unknown parameters grows with snapshots. Thus, asymptotically efficient estimators of $\boldsymbol{\xi}$ may be found when the number of array elements grows as well [144]. Details on asymptotically statistically efficient methods and CRB are given in Chapter 5.

Assuming wide-sense stationarity of the array output in (2.2), the array covariance matrix $\boldsymbol{R}_x \in \mathbb{C}^{N\times N}$ is given by

$$\boldsymbol{R}_x = \boldsymbol{A}(\boldsymbol{\xi})\boldsymbol{R}_s\boldsymbol{A}^H(\boldsymbol{\xi}) + \sigma^2\boldsymbol{I}_N. \tag{2.8}$$

The spatially white noise assumption in (2.8) implies that the noise term in the array output (2.2) is not affected by sensors' gains. Such a scenario is known as *internally noise limited*, as opposed to the externally noise limited assumption where sensors' beampatterns affect both the received signals and interfering spatial field [4]. In the latter case, (2.8) may still be employed by means of pre-whitening, given that the second-order statistics of the interfering spatial field are known [153]. A necessary condition for identifiability of the wavefield parameter vector $\boldsymbol{\xi}$ from (2.8) is $P \leq NP'/(P'+2)$ [61, 155]. Such an assumption is taken in the remainder of this work. In practice, the theoretical covariance matrix in (2.8) is unknown and it is typically estimated from a collection of $K \in \mathbb{N}$ array snapshots as:

$$\hat{\boldsymbol{R}}_x = \frac{1}{K}\sum_{k=1}^{K}\boldsymbol{x}(k)\boldsymbol{x}(k)^H. \tag{2.9}$$

Most of array processing tasks such as beamforming as well as DoA and polarization estimation employ the sample array covariance matrix in (2.9). Such array processing methods are addressed in detail in Chapter 5. In particular, the wavefield parameter vector $\boldsymbol{\xi}$ may be estimated from

the spatial spectrum of the received wavefield by employing beamforming techniques, similarly to a spectrum estimation problem [143]. Such an approach is called *nonparametric* since it does not rely on the assumptions taken above regarding the sources generating the propagating wavefield, including the point-source assumption. Typically, the classification parametric/nonparametric in array processing refers to whether a technique employs a finite dimensional parametric model describing the spatial distribution of power of the wavefield. This is similar to spectral estimation since the spatial distribution of power may be understood as a spatial spectrum [143]. Nonparametric techniques in array processing are versatile but typically have poor *resolution* (in particular for arrays with small apertures, relative to the wavelength) and lead to suboptimal estimates of the wavefield parameter vector $\boldsymbol{\xi}$. Informally, resolution refers to the ability of distinguishing between two closely spaced sources [67, 80]. The resolution of beamforming techniques is limited by the array aperture in wavelengths as well as SNR (or SINR) and does not improve with increasing number of array snapshots [67, Ch. 3], [80].

The resolution limit imposed by the array aperture may be improved by assuming a particular model for the spatial spectrum of the wavefield. One such a model employs the point-source assumption and assumes that the wavefield's spatial distribution of power is described by a *line* spectrum. It is further assumed that the number of signals P as well as the rank P' of the signal covariance matrix are known or have been correctly estimated from the array output, and that the necessary conditions for identifiability of the wavefield parameter vector described above are satisfied [169, 171]. Then, the array output in (2.2) obeys the so-called *low-rank* signal model and the array covariance matrix in (2.8) may be written as [80]:

$$\boldsymbol{R}_x = \boldsymbol{U}_s \boldsymbol{\Lambda}_s \boldsymbol{U}_s^H + \boldsymbol{U}_n \boldsymbol{\Lambda}_n \boldsymbol{U}_n^H. \tag{2.10}$$

Here, $\boldsymbol{U}_s \in \mathbb{C}^{N \times P'}$ and $\boldsymbol{U}_n \in \mathbb{C}^{N \times (N-P')}$ contain the eigenvectors of $\boldsymbol{R}_x$ spanning the so-called signal and noise subspaces while $\boldsymbol{\Lambda}_s \in \mathbb{R}^{P' \times P'}$ and $\boldsymbol{\Lambda}_n \in \mathbb{R}^{(N-P') \times (N-P')}$ contain the corresponding eigenvalues on their diagonal. Techniques employing the low-rank signal model in (2.10) are called subspace methods and are a class of high-resolution DoA estimation algorithms [80]. They exploit the fact that the columns of $\boldsymbol{U}_s$ span the same subspace as the columns of $\boldsymbol{A}(\boldsymbol{\xi})$ (in the case of coherent signals $\boldsymbol{U}_s$ is contained in the subspace spanned by the columns of $\boldsymbol{A}(\boldsymbol{\xi})$), and that both $\boldsymbol{U}_s$ and $\boldsymbol{A}(\boldsymbol{\xi})$ are orthogonal to the noise subspace $\boldsymbol{U}_n$. Unlike beamforming

techniques, the resolution of subspace methods improves with increasing number of array snapshots. A low-rank decomposition similar to (2.10) can also be found for the sample covariance matrix as follows:

$$\hat{\boldsymbol{R}}_x = \hat{\boldsymbol{U}}_s \hat{\boldsymbol{\Lambda}}_s \hat{\boldsymbol{U}}_s^H + \hat{\boldsymbol{U}}_n \hat{\boldsymbol{\Lambda}}_n \hat{\boldsymbol{U}}_n^H. \tag{2.11}$$

Asymptotically optimal DoA estimation algorithms such as the stochastic maximum likelihood estimator, and beamforming techniques such as the Capon beamformer, are often very sensitive to uncertainties in the array steering vector model and sensor noise (and interferers) statistics [46, 163]. Optimal DoA estimators are subject to bias and increased variance while optimum beamformers may suffer from signal-of-interest (SOI) cancellation effects. Uncertainty in noise statistics may be due to outliers, i.e. observations that do not follow the same pattern as the majority of the data, or invalid assumptions on the noise distribution [183]. For example, man-made interference has typically a non-Gaussian heavy-tailed distribution, under which (2.11) may no longer be a consistent estimator of $\boldsymbol{R}_x$ [77, 183]. For details on array processing under uncertainty in noise statistics the reader is referred to [77, 183] and references therein.

2.2 Ideal array models and real-world arrays

Array processing models and methods require the array steering vector of the employed sensor array. This includes knowing the gain function and phase centers of the array elements. In order to simplify the signal processing algorithms, and make the problem more tractable, the array elements are typically assumed to be electrically small compared to the wavelength. Moreover, they are assumed to be free of interactions from the other array elements as well as from the mounting platform. Such ideal assumptions lead to array steering vector models with simple gain functions and element phase centers that correspond to their actual physical locations.

For example, the so-called EM vector-sensor captures the entire six components[1] of the propagating EM wavefield at a single location in space by employing electric dipoles and loop antennas [62, 83, 90, 104, 105]. It is typically assumed that the elements composing such an EM vector-sensor

[1] These are the three components of the Electric-field along the x-, y-, and z-axis, and similarly for the Magnetic-field; see Fig. 2.1 for details. Note that far-field conditions are assumed valid.

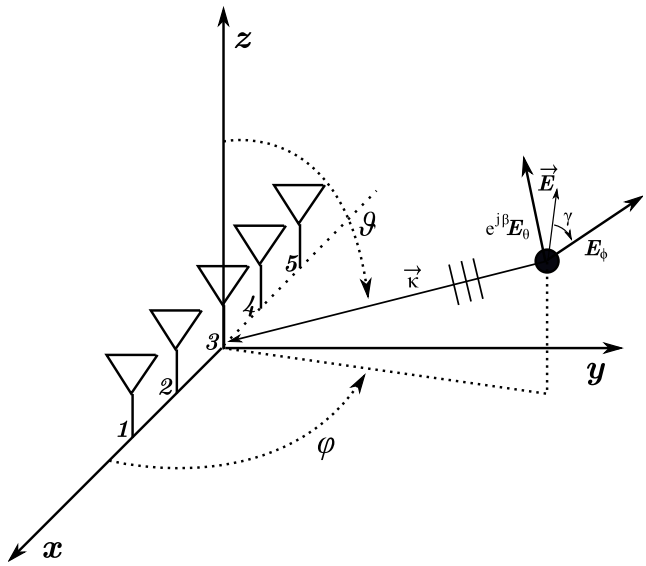

Figure 2.2. Example of an ideal uniform linear array.

share the same phase center, which is at their common physical location, and that their gain functions, denoted as $\boldsymbol{g}_\theta(\vartheta,\varphi), \boldsymbol{g}_\phi(\vartheta,\varphi) \in \mathbb{R}^{6\times 1}$, are given by [90]:

$$\boldsymbol{g}_\theta(\vartheta,\varphi) = \Big[\cos(\vartheta)\cos(\varphi),\ \cos(\vartheta)\sin(\varphi),\ -\sin(\vartheta),\ -\sin(\varphi),\ \cos(\varphi),\ 0\Big]^T \tag{2.12a}$$

$$\boldsymbol{g}_\phi(\vartheta,\varphi) = \Big[-\sin(\varphi),\ \cos(\varphi),\ 0,\ -\cos(\vartheta)\cos(\varphi),\ -\cos(\vartheta)\sin(\varphi),\ \sin(\vartheta)\Big]^T. \tag{2.12b}$$

Under the assumption that the elements of an EM vector-sensor are independently located in free-space, so that elements' interactions are negligible, the steering vectors of an N-element EM vector-sensor array are given by:

$$\boldsymbol{a}_\theta(\vartheta,\varphi) = \Big[\mathrm{e}^{\mathrm{j}\boldsymbol{k}^T\boldsymbol{r}_1},\ \ldots,\ \mathrm{e}^{\mathrm{j}\boldsymbol{k}^T\boldsymbol{r}_N}\Big]^T \otimes \boldsymbol{g}_\theta(\vartheta,\varphi) \tag{2.13a}$$

$$\boldsymbol{a}_\phi(\vartheta,\varphi) = \Big[\mathrm{e}^{\mathrm{j}\boldsymbol{k}^T\boldsymbol{r}_1},\ \ldots,\ \mathrm{e}^{\mathrm{j}\boldsymbol{k}^T\boldsymbol{r}_N}\Big]^T \otimes \boldsymbol{g}_\phi(\vartheta,\varphi), \tag{2.13b}$$

where $\boldsymbol{r}_n \in \mathbb{R}^{3\times 1}$ denotes the location of the nth EM vector-sensor with respect to the assumed coordinate system, in the 3-d Euclidean space. Typically, it is further assumed that the EM sensors are arranged in a regular geometry such as a line, circle, sphere, or a rectangle, in addition to a uniform spacing among them [83, 91]. These arrays are known as uniform linear, circular, spherical, or rectangular arrays, respectively. A uniform linear array (ULA) is illustrated in Fig. 2.2.

However, most sensor arrays built in practice are not well described by the models in eqs. (2.12) and (2.13) [55, 85]. For example, due to mutual coupling, the elements composing a real-world EM vector-sensor may not share the same phase-center. Furthermore, the phase-center of an EM sensor typically varies with the polarization of the received EM wavefield, and may not correspond to the physical location of the array elements. Further complications arise when reflections from the array mounting platform are taken into account. Figure 2.3 illustrates the phase centers of a real-world uniform linear array.

In practical array processing applications, where DoA estimation or spatial filtering is the goal, employing ideal array models that do not take into account the various impairments discussed above typically leads to a performance degradation [163]. In fact, the limiting factor in the performance of high-resolution and optimal array processing algorithms is known to be the accuracy of the employed array model rather than measurement noise [66, 85, 153, 154, 163, 166]. The tightness of related theoretical performance bounds is also limited by the accuracy of the employed array model, except in the low SNR region where performance bounds such as the CRB may not be tight. Misspecified sensor array models may also lead to a severe performance degradation of beamforming techniques, such as steering energy towards unwanted directions, cancellation of the SOI as well as amplification of interfering sources [46].

Deriving the array manifold of real-world arrays is extremely challenging since it requires a mathematical model in a closed-form describing all array nonidealities such as mounting platform reflections, mutual coupling, cross-polarization effects as well as individual beampatterns. Hence, practitioners typically acquire the array response of real-world arrays either from numerical EM simulation software, which is typically available at the array's design phase, or from array calibration measurements taken in controlled environments. EM simulation software do not take into account manufacturing errors and may not capture all of the EM interactions occurring on a real-world array. Conversely, array calibration measurements may describe the actual response of real-world arrays but are subject to measurement noise. Note that both numerical EM simulation software and array calibration measurements do not provide the array manifold in a closed-form but only complex-valued numerical data describing the array response. From a signal processing perspective it is convenient to have the array manifold in a closed-form since it facilitates

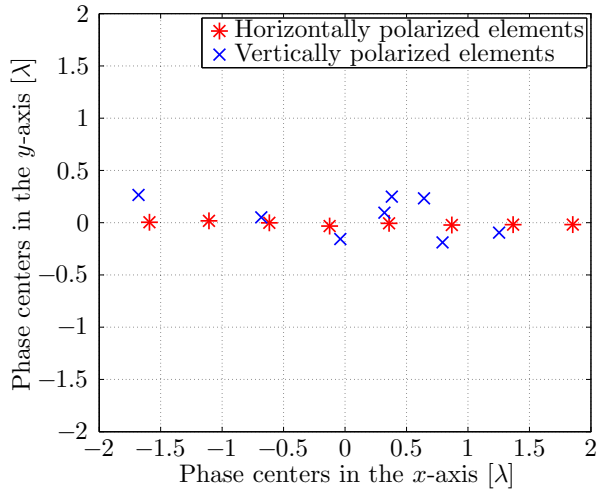

(a) Phase centers for an horizontally polarized Electric-field.

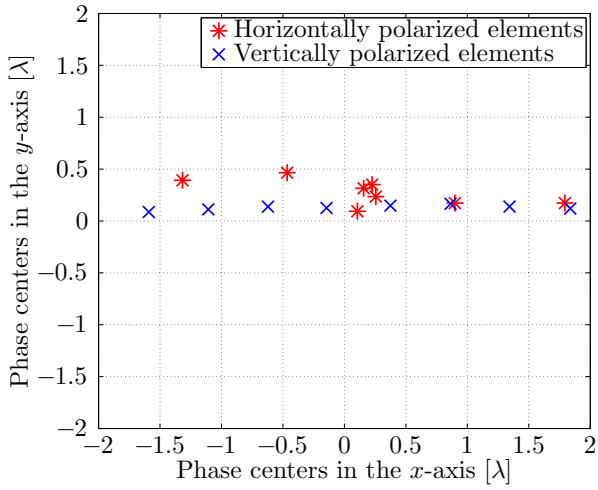

(b) Phase centers for a vertically polarized Electric-field.

Figure 2.3. Phase centers of the real-world polarimetric uniform linear patch array (PULPA) shown in Fig. 2.4-6. The PULPA is composed of eight dual-polarized elements and the physical inter-element spacing is 0.4943λ. Phase centers of real-world arrays may not match with the physical location of the elements and vary significantly with polarization of the received wavefield.

finding performance bounds such as the CRB, and optimizing multidimensional array processing methods by gradient-based techniques.

Figure 2.4 illustrates the real-world antenna arrays employed in this research work. In particular, Fig. 2.4-1 depicts a polarimetric semi-spherical patch array (PSSPA) composed of 21 elements while Fig. 2.4-2 shows a 5-element inverted-F antenna array (IFA). Figures 2.4-3 and

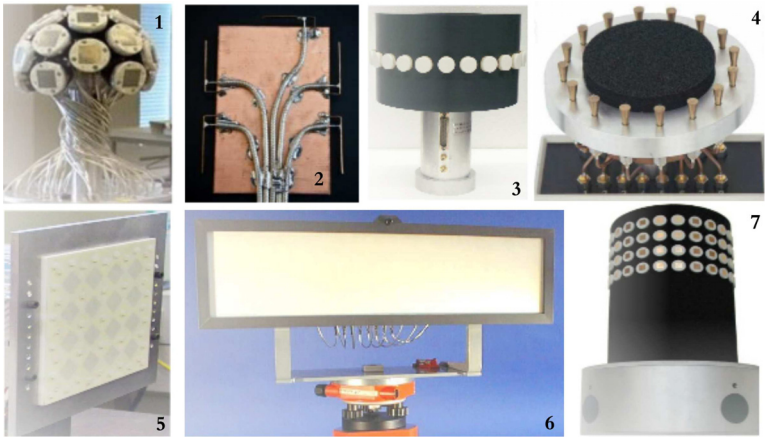

Figure 2.4. Real-world antenna arrays employed in this research work. Courtesy of the Electronic Measurement Research Laboratory, Ilmenau University of Technology, Germany and Department of Radio Science and Engineering, Aalto University, Finland.

2.4-4 illustrate a polarimetric uniform circular patch array (PUCPA) of 24 elements and a real-world uniform circular array (UCA) composed of 16 conical elements, respectively. Note that dual-polarized elements are also known as polarimetric. In Figs. 2.4-5 and 2.4-6, a polarimetric uniform rectangular patch array (PURPA) with 16 elements and a polarimetric uniform linear patch array (PULPA) composed of 8 polarimetric elements are shown. Finally, Fig. 2.4-7 illustrates a stacked polarimetric uniform circular patch array (SPUCPA) comprised of four rings of 24 polarimetric elements. The center frequency and bandwidth of the 5-element IFA is approximately 3.5 GHz and 120 MHz, respectively [5]. The remaining antenna arrays have been designed for a center frequency of 5.3 GHz and a bandwidth of 120 MHz [87]. The PUCPA, UCA, PULPA, and SPUCPA are courtesy of the Electronic Measurement Research Laboratory, Ilmenau University of Technology, Germany. The PSSPA, IFA, and PURPA are courtesy of the Department of Radio Science and Engineering, Aalto University, Finland.

Signal processing methods for real-world arrays thus require a preprocessing stage that is able to deal with aforementioned nonidealities. Such techniques are briefly described in the next chapter.

3. Array processing in the face of nonidealities

The limiting factor in the performance of high-resolution and optimal array processing methods as well as in the tightness of related theoretical performance bounds is known to be the accuracy of the employed array steering vector model [46, 77, 163]. This chapter provides a review of the most relevant techniques for dealing with array nonidealities. In particular, auto-calibration techniques and robust methods based on uncertainty sets are briefly described. Emphasis is given to array calibration measurements and array mapping techniques, including array interpolation and beamspace transform. Wavefield modeling and manifold separation are also briefly considered in this chapter. Chapter 4 provides a more detailed analysis of this last approach. This chapter concludes with a qualitative comparison of the aforementioned techniques.

3.1 Auto-calibration techniques

Auto-calibration techniques, also known as self-calibration, amount to estimate wavefield and array parameters simultaneously from a collection of array snapshots. Array parameters, denoted by $\boldsymbol{\rho}$, may represent unknown array elements' positions, mutual coupling, as well as other array nonidealities. For example, array elements' misplacements in the xy-plane are described by a real-valued vector $\boldsymbol{\rho}$ of dimension $2N$. Assume that the array response can be described in a closed-form by both wavefield $\boldsymbol{\xi}$ and array parameters $\boldsymbol{\rho}$, and denote the corresponding array steering matrix by $\boldsymbol{A}(\boldsymbol{\xi}, \boldsymbol{\rho})$. The parameter vector $\boldsymbol{\xi}$ may denote the DoAs of the sources, for example. Simultaneous estimation of wavefield and array parameters may be accomplished by the following nonlinear least-squares (NNLS) estimator [163, 172]:

$$\left(\hat{\boldsymbol{\xi}}, \hat{\boldsymbol{\rho}}\right) = \arg\min_{\boldsymbol{\xi},\boldsymbol{\rho}} \operatorname{tr}\left\{\boldsymbol{P}_{\boldsymbol{A}}^{\perp}(\boldsymbol{\xi}, \boldsymbol{\rho})\hat{\boldsymbol{R}}_x\right\}, \tag{3.1}$$

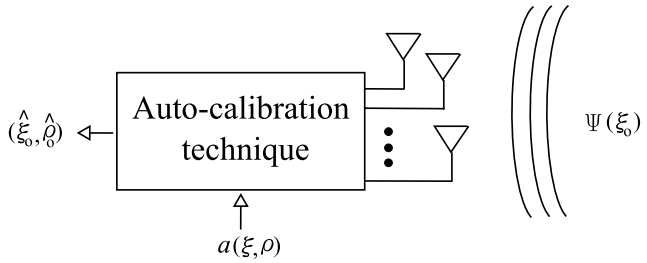

Figure 3.1. Illustration of a typical auto-calibration technique. A closed-form expression of the array steering vector in terms of wavefield parameters and nonidealities is required.

where $\boldsymbol{P}_{\boldsymbol{A}}^{\perp}(\boldsymbol{\xi},\boldsymbol{\rho}) = \boldsymbol{I}_N - \boldsymbol{P}_{\boldsymbol{A}}(\boldsymbol{\xi},\boldsymbol{\rho})$ denotes an orthogonal projection matrix onto the nullspace of $\boldsymbol{A}^H(\boldsymbol{\xi},\boldsymbol{\rho})$. Note that $\boldsymbol{P}_{\boldsymbol{A}}(\boldsymbol{\xi},\boldsymbol{\rho}) \in \mathbb{C}^{N\times N}$ denotes a projection matrix onto the column-space of $\boldsymbol{A}(\boldsymbol{\xi},\boldsymbol{\rho})$, and it is given by $\boldsymbol{P}_{\boldsymbol{A}}(\boldsymbol{\xi},\boldsymbol{\rho}) = \boldsymbol{A}^{\dagger}(\boldsymbol{\xi},\boldsymbol{\rho})\boldsymbol{A}(\boldsymbol{\xi},\boldsymbol{\rho})$. When measurement noise in (2.2) is zero-mean complex-circular Gaussian distributed, and the unknown parameters are deterministic, (3.1) is known as deterministic, or conditional, maximum likelihood estimator (MLE) [109,144,146,164]. Typically, criterion (3.1) is minimized in an alternating manner between the wavefield $\boldsymbol{\xi}$ and array parameters $\boldsymbol{\rho}$ [39,182]. Since the cost function in (3.1) is highly nonlinear, and may have multiple local minima, the minimization should be initialized with "good enough" (and possibly multiple) initial values so that the global minimum can be found.

In general, both wavefield and array parameters are not simultaneously identifiable from a collection of array snapshots, unless additional assumptions regarding the array sensors' locations, and the number of sources generating the wavefield are made [4,127]. For example, the DoAs and the array elements positions are not simultaneously identifiable since the DoA is defined by the relative phases among array elements, which in turn depend on the array sensors' locations. In case the DoAs and array configuration can be determined up to a rotational ambiguity, the spatial signature of the sources may be determined uniquely, which can be used to estimate the transmitted signals [4].

Another approach to consider the identifiability issue in auto-calibration is based on the assumption that the array parameters $\boldsymbol{\rho}$ are random quantities with a known prior distribution, and proceed with Bayesian-type of estimators [167]. In fact, the resulting maximum *a posteriori* estimator may be seen as a regularization to the ML criterion, such that of (3.1), where the regularization parameter is obtained from the prior distribu-

tion [163]. The Bayesian approach combines prior information and observed data in an optimal manner. The effect of the prior distribution diminishes as the number of observations grow. In principle, the Bayesian framework also allows one to "integrate out" the unknown array parameters ρ, and obtain an estimator that is a function of the wavefield parameters ξ, only [69]. Typically, in array processing applications one is mainly interested in the wavefield parameters, and ρ are commonly regarded as nuisance parameters. However, such a task of "integrating out" the array nonidealities is typically extremely challenging due to the non-trivial parameterization of ρ in the array response. For example, in case the parameter vector ρ denotes array elements' misplacements, which are assumed to obey a truncated Gaussian distribution, the pdf of the multivariate observations after marginalizing ρ may not be found in a closed-form.

An alternative approach consists in employing subspace-based estimators for the wavefield parameters ξ that take into account the second-order statistics of the array parameters by properly weighting the signal or noise subspaces of the sample covariance matrix [153, 154, 166, 167]. Bayesian-type of estimators are sometimes regarded as being robust to uncertainties in the array response [66, 154, 167]. In particular, the variation of the array response is taken into account in terms of a known prior distribution for the array nonidealities. However, obtaining a prior distribution describing accurately the array nonidealities may be extremely challenging in practice, and Bayesian-type of estimators may be sensitive to misspecifications of the employed distribution. Figure 3.1 illustrates a typical auto-calibration technique.

3.2 Uncertainty sets on the array steering vector

Robust array processing methods acknowledge that the underlying assumptions regarding the propagating wavefield, sensor array response, and noise statistics may not hold. They trade-off optimality for reliable performance under such circumstances [46, 48, 77, 92, 168, 183]. One such an approach amounts at optimizing certain performance criteria under the assumption that the uncertainty about the real-world array steering vector can be bounded. Geometrically, this may be understood as having an ellipsoid enclosing the maximum uncertainty regarding the real-world array steering vector. The use of uncertainty sets may also be understood as a minimax approach where the goal is to optimize a given performance

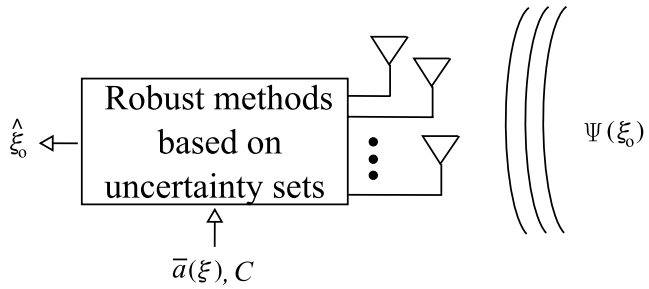

Figure 3.2. Illustration of a typical robust technique based on uncertainty sets such as the robust Capon method. A presumed array steering vector and corresponding uncertainty, described by matrix $\boldsymbol{C}$, is typically needed.

criterion under a worst-case scenario.

Let $\boldsymbol{a}(\boldsymbol{\xi}) \in \mathbb{C}^{N\times 1}$ denote the steering vector of the real-world sensor array and $\bar{\boldsymbol{a}}(\boldsymbol{\xi}) \in \mathbb{C}^{N\times 1}$ the steering vector of the presumed sensor array. The uncertainty ellipsoid may be written as [93, 98]:

$$(\boldsymbol{a}(\boldsymbol{\xi}) - \bar{\boldsymbol{a}}(\boldsymbol{\xi}))^H \boldsymbol{C}^{-1} (\boldsymbol{a}(\boldsymbol{\xi}) - \bar{\boldsymbol{a}}(\boldsymbol{\xi})) \leq 1, \tag{3.2}$$

where $\boldsymbol{C} \in \mathbb{C}^{N\times N}$ denotes a known *positive-definite* matrix that characterizes the shape and volume of the ellipsoid centered at $\bar{\boldsymbol{a}}(\boldsymbol{\xi})$. Ellipsoids of the form of (3.2) are called nondegenerate ellipsoids. If the uncertainty ellipsoids fall into a lower-dimensional space they are called flat (or degenerate) ellipsoids, and a representation different from that in (3.2) should be used [93, 98]. Flat ellipsoids are employed to make the uncertainty set as tight as possible but require more prior information about the maximum uncertainty than that of the nondegenerate ellipsoids. Typically, $\bar{\boldsymbol{a}}(\boldsymbol{\xi})$ and $\boldsymbol{C}$ in (3.2) are assumed known but such quantities may also be estimated from array calibration measurements [98]. For example, in case the uncertainty is identical for all of the array elements, $\boldsymbol{C}$ is a scaled identity matrix. Other examples include the case when different array elements have varying degrees of uncertainties as well as when the elements' uncertainties are correlated. In the former case matrix $\boldsymbol{C}$ is diagonal with nonidentical entries while in the latter case $\boldsymbol{C}$ has nonzero off-diagonal elements.

Uncertainty sets on the array steering vector have been mainly employed in the context of minimum variance adaptive beamforming [93, 98, 168]. In particular, they employ the following robust estimate of the real-world array steering vector [93]:

$$\hat{\boldsymbol{a}}(\boldsymbol{\xi}) = \bar{\boldsymbol{a}}(\boldsymbol{\xi}) - \hat{\boldsymbol{U}}(\boldsymbol{I} + \lambda(\boldsymbol{\xi})\hat{\boldsymbol{\Lambda}})^{-1}\hat{\boldsymbol{U}}^H \bar{\boldsymbol{a}}(\boldsymbol{\xi}), \tag{3.3}$$

where $\hat{\boldsymbol{U}} \in \mathbb{C}^{N \times N}$ and $\hat{\boldsymbol{\Lambda}} \in \mathbb{R}^{N \times N}$ denote the eigenvectors of the sample covariance matrix $\hat{\boldsymbol{R}}_x$ and corresponding eigenvalues, respectively. In (3.3), $\lambda(\boldsymbol{\xi}) \in \mathbb{R}$ is found numerically for a given uncertainty ellipsoid $\boldsymbol{C}$ centered at $\bar{\boldsymbol{a}}(\boldsymbol{\xi})$; see [93] for details. Note that $\lambda(\boldsymbol{\xi})$ may be understood as a regularization of the array sample covariance matrix $\hat{\boldsymbol{R}}_x$ in terms of *diagonal loading*. Such type of regularization has the effect of widening the main beam of the Capon beamformer [18]. Chapter 5 includes a more detailed discussion on diagonal loading.

Writing (3.3) as $\hat{\boldsymbol{a}}(\boldsymbol{\xi}) = \boldsymbol{W}\bar{\boldsymbol{a}}(\boldsymbol{\xi})$, where $\boldsymbol{W} = \hat{\boldsymbol{U}}(\boldsymbol{I} - (\boldsymbol{I} + \lambda(\boldsymbol{\xi})\hat{\boldsymbol{\Lambda}})^{-1})\hat{\boldsymbol{U}}^H$ shows that the robust estimate in (3.3) is obtained by properly weighting the presumed array steering vector $\bar{\boldsymbol{a}}(\boldsymbol{\xi})$. A similar expression is obtained in the robustified MUSIC method based on uncertainty sets [150]. Figure 3.2 illustrates a typical robust technique based on uncertainty sets such as the robust Capon method.

3.3 Array calibration measurements

Array calibration aims at acquiring the array response of real-world arrays through measurements from a number of different locations of angles. They capture the combined effects due to mutual coupling, cross-polarization effects, and mounting platform reflections, in addition to array elements' misplacements and individual beampatterns. Typically, array calibration measurements are acquired in controlled environments such as anechoic chambers, and allow for obtaining an accurate and complete description of the radiating characteristics of real-world arrays. High-resolution radar, satellite, and communication systems often require such accurate antenna array responses that are typically obtained from array calibration measurements [45].

The most commonly used approach for array calibration measurements acquires the array response to a known active source, called probe, at different angles and polarizations. The antenna array is typically mounted on a mechanical platform, known as positioner, that rotates the sensor array in azimuth φ and co-elevation ϑ angles while the probe is held fixed. Dual-polarized probes are typically employed since one may acquire the array response to horizontal and vertical polarizations without the requirement of rotating the probe as well. Figure 3.3 illustrates a typical array calibration measurement setup. Note that the coordinate system employed in array processing methods is defined by the relative position

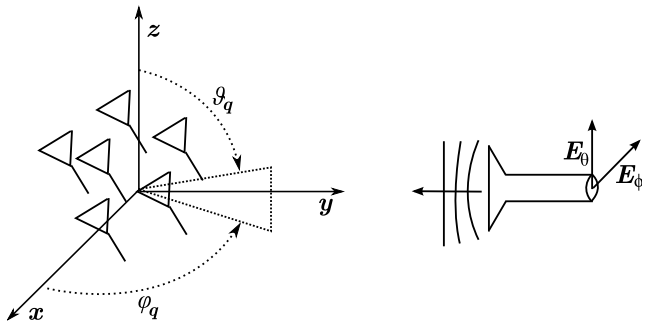

Figure 3.3. Illustration of the standard array calibration measurement setup.

between the positioner and probe.

Assume that the probe is a point-source, such as an Hertzian dipole, located in the far-field region of the antenna array. The array output obtained in array calibration measurements may be described by the following expressions:

$$\boldsymbol{x}_\theta(k,\vartheta_q,\varphi_q) = \boldsymbol{a}_\theta(\vartheta_q,\varphi_q)s(k) + \boldsymbol{\varepsilon}_\theta(k) \tag{3.4a}$$

$$\boldsymbol{x}_\phi(k,\vartheta_q,\varphi_q) = \boldsymbol{a}_\phi(\vartheta_q,\varphi_q)s(k) + \boldsymbol{\varepsilon}_\phi(k), \tag{3.4b}$$

where $\boldsymbol{x}_\theta(k,\vartheta_q,\varphi_q), \boldsymbol{x}_\phi(k,\vartheta_q,\varphi_q) \in \mathbb{C}^{N\times 1}$ denote the array output at the kth snapshot for a vertically and horizontally polarized probe located at angles (ϑ_q,φ_q), respectively. In practice, the array output is acquired by measuring the induced voltage at each antenna, followed by down-conversion, demodulation, and analog-to-digital conversion. In (3.4), $s(k) \in \mathbb{C}$ denotes a *known* transmitted signal with power σ_s^2, and $\boldsymbol{\varepsilon}_\theta(k) \in \mathbb{C}^{N\times 1}$ as well as $\boldsymbol{\varepsilon}_\phi(k) \in \mathbb{C}^{N\times 1}$ denote calibration measurement noise. In this research work, calibration measurement noise are assumed to be spatially and temporally uncorrelated zero-mean complex-circular Gaussian distributed i.e., $\boldsymbol{\varepsilon}_\theta(k) \sim \mathcal{N}_c(\boldsymbol{0}, \sigma_{\text{cal}}^2\boldsymbol{I}_N)$ and $\boldsymbol{\varepsilon}_\theta^H(k)\boldsymbol{\varepsilon}_\phi(k) = 0$, and similarly for $\boldsymbol{\varepsilon}_\phi(k)$. The least-squares estimator (LSE) of the array response at angles (ϑ_q,φ_q) is [163]:

$$\hat{\boldsymbol{a}}_\theta(\vartheta_q,\varphi_q) = \sum_{k=1}^{K} \boldsymbol{x}_\theta(k,\vartheta_q,\varphi_q)s^*(k) / \sum_{k=1}^{K} |s(k)|^2 \tag{3.5a}$$

$$\hat{\boldsymbol{a}}_\phi(\vartheta_q,\varphi_q) = \sum_{k=1}^{K} \boldsymbol{x}_\phi(k,\vartheta_q,\varphi_q)s^*(k) / \sum_{k=1}^{K} |s(k)|^2. \tag{3.5b}$$

Since the array responses at angles (ϑ_q,φ_q) may also be seen as unknown channel coefficients, under zero-mean complex-circular Gaussian noise assumption, the maximum-likelihood estimator (MLE) of $\boldsymbol{a}_\phi(\vartheta_q,\varphi_q)$ and $\boldsymbol{a}_\theta(\vartheta_q,\varphi_q)$ are also given by (3.5) [3, 69].

Collecting $\hat{\boldsymbol{a}}_\phi(\vartheta_q,\varphi_q), \hat{\boldsymbol{a}}_\theta(\vartheta_q,\varphi_q)$ for $Q_a \in \mathbb{N}$ points in azimuth and $Q_e \in \mathbb{N}$ points in co-elevation yields the *array calibration matrix*, denoted by $\boldsymbol{B} = [\boldsymbol{B}_\theta,\ \boldsymbol{B}_\phi] \in \mathbb{C}^{N\times 2Q}$, where $Q = Q_aQ_e$ denotes the total number of calibration points and $\boldsymbol{B}_\theta, \boldsymbol{B}_\phi \in \mathbb{C}^{N\times Q}$ are respectively given by[1]:

$$\boldsymbol{B}_\theta = \left[\hat{\boldsymbol{a}}_\theta(\vartheta_1,\varphi_1),\ldots,\hat{\boldsymbol{a}}_\theta(\vartheta_1,\varphi_{Q_a}),\hat{\boldsymbol{a}}_\theta(\vartheta_2,\varphi_1),\ldots,\hat{\boldsymbol{a}}_\theta(\vartheta_{Q_e},\varphi_{Q_a})\right] \tag{3.6a}$$

$$\boldsymbol{B}_\phi = \left[\hat{\boldsymbol{a}}_\phi(\vartheta_1,\varphi_1),\ldots,\hat{\boldsymbol{a}}_\phi(\vartheta_1,\varphi_{Q_a}),\hat{\boldsymbol{a}}_\phi(\vartheta_2,\varphi_1),\ldots,\hat{\boldsymbol{a}}_\phi(\vartheta_{Q_e},\varphi_{Q_a})\right]. \tag{3.6b}$$

In general, a complete characterization of real-world arrays requires that the array calibration matrix is composed of array responses spanning the whole angular region, i.e. $\vartheta_q \in [0,\pi], \varphi_q \in [0,2\pi)$. The array response is said to be acquired in the 2-sphere[2] ($\mathcal{S}^2$). However, it may be sufficient to collect the array responses over an angular sector only, say $\mathcal{C} \subset \mathcal{S}^2$, if the sensor array is to be deployed on an environment where the sources are known *a priori* to be confined to such a sector $\mathcal{C}$ [163]. Similarly, considering angular sectors may be the only feasible option of calibrating a sensor array due to physical limitations of the mounting platform. The impact of incomplete array calibration measurements on high-resolution array processing algorithms is considered in [85]. Details on the sampling grid used in (3.6) are given in Chapter 4. It is also shown in Chapter 4 that employing wavefield modeling and manifold separation typically leads to an improvement of the MSE achieved by the array calibration matrix.

Typically, the array gain $\|\boldsymbol{a}(\vartheta,\varphi,\gamma,\beta)\|^2$ of real-world arrays is a function of the angle (ϑ,φ) and polarization (γ,β). This may be due to the array elements' directivity and polarization sensitivity. Hence, it is convenient to define the following *average* array gain:

$$\frac{1}{4\pi}\int_{\mathcal{S}^2} \boldsymbol{a}_\theta^H(\vartheta,\varphi)\boldsymbol{a}_\theta(\vartheta,\varphi) + \boldsymbol{a}_\phi^H(\vartheta,\varphi)\boldsymbol{a}_\phi(\vartheta,\varphi)\,d\Omega = N, \tag{3.7}$$

where $d\Omega = \sin(\vartheta)\,d\vartheta d\varphi$. The normalization defined in (3.7) is employed throughout this work and useful in describing the SNR gain obtained by using multi-antenna systems.

In addition to calibration measurement noise, array calibration measurements may be subject to other sources of errors. These include re-

[1]The use of a rectangular grid is *not* a restriction but simply a notational convenience. Chapter 4 considers the case where one may acquire a single observation at the poles, and not Q_a samples.

[2]A 2-sphere is a surface (or 2-D manifold) in a 3-D Euclidean space where its points satisfy $(x-x_0)^2+(y-y_0)^2+(z-z_0)^2 = r^2$, for a given center (x_0,y_0,z_0) and radius r. A 2-sphere refers to the usual sphere. A 1-sphere is a 1-D manifold and it refers to the usual circle.

flections from the anechoic chamber, imperfections of the employed positioner, attenuations and phase-drifts due to cabling, small distance between the antenna array and probe (i.e., source not in far-field), and effects of the probe (e.g., not a point-source). These errors are not considered in this research work, and the interested reader is referred to [45, 55, 85, 159] and references therein. However, it is important to mention that a widely used technique in array calibration measurements called spherical near-field antenna measurements [55] has strong connections with wavefield modeling [28–30], [VI] and manifold separation [9], [IV, V, VII]. This is further discussed in Chapter 4.

3.4 Local interpolation of the array calibration matrix

The array calibration matrix $\boldsymbol{B}$ in (3.6) may be seen as the result of a discretization operation on the array manifold $\mathcal{A}$ in (2.4) under additive white Gaussian noise (AWGN). An approximation of the array manifold may thus be obtained by interpolating $\boldsymbol{B}$. However, interpolation may overfit the data and describe measurement noise rather than the array manifold. Alternatively, one may employ the principle of Parsimony in a model fitting approach in order to minimize the contribution of calibration measurement noise [111, 147]. Such an approach is further discussed in Chapter 4 in the context of wavefield modeling and manifold separation.

Let $\boldsymbol{\alpha}_n(\vartheta, \varphi)$ denote a vector composed of local basis functions such as wavelets, splines or polynomials. Also, let $\hat{\boldsymbol{C}}_n$ denote a coefficient matrix obtained by interpolating the array calibration matrix $\boldsymbol{B}$ over an angular sector $\mathcal{C}_n$ using $\boldsymbol{\alpha}_n(\vartheta, \varphi)$. $\mathcal{C}_n$ may correspond to two or more columns of $\boldsymbol{B}$. Using local basis as the interpolating functions leads to the following *piece-wise* estimate of the real-world array steering vector:

$$\hat{\boldsymbol{a}}_\theta(\vartheta, \varphi) = \begin{cases} \hat{\boldsymbol{C}}_1 \boldsymbol{\alpha}_1(\vartheta, \varphi), & (\vartheta, \varphi) \in \mathcal{C}_1 \\ \hat{\boldsymbol{C}}_2 \boldsymbol{\alpha}_2(\vartheta, \varphi), & (\vartheta, \varphi) \in \mathcal{C}_2 \\ \quad \vdots & \\ \hat{\boldsymbol{C}}_n \boldsymbol{\alpha}_n(\vartheta, \varphi), & (\vartheta, \varphi) \in \mathcal{C}_n, \end{cases} \tag{3.8}$$

and similarly for $\hat{\boldsymbol{a}}_\phi(\vartheta, \varphi)$.

Local interpolation of the array calibration matrix requires the practitioner to choose the local basis functions and their degree, with particular continuity and differentiability properties, as well as the size of each angular sector. Thus, local interpolation may not be convenient in array pro-

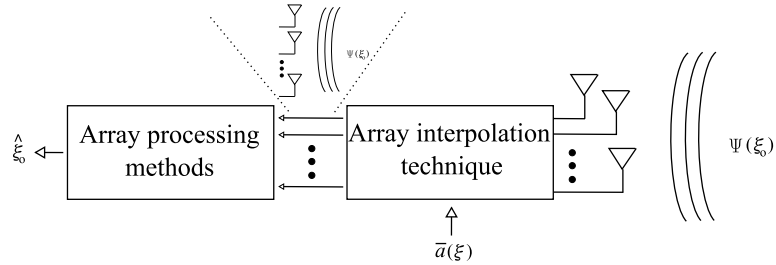

Figure 3.4. Illustration of a typical array interpolation technique. A virtual array is needed along with a specification of the array elements, geometry, and size of each angular sector.

cessing when the sources may span the whole visible region. In Chapter 4 and Section 4.1, wavefield modeling and manifold separation are shown to alleviate many of these difficulties.

3.5 Array mapping techniques

3.5.1 Array interpolation based on virtual arrays

Array interpolation techniques aim at replacing the real-world array response in the acquired array snapshots by the response of an ideal sensor array, known as *virtual array* [15, 40, 47, 63, 64]. Typically, this is accomplished by linearly transforming the array output data in a manner that the transformed data approximates those acquired by employing a virtual array. Computationally efficient array processing methods developed for ideal ULAs and URAs, such as root-MUSIC, ESPRIT, and spatial smoothing, may be employed with real-world sensor arrays and nonidealities by exploiting the transformed data as well as the structure of the virtual array [14, 41, 128, 139, 174]. The configuration of the virtual array as well as the number of elements and orientation are user-parameters that need to be specified by the practitioner. The aperture of the virtual array is commonly designed to be enclosed by the real-world array [28, 40].

Let us assume single (e.g., vertically) polarized wavefields propagating in the xy-plane, and denote the corresponding steering vector of the virtual array by $\bar{\boldsymbol{a}}(\varphi) \in \mathbb{C}^{\bar{N}\times 1}$. The virtual array is composed of $\bar{N} \in \mathbb{N}(\bar{N} \leq N)$ virtual elements. Also, let $\bar{\boldsymbol{B}} = [\bar{\boldsymbol{a}}(\varphi_1), \ldots, \bar{\boldsymbol{a}}(\varphi_{Qa})] \in \mathbb{C}^{\bar{N}\times Q_a}$ denote a collection of virtual array steering vectors. In its simplest form, the transformation matrix $\hat{\boldsymbol{T}} \in \mathbb{C}^{\bar{N}\times N}$ employed by array interpolation techniques

is the solution to the following quadratic-error criterion [40]:

$$\hat{\boldsymbol{T}}_{\mathrm{ls}} = \arg\min_{\boldsymbol{T}} \|\boldsymbol{T}\boldsymbol{B} - \bar{\boldsymbol{B}}\|_F^2, \tag{3.9}$$

where $\boldsymbol{B} \in \mathbb{C}^{N \times Qa}$ denotes the calibration matrix of the real-world array. The solution to (3.9) is well-known to be $\hat{\boldsymbol{T}}_{\mathrm{ls}} = \bar{\boldsymbol{B}}\boldsymbol{B}^{\dagger}$. Given a collection of snapshots $\boldsymbol{X} = [\boldsymbol{x}(1), \ldots, \boldsymbol{x}(K)]$, the output of the virtual array and corresponding sample covariance matrix are found, respectively, as $\boldsymbol{Y} = \hat{\boldsymbol{T}}_{\mathrm{ls}}\boldsymbol{X}$ and $\hat{\boldsymbol{R}}_y = \hat{\boldsymbol{T}}_{\mathrm{ls}}\hat{\boldsymbol{R}}_x\hat{\boldsymbol{T}}_{\mathrm{ls}}^H$, where $\hat{\boldsymbol{R}}_x$ is given in (2.9). Array processing methods that exploit the structure of the virtual array may be applied to $\boldsymbol{Y}$ and $\hat{\boldsymbol{R}}_y$. Note that the virtual array should be designed so that $\hat{\boldsymbol{R}}_y$ is full-rank. In case the condition $\bar{N} \leq N$ does not lead to a full-rank virtual sample covariance matrix the virtual array should be re-designed [40]. Also, it is desirable to design the virtual array so that the transformation matrix $\hat{\boldsymbol{T}}_{\mathrm{ls}}$ is well-conditioned [40].

Typically, the *fitting error* of the transformation matrix, obtained by using $\hat{\boldsymbol{T}}_{LS}$ in place of $\boldsymbol{T}$ in (3.9), grows with the angular sector $\mathcal{C}$ spanned by $\boldsymbol{B}$ and $\bar{\boldsymbol{B}}$ [40, 63, 64]. In general, one cannot find a perfect transformation between the virtual and the real-world array manifolds, and the resulting fitting error leads to a performance loss of array processing methods. In order to reduce fitting errors to a level where they have the same order of magnitude as the errors due to finite sample support, the angular sector $\mathcal{C}$ is kept "small enough" [40, 63]. However, when there is no prior information regarding the location of the sources, multiple angular sectors are needed to cover the entire angular domain, which leads to multiple transformation matrices (one per angular sector). Such a procedure is called *sector-by-sector processing*, and the employed transformation matrices are known to be sensitive to out-of-sector sources [63]. Robustness to out-of-sector sources may be achieved at the cost of an increase of the fitting error [114]. Figure 3.4 illustrates a typical array interpolation technique and related processing stages.

3.5.2 Phase-mode excitation and beamspace transform

Phase-mode excitation is a technique employing a *spatial* Fourier series representation in order to synthesize arbitrary excitation functions, and consequently far-field patterns, of uniform circular as well as spherical arrays [24, 25, 97, 179]. Originally developed for continuous apertures, the phase-mode excitation technique is also applicable to practical arrays that consist of a few elements. Continuous apertures may be understood

as a continuum of array elements disposed on a circular geometry, for example. In the context of array processing, the phase-mode excitation technique is known as beamspace transform [7, 100]. Both phase-mode excitation technique and beamspace transform have been widely used in array processing. They allow many of the methods originally developed for uniform linear arrays, such as polynomial rooting based DoA estimators and spatial smoothing techniques, to be applied on uniform circular as well as spherical arrays [35, 52, 100, 156, 170]. The phase-mode excitation technique is also closely related to the wavefield modeling principle and manifold separation technique. These are among the main topics of this dissertation, and are considered in detail in Chapter 4.

Consider a uniform circular array of radius R, composed of N single-polarized elements, and receiving a wavefield generated by single-polarized point-sources. Assume also wavefield propagation in the xy-plane. The phase-mode excitation technique or beamspace transform for uniform circular arrays may be written as [7, 100]:

$$\boldsymbol{F}^H \boldsymbol{a}_{\mathrm{uca}}(\varphi) \approx \sqrt{N} \boldsymbol{\mathcal{J}}(\kappa R)\, \boldsymbol{d}(\varphi), \tag{3.10}$$

where $\boldsymbol{F} \in \mathbb{C}^{N \times \mathcal{M}}$ denotes a block of an $N \times N$ unitary discrete Fourier transform (DFT) matrix. In (3.10), matrix $\boldsymbol{\mathcal{J}}(\kappa R) \in \mathbb{C}^{\mathcal{M} \times \mathcal{M}}$ and vector $\boldsymbol{d}(\varphi) \in \mathbb{C}^{\mathcal{M} \times 1}$ are respectively given by:

$$\begin{aligned} \boldsymbol{\mathcal{J}}(\kappa R) = \mathrm{diag}\{\mathrm{j}^M J_M(\kappa R), \ldots, \mathrm{j}\, J_1(\kappa R),\, J_0(\kappa R), \\ \mathrm{j}\, J_1(\kappa R), \ldots, \mathrm{j}^M J_M(\kappa R)\} \end{aligned} \tag{3.11a}$$

$$\boldsymbol{d}(\varphi) = [\mathrm{e}^{-\mathrm{j}M\varphi}, \ldots, \mathrm{e}^{-\mathrm{j}\varphi}, 1, \mathrm{e}^{\mathrm{j}\varphi}, \ldots, \mathrm{e}^{\mathrm{j}M\varphi}]^T, \tag{3.11b}$$

where $\boldsymbol{d}(\varphi)$ is comprised of spatial Fourier basis, also known as phase-modes, and $J_m(\kappa R) \in \mathbb{R}$ denotes the Bessel function of the first kind and order m [1, Ch.9]. The Vandermonde structure of vector $\boldsymbol{d}(\varphi)$ in (3.10) facilitates using techniques originally developed for uniform linear arrays on circular array geometries. A rule of thumb for determining M is $M = \lfloor \kappa R \rfloor$, where $\mathcal{M} = 2M + 1$ [25, 100]. Such a rule follows from the fact that Bessel functions decay superexponentially (i.e., faster than exponential) when the order exceeds their argument [28, 100], [1, Ch.9]. As an example, an UCA composed of N elements with an inter-element spacing of $\lambda/2$ leads to $\kappa R = N/2$.

The approximation in (3.10) is due to the aliasing introduced by employing the phase-mode excitation technique on uniform circular arrays. In fact, for a continuous circular aperture the phase-mode excitation technique is exact and expression (3.10) holds true with strict equality [24, 25,

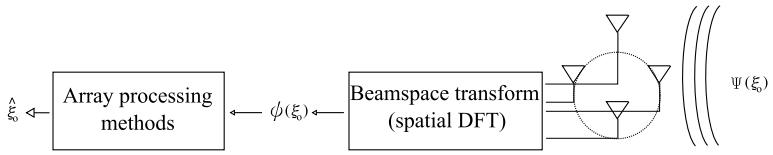

Figure 3.5. Illustration of the typical stages comprising beamspace transform based array processing methods.

97, 100]. However, when dealing with uniform circular arrays, the relationship between the number of array elements and phase-modes should satisfy $N \geq \mathcal{M}$ [100]. Such a condition makes the term $\sqrt{N}\boldsymbol{J}(\kappa R)\,\boldsymbol{d}(\varphi)$ in (3.10) larger than the term due to aliasing.

Expression (3.10) may be rewritten as follows:

$$\frac{1}{\sqrt{N}}\boldsymbol{\mathcal{J}}^{-1}(\kappa R)\boldsymbol{F}^H\boldsymbol{a}_{\mathrm{uca}}(\varphi) \approx \boldsymbol{d}(\varphi). \tag{3.12}$$

The transformation in (3.12) is known as Davis transform, and it assumes that $\{J_m(\kappa R) \neq 0\}_{m=0}^{M}$ [24, 25, 88, 170]. If $J_m(\kappa R) = 0$ for some $m \leq \lfloor \kappa R \rfloor$ the sensor array is said to operate at the resonances of the wavefield. The wavefield is thus essentially unobservable by such a sensor array, and array processing methods are not expected to provide any meaningful results [30].

Another interpretation of the phase-mode excitation technique and beamspace transform for uniform circular (or spherical) arrays is obtained by means of *wavefield decomposition* [97, 118, 156, 157, 178]. In particular, the term $\boldsymbol{J}(\kappa R)\,\boldsymbol{d}(\varphi)$ in (3.10) may be understood as the spatial Fourier coefficients of the propagating wavefield observed on a circular region of radius R. More precisely, a unit-magnitude wavefield, propagating in the xy-plane and generated by a single far-field point-source located at φ, may be decomposed at point $\boldsymbol{r}_n = [R_n,\ \varphi_n]^T$ as follows [28, 157]:

$$\Psi(\boldsymbol{r}_n) = \sum_{m=-\infty}^{+\infty} \mathrm{j}^m J_m(\kappa R_n)\,\mathrm{e}^{\mathrm{j}m(\varphi-\varphi_n)}, \tag{3.13}$$

Expression (3.13) is a spatial Fourier series of the wavefield, where the mth Fourier basis and coefficient are $\mathrm{e}^{\mathrm{j}m\varphi_n}$ and $c_m = \mathrm{j}^m J_m(\kappa R_n)\,\mathrm{e}^{\mathrm{j}m\varphi}$, respectively. The Fourier coefficients $\{c_m\}_{m=-\infty}^{+\infty}$ carry information regarding the angle of the source φ, and may be obtained by a spatial Fourier transform (at a fixed radius $R_n = R$):

$$c_m = \frac{1}{2\pi}\int_{S^1} \Psi(R,\varphi_n)\,\mathrm{e}^{\mathrm{j}m\varphi_n}\,d\varphi_n \tag{3.14a}$$

$$\approx \frac{1}{N}\sum_{n=1}^{N} \Psi(R, 2\pi n/N)\,\mathrm{e}^{\mathrm{j}m\frac{2\pi n}{N}}, \qquad \forall m. \tag{3.14b}$$

Since the nth element of a uniform circular array of radius R sample the wavefield at point $(R, 2\pi n/N)$, using $[\boldsymbol{a}_{\text{uca}}(\varphi)]_n = \Psi(R, 2\pi n/N)$ in (3.14b) yields (3.10), showing that the beamspace transform is essentially a spatial DFT of the propagating wavefield. Figure 3.5 illustrates the typical stages comprising beamspace transform based array processing methods.

Extensions of the phase-mode excitation technique, or beamspace transform, to uniform circular arrays in the presence of mutual coupling as well as other perturbations of the array manifold can be found in [51, 88, 170]. Also, extensions of the phase-mode excitation technique to spherical arrays can be found in [118, 179], forming the basis to the research topic of *spherical microphone array processing* [52, 119, 120, 122].

3.6 Wavefield modeling and manifold separation - summary

Wavefield modeling is a formalism for array processing where the array output is written as the product of a wavefield independent matrix called *array sampling matrix* and an array independent vector known as *coefficient vector* [28–30], [III, VII, VIII]. The sampling matrix depends on the employed sensor array only while the coefficient vector depends on the wavefield. Array sampling matrix and coefficient vector are independent from each other. Manifold separation stems from wavefield modeling and it is a spatial Fourier series of the array manifold and steering vector [9], [IV, V, VI].

The sampling matrix fully describes the employed sensor array, including its geometry and nonidealities, while the coefficient vector uniquely characterizes the received wavefield. Thus, the coefficient vector carries information regarding the wavefield parameters such as DoAs and polarization of the sources in a manner that is independent from the sensor array.

In particular, assuming that the employed sensor array is a linear system, in the sense of superposition principle, and continuous, the array output may be written as [28–30], [VI, VII]:

$$\boldsymbol{x}(t) = \boldsymbol{G}\,\boldsymbol{\psi}(t) + \boldsymbol{n}(t), \tag{3.15}$$

where $\boldsymbol{G} : \mathcal{H} \to \mathbb{C}^N$ and $\boldsymbol{\psi}(t) \in \mathcal{H}$ denote the array sampling matrix and coefficient vector, respectively. Moreover, vector $\boldsymbol{n}(k) \in \mathbb{C}^{N\times 1}$ denotes measurement noise which is assumed to be zero-mean complex-circular Gaussian distributed with covariance matrix given by $\boldsymbol{R}_n = \sigma^2 \boldsymbol{I}_n$. The re-

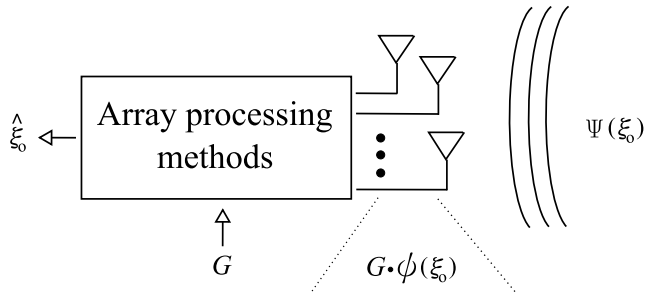

Figure 3.6. Illustration of the key concept in array processing based on wavefield modeling and manifold separation. The array output is written as the product of a wavefield independent matrix $\boldsymbol{G}$ and an array independent vector $\psi(\boldsymbol{\xi})$.

sult in (3.15) is known as *wavefield modeling*. Note that (3.15) is equally valid for sensor arrays receiving scalar-fields as well as for arrays composed of polarization sensitive antennas, observing completely polarized EM waves. Figure 3.6 illustrates the key concept in array processing based on wavefield modeling and manifold separation.

The coefficient vector $\psi(t)$ may describe the received wavefield either in a non-parametric or a parametric manner, with closed-form expressions for the DoAs and polarization of the sources. Chapter 4 includes closed-form expressions for the coefficient vector that are applicable for scalar and vector-fields. The array sampling matrix $\boldsymbol{G}$ is composed of infinitely many columns but in practice one may consider only a finite number of such columns. This follows from a key property of the array sampling matrix that is known as *superexponential decay*. Chapter 4 provides upper-bounds for the supexexponential decay of $\boldsymbol{G}$ for sensor arrays receiving scalar-fields as well as for arrays composed of polarization sensitive antennas.

Similarly to array interpolation, wavefield modeling and manifold separation may also be employed in sector-by-sector processing and in cases where the sources are known *a priori* to span an angular sector. Such an information may be incorporated into $\boldsymbol{G}$, and the resulting array sampling matrix also shares the superexponential decay property [28]. Chapter 4 provides more relationships among wavefield modeling, manifold separation, and array mapping techniques.

Wavefield modeling and manifold separation provide more insight into applications dealing with sensor arrays. For example, such a formalism is appropriate in assessing the fundamental performance limitations of real-world sensor arrays. Moreover, many of the computationally-efficient array processing methods originally developed for ULAs may be employed

Table 3.1. Qualitative comparison among array processing techniques for dealing with nonidealities.

	Techniques					
Features	US	ACM	LI	AIT	BT	WM/MS
Applicable to arbitrary array geometries	+ +	+ +	+ +	+ +	- -	+ +
Robustness to modeling errors	+ +	+	- -	- -	-	- -
Characterization of real-world array responses	- -	- -	+	-	- -	+ +
Incorporation of prior knowledge about sources' locations	+ +	+	+ +	+ +	- -	+ +
Computational complexity	- -	- -	-	+	+ +	+
Requirement for user-design parameters	-	- -	- -	- -	+ +	+ +

on sensor arrays with arbitrary geometries and nonidealities. This is addressed in Chapter 5.

3.7 Discussion

This chapter provides an overview of array processing techniques for dealing with nonidealities. Real-world sensor arrays are typically composed of elements with individual directional beampatterns. They are subject to misplacements of the array elements, mutual coupling, cross-polarization effects, and mounting platform reflections. Dealing with such nonidealities is crucial in any array processing application in order to obtain optimal results as well as avoid systematic errors and excess variance. Table 3.1 includes a qualitative comparison of the array processing techniques considered in this chapter.

Auto-calibration methods (ACM) may be useful when both wavefield parameters and array nonidealities are described in a closed-form. However, real-world directional beampatterns, cross-polarization effects, and mounting platform reflections are extremely challenging to express in a closed-form. Even if a closed-form expression for the uncalibrated steering vector is acquired, wavefield parameters and array nonidealities may not be simultaneously identifiable. Such a difficulty with parameter identifiability may be relaxed by assuming that the array nonidealities are random quantities. Typically, Bayesian-type of estimators require the second-order statistics of the array nonidealities to be fully known, which

may not be practical or realistic.

A more conservative approach to dealing with array nonidealities consists in employing uncertainty sets (US) on the array steering vector. Uncertainty sets do not require a closed-form expression for the array nonidealities and may use array calibration measurements. However, uncertainty sets trade-off optimality for robustness. Uncertainty sets may also require user-design parameters for bounding the maximal uncertainty, and the computational burden of such an approach may be prohibitive in many array processing applications.

The beamspace transform (BT) is a rather simple and convenient technique that is amenable to many computationally-efficient array processing methods. However, it requires circular or spherical arrays and its performance is typically limited by the number of array elements. Array interpolation techniques (AIT) are versatile since the practitioner has the freedom to employ most of the computationally-efficient array processing methods originally developed for ULAs on arrays with arbitrary geometries. However, in cases where the practitioner does not have prior knowledge regarding the location of the sources the performance of array interpolation techniques may be rather poor and the corresponding computational burden may be significant.

Wavefield modeling (WM) and manifold separation (MS) may be seen as an alternative approach of describing the array output. The ability to separate the array parameters, including the array nonidealities, from the wavefield parameters is convenient in many array processing methods. Moreover, the linear relationship describing the array output in terms of sampling matrix and coefficient vector makes wavefield modeling and manifold separation a very attractive technique in signal processing. More details regarding the advantages and limitations of wavefield modeling and manifold separation are provided in the next chapter.

4. Wavefield modeling and manifold separation

This chapter describes the theoretical and practical aspects of wavefield modeling and manifold separation. The simpler case of scalar-fields such as acoustic pressure is briefly considered. Emphasis is given to vector-fields such as completely polarized EM waves that may propagate in the 3-D Euclidean space [III, VII, VIII]. The estimation of the array sampling matrix from calibration measurements is also considered [V]. Such an approach is suitable for incorporating array nonidealities into array processing models and methods.

A novel concept called *equivalence matrix* is also described in this chapter [V, VI]. The equivalence matrix establishes a connection between vector spherical harmonics and 2-D Fourier basis as well as a one-to-one relationship between their spectra. The equivalence matrix is employed in order to reformulate wavefield modeling and manifold separation in terms of 2-D Fourier basis. This facilitates deriving FFT-based or polynomial rooting-based array processing methods that are applicable regardless of the sensor array geometry and nonidealities. A novel fast spherical harmonic transform using the 2-D FFT is also proposed in this chapter. Novel sampling theorems on the sphere for equiangular sampling schemes, e.g. the Chebyshev rule, are also found by employing the equivalence matrix. Denoising of spherical data on the 2-D Fourier domain is achieved by using the equivalence matrix as well.

The equivalence matrix is suitable in any application that deals with data defined on a spherical manifold including geodesy [12, 175], medical image processing, computer graphics, radioastronomy and cosmology [17, 89] as well as measurement-based radio channel modeling and related array processing tasks [80, 133, 138].

4.1 Wavefield modeling and manifold separation for scalar-fields

Consider a propagating wavefield of the form:

$$\Psi(t, \boldsymbol{r}_n) = \int_{S^1} \varrho(t, \varphi)\, \mathrm{e}^{\mathrm{j}\, \boldsymbol{\kappa}^T \boldsymbol{r}_n} d\varphi, \tag{4.1}$$

where $\boldsymbol{r}_n = [R_n, \varphi_n]^T$ and $\varrho(t, \varphi) \in \mathbb{C}$ denote a point in the xy-plane and an angular signal distribution known as *radiation density* [28], respectively. Expression (4.1) may be used to describe spatially distributed sources due e.g., to scattering as well as point-sources. In the latter case we may write $\varrho(t, \varphi) = \sum_{p=1}^{P} s_p(t)\delta(\varphi_p - \varphi)$, denoting a spatial line-spectrum. Similarly to the wavefield decomposition used in beamspace transform in Chapter 3, wavefields of the form in (4.1) and corresponding radiation densities may be expressed in terms of an orthogonal expansion [28]:

$$\Psi(t, \boldsymbol{r}_n) = \sum_{m=-\infty}^{+\infty} \psi_m(t)\, h_m(\boldsymbol{r}_n), \tag{4.2a}$$

$$\varrho(t, \varphi) = \sum_{m=-\infty}^{+\infty} \psi_m(t)\, d_m(\varphi). \tag{4.2b}$$

Expressions (4.2a) and (4.2b) are related to (4.1) by the expansion coefficients $\{\psi_m(t)\}_{m=-\infty}^{+\infty}$ as follows:

$$\psi_m(t) = \frac{1}{\mathrm{j}^m \sqrt{2\pi} J_m(\kappa R_n)} \int_{S^1} \Psi(t, \boldsymbol{r}_n)\, \mathrm{e}^{\mathrm{j}m\varphi_n} d\varphi_n \tag{4.3a}$$

$$= \frac{1}{\sqrt{2\pi}} \int_{S^1} \varrho(t, \varphi)\, \mathrm{e}^{\mathrm{j}m\varphi} d\varphi. \tag{4.3b}$$

The spatial basis functions of (4.2a) and (4.2b) are given by $h_m(\boldsymbol{r}_n) = \mathrm{j}^m J_m(\kappa R_n)\, \mathrm{e}^{-\mathrm{j}m\varphi_n}$ and $d_m(\varphi) = \mathrm{e}^{-\mathrm{j}m\varphi}$, respectively. Note that $J_m(\cdot) \in \mathbb{R}$ denotes a Bessel function of the first kind and order m.

For point-sources we have $\psi_m(t) = 1/\sqrt{2\pi} \sum_{p=1}^{P} [\boldsymbol{s}(t)]_p\, \mathrm{e}^{\mathrm{j}m\varphi_p}$. Then, the array output described by wavefield modeling in (3.15) simplifies to:

$$\boldsymbol{x}(t) = \boldsymbol{G} \sum_{p=1}^{P} \boldsymbol{d}(\varphi_p)\, [\boldsymbol{s}(t)]_p + \boldsymbol{n}(t), \tag{4.4a}$$

$$= \boldsymbol{A}(\boldsymbol{\varphi})\, \boldsymbol{s}(t) + \boldsymbol{n}(t), \tag{4.4b}$$

where $\boldsymbol{d}(\varphi) \in \mathcal{H}$ denotes a *Vandermonde* vector composed of spatial Fourier basis. Note that the expression in (4.4b) is the standard array processing model described in Chapter 2.

It follows from (4.4) that the array steering vector has the following expansion [9]:

$$\boldsymbol{a}(\varphi) = \boldsymbol{G}\, \boldsymbol{d}(\varphi), \tag{4.5a}$$

$$\boldsymbol{G} = \int_{S^1} \boldsymbol{a}(\varphi)\, \boldsymbol{d}^H(\varphi) d\varphi. \tag{4.5b}$$

The result in (4.5) is known as *manifold separation* and shows that the array sampling matrix may be interpreted as the spatial Fourier coefficients of the array steering vector. Wavefield modeling thus shows that, for each frequency, the array output is the product between the spatial Fourier coefficients of the array steering vector and those of the propagating wavefield.

The array sampling matrix $\boldsymbol{G}$ has infinitely many columns, and so does the coefficient vector $\boldsymbol{\psi}(t)$. For practical purposes one may only consider a finite number of columns, denoted by $\mathcal{M}$. It is therefore important to quantify the error caused by using an array sampling matrix with $\mathcal{M}$ columns in the array output model (4.4) as well as in the steering vector in (4.5a). In the following, such modeling errors are also compared to the errors due to finite sample effects. Consider the following error-vector:

$$\boldsymbol{\epsilon}(\varphi, \mathcal{M}) = \boldsymbol{a}(\varphi) - \sum_{m=-M}^{M} [\boldsymbol{G}]_m \, [\boldsymbol{d}(\varphi)]_m, \tag{4.6}$$

where $M = (\mathcal{M}-1)/2$. The average squared-error as well as the maximum error caused by employing a truncated array sampling matrix in models (4.4) and (4.5) are:

$$\bar{\epsilon}^2(\mathcal{M}) = \frac{1}{2\pi} \int_{\mathcal{S}^1} \|\boldsymbol{\epsilon}(\varphi, \mathcal{M})\|^2 \, d\varphi, \tag{4.7a}$$

$$\epsilon_{\max}(\mathcal{M}) = \max_{\varphi} \|\boldsymbol{\epsilon}(\varphi, \mathcal{M})\|_1, \tag{4.7b}$$

respectively. These errors can be upper-bounded by [28]:

$$\bar{\epsilon}^2(\mathcal{M}) \leq 2\alpha^2 N \sum_{m=M+1}^{+\infty} J_m^2(\kappa R_{\min}), \tag{4.8a}$$

$$\epsilon_{\max}(\mathcal{M}) \leq 2\alpha N \sum_{m=M+1}^{+\infty} |J_m(\kappa R_{\min})|. \tag{4.8b}$$

In (4.8), $\alpha \in \mathbb{R}$ denotes a constant ($\alpha < \infty$) while $R_{\min} \in \mathbb{R}$ denotes the radius of the smallest circle (in the xy-plane) enclosing the sensor array, including the radiating mounting platform. Since the Bessel functions $J_m(\kappa R_{\min})$ in (4.8) decay superexponentially as $m \to +\infty$ beyond $|m| = \kappa R_{\min}$ [1, Ch.9], both error expressions in (4.7) are $\mathcal{O}(\mathrm{e}^{-\mathcal{M}})$ for $\mathcal{M} > \kappa R_{\min}$. Note that the errors due to finite sample size in the estimation of the array covariance matrix are typically $\mathcal{O}(1/\sqrt{K})$. Consequently, the modeling errors caused by employing a truncated array sampling matrix are negligible for a sufficiently large but finite number of columns $\mathcal{M}$.

The result in (4.8) is called superexponential property of the array sampling matrix, and may be understood by interpreting sensor arrays as spatial filters since it reflects their finite aperture. The sampling matrix $\boldsymbol{G}$ may be seen as the array's spatial frequency response, where the passband, stopband, and cutoff frequencies are approximately given by $|m| < \kappa R_{\min}$, $|m| > \kappa R_{\min}$, and $|m| = \kappa R_{\min}$, respectively. For example, it is well-known that sensor arrays with a large aperture have increased resolution since they sample the propagating wavefield over a large area or volume. This is reflected on the array sampling matrix by an increase of the passband region $|m| < \kappa R_{\min}$, since the radius of the smallest circle enclosing the sensor array increases. A larger number of wavefield coefficients $\{\psi_m(t)\}_{m=-\infty}^{+\infty}$ fall in the passband region of the sampling matrix, increasing the received power and leading to a more accurate description of the propagating wavefield as well as to increased resolution.

It is also useful to note that the result in (4.8) appears in the context of multiple-antenna channel capacity as well [71,117]. There, the number of spatial degrees of freedom, a key quantity that allows a linear increase on the channel capacity, is shown to be limited by the minimum sphere enclosing the employed antenna arrays based on arguments that are similar to the superexponential property of the sampling matrix. This suggests that wavefield modeling and manifold separation may play a fundamental role in any sensor array application.

4.1.1 Relationship to local interpolation of the array calibration matrix

Prior knowledge on the location of the sources generating the received wavefield may be incorporated to the array sampling matrix [28]. This is useful when the sources are known to be confined to an angular sector $\mathcal{C}$. Wavefield modeling and manifold separation are then valid over $\mathcal{C}$, only. The basis functions employed in manifold separation and in obtaining the coefficient vector $\boldsymbol{\psi}(k)$ in wavefield modeling are then orthogonal on the angular sector $\mathcal{C}$ and *not* in whole angular domain $\mathcal{S}^1$. This prevents from using Fourier basis since such basis functions are not, in general, orthogonal on $\mathcal{C}$. Orthogonal basis on an angular sector $\mathcal{C}$ may be obtained from Fourier basis by means of Gram-Schmidt orthogonalization, for example [28].

Let $\boldsymbol{b}_n(\varphi)$ and $\boldsymbol{G}_n$ denote an orthogonal basis set on $\mathcal{C}_n$ and corresponding array sampling matrix, respectively. Also, let $\mathcal{C}_1 \cup \mathcal{C}_2 \ldots \cup \mathcal{C}_n = \mathcal{S}^1$.

Then, manifold separation may also be written as:

$$\boldsymbol{a}(\varphi) = \begin{cases} \boldsymbol{G}_1 \boldsymbol{b}_1(\varphi), & \varphi \in \mathcal{C}_1 \\ \boldsymbol{G}_2 \boldsymbol{b}_2(\varphi), & \varphi \in \mathcal{C}_2 \\ \quad \vdots & \\ \boldsymbol{G}_n \boldsymbol{b}_n(\varphi), & \varphi \in \mathcal{C}_n. \end{cases} \tag{4.9}$$

The above expression is similar to local interpolation of the array calibration matrix, described in Chapter 3. However, using the array sampling matrices in (4.9) may be more convenient than the coefficient matrices obtained in the standard local interpolation approach due to the superexponential decaying property of the former. In fact, using (4.9) one may bound both the average squared-error and maximal error, similarly to (4.8), thus ensuring convergence of the array steering vector expansion [28].

Suppose one *does not* have any prior knowledge regarding the location of the sources generating the received wavefield. One may still consider using local basis for decomposing the array steering vector in a piece-wise manner, such as in (4.9), rather than global basis. Typically, such an approach increases the computational complexity of array processing techniques and may reduce the convergence rate of gradient-based optimization methods. For example, using (4.9) with the root-MUSIC technique requires finding the roots of n different polynomials while the maximum step-size of gradient-based methods is limited by the size of each angular sector $\mathcal{C}$.

Wavefield modeling and manifold separation using global basis, with a single array sampling matrix, are thus generally preferred when a sensor array is to be deployed on an environment where the sources may span the whole angular region. This is the case considered throughout this research work.

4.1.2 Relationship to array mapping techniques

Wavefield modeling and manifold separation provide more insight into array interpolation techniques as well as beamspace transform. Let $\boldsymbol{G} \in \mathbb{C}^{N \times \mathcal{M}}$ and $\bar{\boldsymbol{G}} \in \mathbb{C}^{\bar{N} \times \mathcal{M}}$ denote the truncated array sampling matrices of the employed sensor array and that of the virtual array, respectively. Also, consider the following compact singular value decomposition (SVD) $\boldsymbol{G} = \boldsymbol{U}_G \boldsymbol{\Sigma}_G \boldsymbol{V}_G^H$, where $\boldsymbol{U}_G \in \mathbb{C}^{N \times N}$ and $\boldsymbol{V}_G \in \mathbb{C}^{\mathcal{M} \times N}$ denote the left and right singular vectors, and $\boldsymbol{\Sigma}_G \in \mathbb{C}^{N \times N}$ contain the singular values of $\boldsymbol{G}$. Using manifold separation in the LS formulation of the array interpola-

tion (3.9), described in Chapter 3, yields $\boldsymbol{T}_{\text{ls}} = \bar{\boldsymbol{G}}\boldsymbol{G}^{\dagger}$. Then, by applying the linear transform $\boldsymbol{T}_{\text{ls}}$ to the array output and employing wavefield modeling, results in:

$$\boldsymbol{T}_{\text{ls}}\boldsymbol{x}(k) = \bar{\boldsymbol{G}}\boldsymbol{V}_G\boldsymbol{V}_G^H\boldsymbol{\psi}(k) + \boldsymbol{T}_{\text{ls}}\boldsymbol{n}(k) \tag{4.10a}$$

$$\boldsymbol{y}(k) \approx \bar{\boldsymbol{G}}\boldsymbol{\psi}(k) + \boldsymbol{T}_{\text{ls}}\boldsymbol{n}(k). \tag{4.10b}$$

Thus, array interpolation may be understood as a technique that aims at determining the spatial Fourier coefficients of the wavefield, i.e. the coefficient vector $\boldsymbol{\psi}(k)$, in order to synthesize the output of the virtual array.

Let $\boldsymbol{G}_{\text{uca}}$ denote the sampling matrix of an N-element uniform circular array with radius R. The (n,m)th element of $\boldsymbol{G}_{\text{uca}}$ is [28]

$$[\boldsymbol{G}_{\text{uca}}]_{n,m} = \sqrt{2\pi}\,\mathrm{j}^m J_m(\kappa R)\,\mathrm{e}^{-\mathrm{j}m\frac{2\pi n}{N}}. \tag{4.11}$$

By letting $\boldsymbol{F} \in \mathbb{C}^{N\times\bar{\mathcal{M}}}$ denote a block of the $N\times N$ unitary DFT matrix, and employing wavefield modeling, the beamspace transform may be written as:

$$\boldsymbol{F}^H\boldsymbol{x}(k) = \boldsymbol{F}^H\boldsymbol{G}_{\text{uca}}\boldsymbol{\psi}(k) + \boldsymbol{F}^H\boldsymbol{n}(k) \tag{4.12a}$$

$$\approx \sqrt{N}\boldsymbol{\mathcal{J}}(\kappa R)\bar{\boldsymbol{\psi}}(k) + \boldsymbol{F}^H\boldsymbol{n}(k), \tag{4.12b}$$

where $\boldsymbol{\mathcal{J}}(\kappa R) \in \mathbb{C}^{\bar{\mathcal{M}}\times\bar{\mathcal{M}}}$ is given in (3.11a) and $\bar{\boldsymbol{\psi}}(k) \in \mathbb{C}^{\bar{\mathcal{M}}\times 1}$ denotes a truncated coefficient vector since $\bar{\mathcal{M}} < \mathcal{M}$. Similarly, the Davis transform [24, 25, 88] yields:

$$\frac{1}{\sqrt{N}}\,\boldsymbol{\mathcal{J}}^{-1}(\kappa R)\,\boldsymbol{F}^H\boldsymbol{x}(k) \approx \bar{\boldsymbol{\psi}}(k) + \frac{1}{\sqrt{N}}\,\boldsymbol{\mathcal{J}}^{-1}(\kappa R)\,\boldsymbol{F}^H\boldsymbol{n}(k). \tag{4.13}$$

Beamspace and Davis transform are aiming at exploiting the convenient structure of uniform circular arrays in order to acquire an approximation of the coefficient vector $\boldsymbol{\psi}(k)$ by diagonalizing a block of $\boldsymbol{G}_{\text{uca}}$.

The aforementioned diagonalization approach to determining an approximation of the coefficient vector $\boldsymbol{\psi}(k)$ may be employed in sensor arrays of arbitrary geometries and nonidealities [I]. Let $\boldsymbol{G} \in \mathbb{C}^{N\times\mathcal{M}}$ denote the sampling matrix of a sensor array and $\boldsymbol{J} \in \mathbb{N}^{\bar{\mathcal{M}}\times\mathcal{M}}$ a selection matrix given by $\boldsymbol{J} = [\boldsymbol{0} \,\vdots\, \boldsymbol{I}_{\bar{\mathcal{M}}} \,\vdots\, \boldsymbol{0}]$, where $\bar{\mathcal{M}} \leq N$. The manifold separation based Davis transform may be formulated as [I]:

$$\boldsymbol{T} = \arg\min_{\boldsymbol{T}} \|\boldsymbol{T}\boldsymbol{G}\boldsymbol{F} - \boldsymbol{J}\boldsymbol{F}\|_F^2, \tag{4.14}$$

where $\boldsymbol{F} \in \mathbb{C}^{\mathcal{M}\times\mathcal{M}}$ denotes a DFT matrix. Note that the selection matrix $\boldsymbol{J}$ is found prior to solving (4.14) by model-order selection methods, for

example [22, 126, 147]. The least-squares solution to (4.14) is $\boldsymbol{T}_{\text{ls}} = \boldsymbol{J}\,\boldsymbol{G}^{\dagger}$, and the corresponding linearly transformed array output is given by:

$$\boldsymbol{T}_{\text{ls}}\,\boldsymbol{x}(k) = \boldsymbol{J}\boldsymbol{V}_G\boldsymbol{V}_G^H\boldsymbol{\psi}(k) + \boldsymbol{T}_{\text{ls}}\,\boldsymbol{n}(k) \tag{4.15a}$$

$$\boldsymbol{y}(k) \approx \bar{\boldsymbol{\psi}}(k) + \boldsymbol{T}_{\text{ls}}\,\boldsymbol{n}(k). \tag{4.15b}$$

Typically, $\boldsymbol{T}_{\text{ls}}$ is not a unitary matrix so that pre-whitening may be needed before applying array processing methods to (4.15b). Recall also that the truncated coefficient vector for P point-sources simplifies to $\bar{\boldsymbol{\psi}}(k) = \sum_{p=1}^{P}\bar{\boldsymbol{d}}(\varphi_p)s_p(t)$, where $\bar{\boldsymbol{d}}(\varphi) \in \mathbb{C}^{\bar{\mathcal{M}}\times 1}$ is a *Vandermonde* vector composed of spatial Fourier basis. Array processing methods originally developed for ULAs may thus be applied to sensor arrays of arbitrary geometries using the manifold separation based Davis transform and the resulting array output model (4.15b) [I].

4.2 Wavefield modeling and manifold separation for vector-fields

Additional degrees-of-freedom and sources of diversity are obtained by taking into account the co-elevation angle and polarization of the sources, in addition to their azimuth angles. In multiple-input-multiple-output (MIMO) systems, such degrees-of-freedom can be used for increasing capacity and link reliability in the face of channel fading [117, 138]. Employing arrays with polarization diversity allows one to transmit independent data streams to users that share the same frequency and location but operate with different polarization states. Polarization diversity may be exploited even in line-of-sight (LOS) channels. In global navigation satellite systems (GNSS), the polarization state of electromagnetic waves may also be used in achieving robustness to jammers as well as improving positioning accuracy in indoor environments [8, 19]. One may attenuate jammers that operate at a different polarization state than that of the signal-of-interest (SOI), and may receive multiple copies of the same signal that are independently faded due to their polarization states. In radar, polarization diversity typically leads to improved target detection and tracking by designing waveforms that exploit the polarimetric information of the target and environment [62]. Neglecting the polarization of radio waves typically leads to a performance degradation of array processing tasks [85]. This section considers wavefield modeling and manifold separation in azimuth, elevation, and polarization domains.

Let $\boldsymbol{\Psi}(t, \boldsymbol{r}) \in \mathbb{C}^{2\times 1}$ denote a propagating EM wavefield generated by

narrowband far-field sources. Such a wavefield may take the following form:

$$\boldsymbol{\Psi}(t,\boldsymbol{r}) = \int_{\mathcal{S}^2} \boldsymbol{\varrho}(t,\vartheta,\varphi)\, \mathrm{e}^{\mathrm{j}\boldsymbol{\kappa}^T\boldsymbol{r}}\, d\Omega, \tag{4.16}$$

where $d\Omega = \sin\vartheta\, d\vartheta\, d\varphi$ and $\boldsymbol{\varrho}(t,\vartheta,\varphi) \in \mathbb{C}^{2\times 1}$ denotes the radiation density vector. Both wavefield and radiation density may be uniquely written in terms of the following orthogonal expansions [55, 65, 78]:

$$\boldsymbol{\Psi}(t,\boldsymbol{r}_n) = \sum_{\xi=1}^{+\infty} \psi_\xi(t)\, \boldsymbol{h}_\xi(\boldsymbol{r}_n) \tag{4.17a}$$

$$\boldsymbol{\varrho}(t,\vartheta,\varphi) = \sum_{\xi=1}^{+\infty} \psi_\xi(t)\, \boldsymbol{y}_\xi(\vartheta,\varphi), \tag{4.17b}$$

where $\boldsymbol{r}_n = [R_n, \vartheta_n, \varphi_n]^T$ and $\{\psi_\xi(t)\}_{\xi=1}^{+\infty} \in \mathbb{C}$ denote a point in the 3-d Euclidean space and the expansion coefficients, respectively. In (4.17), $\boldsymbol{h}_\xi(\boldsymbol{r}_n) \in \mathbb{C}^{2\times 1}$ and $\boldsymbol{y}_\xi(\vartheta,\varphi) \in \mathbb{C}^{2\times 1}$ denote the orthogonal basis functions used in decomposing the wavefield and radiation density, respectively. The summation in (4.17) is a compact representation for $\sum_{s=1}^{2}\sum_{\ell=1}^{+\infty}\sum_{m=-\ell}^{+\ell}$ with the corresponding index given by $\xi = 2(\ell(\ell+1)+m-1)+s$. The harmonic indices ℓ and m and called levels and modes, respectively.

The basis functions $\{\boldsymbol{y}_\xi(\vartheta,\varphi)\}_{\xi=1}^{+\infty}$ are known as *vector spherical harmonics*, and are given by [65, 78]:

$$\boldsymbol{y}_{1m\ell}(\vartheta,\varphi) = \frac{1}{\sqrt{\ell(\ell+1)}} \left\{ \frac{1}{\sin\vartheta} \frac{\partial Y_\ell^m(\vartheta,\varphi)}{\partial\varphi} \boldsymbol{e}_\theta - \frac{\partial Y_\ell^m(\vartheta,\varphi)}{\partial\vartheta} \boldsymbol{e}_\phi \right\} \tag{4.18a}$$

$$\boldsymbol{y}_{2m\ell}(\vartheta,\varphi) = \frac{1}{\sqrt{\ell(\ell+1)}} \left\{ \frac{\partial Y_\ell^m(\vartheta,\varphi)}{\partial\vartheta} \boldsymbol{e}_\theta + \frac{1}{\sin\vartheta} \frac{\partial Y_\ell^m(\vartheta,\varphi)}{\partial\varphi} \boldsymbol{e}_\phi \right\}, \tag{4.18b}$$

where $\boldsymbol{e}_\theta, \boldsymbol{e}_\phi \in \mathbb{R}^{2\times 1}$ denote the spherical tangential unit-vectors. In (4.18), $Y_\ell^m(\vartheta,\varphi) = \sqrt{\frac{(2\ell+1)}{4\pi}\frac{(\ell-m)!}{(\ell+m)!}} P_\ell^m(\cos\vartheta)\mathrm{e}^{\mathrm{j}m\varphi}$ denotes a *scalar spherical harmonic*, which is composed of associated Legendre functions $P_\ell^m(\cos\vartheta) \in \mathbb{R}$. The basis functions $\boldsymbol{h}_\xi(\boldsymbol{r})$ in (4.17a) may be obtained by using $\boldsymbol{y}_\xi(\vartheta,\varphi)$ in (4.16); see [Appx. A.1] for details. Vector spherical harmonics form a complete orthonormal basis set in the Hilbert space of tangential vector-fields on the 2-sphere, and are invariant under rotations on $SO(3)$ [78]. In particular, vector spherical harmonics satisfy the following orthonormality property [78]:

$$\int_{\mathcal{S}^2} \boldsymbol{y}_{1m\ell}^H(\vartheta,\varphi)\, \boldsymbol{y}_{1m\ell}(\vartheta,\varphi)\, d\Omega = 1, \quad \int_{\mathcal{S}^2} \boldsymbol{y}_{2m\ell}^H(\vartheta,\varphi)\, \boldsymbol{y}_{2m\ell}(\vartheta,\varphi)\, d\Omega = 1 \tag{4.19a}$$

$$\int_{\mathcal{S}^2} \boldsymbol{y}_{1m\ell}^H(\vartheta,\varphi)\, \boldsymbol{y}_{2m\ell}(\vartheta,\varphi)\, d\Omega = 0, \quad \int_{\mathcal{S}^2} \boldsymbol{y}_{2m\ell}^H(\vartheta,\varphi)\, \boldsymbol{y}_{1m\ell}(\vartheta,\varphi)\, d\Omega = 0. \tag{4.19b}$$

Note that vector spherical harmonics as given in (4.18) may suffer from numerical inaccuracies due to the term $1/\sin\vartheta$. Analytically, such a term does not cause any singularities at the poles since $\frac{1}{\sin\vartheta}\frac{\partial Y_\ell^m(\vartheta,\varphi)}{\partial\varphi}\Big|_{\vartheta=0,\pi} = \text{const.}$ for $m = \pm 1$, and zero otherwise [55, Appx. A1]. However, when computing vector spherical harmonics numerically using (4.18), erroneous results may be obtained due to finite precision arithmetic [78]. This is particularly problematic in synthesis equations since for the analysis expression one may choose a sampling scheme that does not acquire observations at the poles. One approach for avoiding such numerical inaccuracies is to write the term $\frac{1}{\sin\vartheta}\frac{\partial Y_\ell^m(\vartheta,\varphi)}{\partial\varphi}$ as a linear combination of associated Legendre functions, and evaluate such an expression for *each* elevation angle [55, Appx. A1]. An alternative approach is described in Section 4.4 by employing the equivalence matrix as well as the 2-D fast Fourier transform (FFT) [IV, V, VI].

For a wavefield generated by P point-sources, the radiation density vector is [VI, VII]:

$$\boldsymbol{\varrho}(t,\vartheta,\varphi) = \sum_{p=1}^{P} \boldsymbol{v}_p\,[\boldsymbol{s}(t)]_p\,\delta(\varphi-\varphi_p)\,\delta(\cos\vartheta-\cos\vartheta_p), \tag{4.20}$$

where $\boldsymbol{v}_p \in \mathbb{C}^{2\times 1}$ describes the polarization state of the Electric-field generated by the pth source, as described in Chapter 2. The coefficient vector is then given by $[\boldsymbol{\psi}(k)]_\xi = \sum_{p=1}^{P}\left[[\boldsymbol{y}_\theta(\vartheta_p,\varphi_p)]_\xi\,[\boldsymbol{y}_\phi(\vartheta_p,\varphi_p)]_\xi\right]\boldsymbol{v}_p\,[\boldsymbol{s}(k)]_p$ for $\xi = 1,\ldots,+\infty$, and the wavefield modeling reduces to the signal model employed in Chapter 2 [IV, V, VI]:

$$\boldsymbol{x}(k) = \boldsymbol{G}\sum_{p=1}^{P}\left[\boldsymbol{y}_\theta(\vartheta_p,\varphi_p),\,\boldsymbol{y}_\phi(\vartheta_p,\varphi_p)\right]\boldsymbol{v}(\gamma_p,\beta_p)\,[\boldsymbol{s}(k)]_p + \boldsymbol{n}(k) \tag{4.21a}$$

$$= \boldsymbol{A}(\boldsymbol{\vartheta},\boldsymbol{\varphi},\boldsymbol{\gamma},\boldsymbol{\beta})\,\boldsymbol{s}(k) + \boldsymbol{n}(k). \tag{4.21b}$$

In (4.21), vectors $\boldsymbol{y}_\theta(\vartheta,\varphi), \boldsymbol{y}_\phi(\vartheta,\varphi) \in \mathcal{H}$ contain the complex-conjugate vector spherical harmonics, for all indices $\xi = 1,\ldots,+\infty$, in $\boldsymbol{e}_\theta$ and $\boldsymbol{e}_\phi$, respectively. From (4.21), manifold separation is now given by [VI, VII]:

$$\boldsymbol{a}(\vartheta,\varphi,\gamma,\beta) = \boldsymbol{G}\left[\boldsymbol{y}_\phi(\vartheta,\varphi),\,\boldsymbol{y}_\theta(\vartheta,\varphi)\right]\boldsymbol{v}(\gamma,\beta) \tag{4.22a}$$

$$\boldsymbol{G} = \int_{S^2} \boldsymbol{a}_\theta(\vartheta,\varphi)\,\boldsymbol{y}_\theta^H(\vartheta,\varphi) + \boldsymbol{a}_\phi(\vartheta,\varphi)\,\boldsymbol{y}_\phi^H(\vartheta,\varphi)\,d\Omega. \tag{4.22b}$$

Hence, the array sampling matrix contains the vector spherical harmonic coefficients of the array steering vector.

The array steering vector in (4.22) may be considered spatially bandlimited, leading to an array sampling matrix composed of $\mathcal{L}$ columns, where

$\mathcal{L} = 2L^2 + 4L$ and L denotes the bandwidth of (4.22) in the vector spherical harmonic domain. Such an assumption causes a modeling error that is typically negligible compared to finite sample effects as well as measurement and quantization noise. To see this consider the following error vectors:

$$\boldsymbol{\epsilon}_\theta(\vartheta, \varphi, L) = \boldsymbol{a}_\theta(\vartheta, \varphi) - \sum_{\xi=1}^{\mathcal{L}} [\boldsymbol{G}]_\xi \, [\boldsymbol{y}_\theta(\vartheta, \varphi)]_\xi, \tag{4.23a}$$

$$\boldsymbol{\epsilon}_\phi(\vartheta, \varphi, L) = \boldsymbol{a}_\phi(\vartheta, \varphi) - \sum_{\xi=1}^{\mathcal{L}} [\boldsymbol{G}]_\xi \, [\boldsymbol{y}_\phi(\vartheta, \varphi)]_\xi. \tag{4.23b}$$

The following average-squared error and maximum errors

$$\bar{\epsilon}^2(L) = \frac{1}{4\pi} \int_{\mathcal{S}^2} \|\boldsymbol{\epsilon}_\theta(\vartheta, \varphi, L)\|^2 + \|\boldsymbol{\epsilon}_\phi(\vartheta, \varphi, L)\|^2 \, d\Omega, \tag{4.24a}$$

$$\epsilon_{\max}(L) = \max_{(\vartheta,\varphi)} \|\boldsymbol{\epsilon}_\theta(\vartheta, \varphi, L)\|_1 + \|\boldsymbol{\epsilon}_\phi(\vartheta, \varphi, L)\|_1, \tag{4.24b}$$

are bounded by the following expressions:

$$\bar{\epsilon}^2(L) \leq N\alpha^2 \sum_{\ell=L+1}^{+\infty} (2\ell+1) \left(j_\ell^2(\kappa R_{\min}) + \left(j_{\ell-1}(\kappa R_{\min}) - \frac{\ell}{\kappa R_{\min}} j_\ell(kR_{\min}) \right)^2 \right), \tag{4.25a}$$

$$\epsilon_{\max}(L) \leq N\alpha \sum_{\ell=L+1}^{+\infty} (2\ell+1) \left(|j_\ell(\kappa R_{\min})| + \left| j_{\ell-1}(\kappa R_{\min}) - \frac{\ell}{\kappa R_{\min}} j_\ell(kR_{\min}) \right| \right), \tag{4.25b}$$

see [Appx. A.1] for details. Here, $R_{\min} \in \mathbb{R}$ denotes the radius of the smallest sphere enclosing the antenna array and $j_\ell(\cdot) \in \mathbb{R}$ denotes a spherical Bessel function of the first kind and order ℓ [1, Ch. 10]. The upper-bounds in (4.25) assume that the number of terms in the summation in the right-hand-side of (4.23) satisfy the following condition $L > \lceil \kappa R_{\min} \rceil$. Note also that the spherical Bessel function $j_\ell(\kappa R_{\min})$ decays *superexponentially* as $\ell \to +\infty$ beyond $\ell = \kappa R_{\min}$ [28]. Hence, the modeling errors caused by employing an array sampling matrix composed of $\mathcal{L}$ columns are $\mathcal{O}(\mathrm{e}^{-cL})$ for $L > \lceil \kappa R_{\min} \rceil$, where $\mathcal{L} = 2L^2 + 4L$ and $c \geq 1$ denotes a positive constant. Recall that the errors due to finite sample effects are typically $\mathcal{O}(1/\sqrt{K})$.

Figure 4.1 illustrates the error expressions in (4.24) and corresponding upper-bounds in (4.25) for a uniform circular array composed of EM vector-sensors. Results show that wavefield modeling and manifold separation may employ an array sampling matrix composed of $\mathcal{L}$ columns, given that $\ell > \lceil \kappa R_{\min} \rceil$, since the modeling errors are negligible. In the remainder of this thesis, and unless explicitly stated, the array sampling

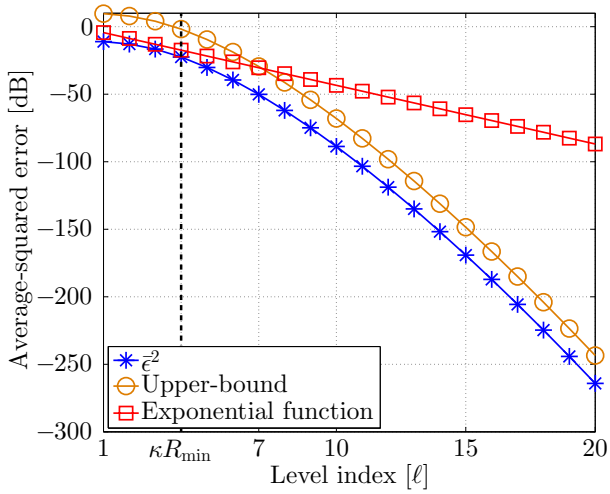

(a) Average-squared modeling error.

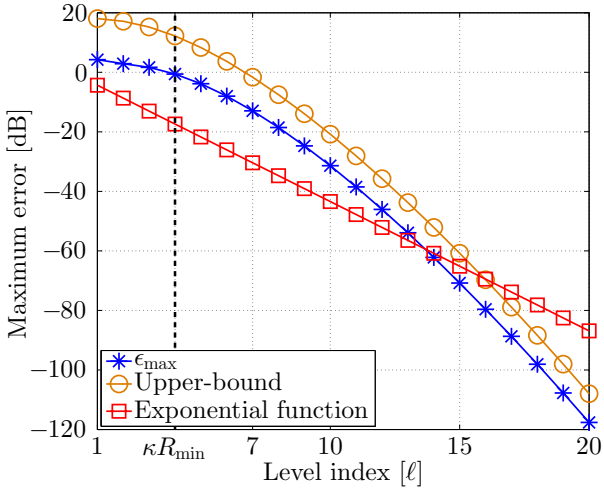

(b) Maximum modeling error.

Figure 4.1. Array steering vector modeling errors caused by employing a sampling matrix composed of $\mathcal{L}(\mathcal{L} = 2\ell^2 + 4\ell)$ columns. The exponential function $\mathrm{e}^{-\ell}$ is illustrated for comparison. A uniform circular array composed of 8 EM vector-sensors is considered. The inter-element spacing is $\lambda/2$. Results show that both average-squared error and maximum error decay superexponentially as $\ell \to +\infty$ beyond $\ell > \lceil \kappa R_{\min} \rceil$. Wavefield modeling and manifold separation may thus be employed with an array sampling matrix composed of $\mathcal{L}$ columns, given that $\ell > \lceil \kappa R_{\min} \rceil$, since the modeling errors are negligible.

matrix $\boldsymbol{G}$ is assumed to be composed of $\mathcal{L}$ columns, and similarly for vectors $\boldsymbol{y}_\theta(\vartheta, \varphi), \boldsymbol{y}_\phi(\vartheta, \varphi)$.

Wavefield modeling and manifold separation may also be extended to near-field scenarios, where both the curvature of the wavefront and ra-

dial component of the EM wavefield needs to be considered. In fact, the approach of writing the transmitting and receiving antenna characteristics in the near-field in terms of an orthogonal expansion forms the basis of *spherical near-field antenna measurements* [55, 76, 108, 158, 159]. Note also that the results regarding wavefield modeling and manifold separation for vector-fields provided in this section may be seen as an extension of the phase-mode excitation principle and beamspace transform to polarization sensitive antenna arrays.

4.3 Sampling matrix estimation

The array sampling matrix may be found in a closed-form using (4.22b). Such an approach may be understood as a vector spherical harmonic transform (VSHT) of each array element, and requires a closed-form expression for the array steering vector. However, such closed-form expressions are often unavailable for real-world antenna arrays since they require a model describing the complex EM interactions occurring on antenna arrays built in practice. Even if a closed-form expression for the array steering vector is acquired, it may be rather tedious and extremely challenging to find the sampling matrix analytically.

This section addresses the estimation of the sampling matrix from array calibration measurements. Two estimators are considered, namely, a least-squares estimator and an estimator that is based on a discrete vector spherical harmonic transform (DVSHT) [42, 78, 119], [IV, V, VI]. Their statistical properties are also considered. The methods described herein are also applicable when the array response is obtained from numerical EM software, or even in cases when the array response is described in a closed-form. Consequently, the effort of solving (4.22b) analytically for each and every antenna array is avoided.

4.3.1 Least-squares estimator

Let $\boldsymbol{B} = [\boldsymbol{B}_\theta, \boldsymbol{B}_\phi] \in \mathbb{C}^{N\times 2Q}$ denote the array calibration matrix obtained by calibration measurements, as described in Chapter 3. Matrix $\boldsymbol{B}$ is composed of the measured array responses from $Q_a \in \mathbb{N}$ azimuth angles and $Q_e \in \mathbb{N}$ co-elevation angles for both vertically and horizontally polarized wavefields. Such array responses are denoted by $\boldsymbol{B}_\theta \in \mathbb{C}^{N\times Q}$ and $\boldsymbol{B}_\phi \in \mathbb{C}^{N\times Q}$, respectively. The number of points on the 2-sphere is de-

noted by $Q = Q_a Q_e$. Using manifold separation for vector-fields, the array calibration matrix may be written as follows [V, VI]:

$$\boldsymbol{B} = \boldsymbol{G}\,\boldsymbol{Y} + \boldsymbol{\mathcal{E}}, \tag{4.26}$$

where $\boldsymbol{Y} \in \mathbb{C}^{\mathcal{L}\times 2Q}$ and $\boldsymbol{\mathcal{E}} \in \mathbb{C}^{N\times 2Q}$ denote matrices composed of vector spherical harmonics and calibration measurement noise, respectively. Recall that matrix $\boldsymbol{G} \in \mathbb{C}^{N\times\mathcal{L}}$ denotes the array sampling matrix. Matrices $\boldsymbol{Y}$ and $\boldsymbol{\mathcal{E}}$ are given by:[1]

$$\boldsymbol{Y} = [\boldsymbol{y}_\theta(\vartheta_1,\varphi_1),\,\cdots,\,\boldsymbol{y}_\theta(\vartheta_{Q_e},\varphi_{Q_a}),\,\boldsymbol{y}_\phi(\vartheta_1,\varphi_1),\,\cdots,\,\boldsymbol{y}_\phi(\vartheta_{Q_e},\varphi_{Q_a})], \tag{4.27a}$$

$$\boldsymbol{\mathcal{E}} = [\boldsymbol{\varepsilon}_\theta(1,1),\,\cdots,\,\boldsymbol{\varepsilon}_\theta(Q_e,Q_a),\,\boldsymbol{\varepsilon}_\phi(1,1),\,\cdots,\,\boldsymbol{\varepsilon}_\phi(Q_e,Q_a)]. \tag{4.27b}$$

The task at hand is to estimate the array sampling matrix $\boldsymbol{G}$ from (4.26). Assuming that the number of calibration points is larger than the number of columns of the array sampling matrix, i.e. $2Q > \mathcal{L}$ (an overdetermined system of equations), expression (4.26) may be seen as a low-rank model for array calibration measurements. The part of the observations describing the array response is confined to a subspace of dimension $N\mathcal{L}$ of the $2NQ$-dimensional complex measurement space. Describing real-world arrays in terms of $\boldsymbol{G}$ rather than $\boldsymbol{B}$ facilitates denoising array calibration measurements as well as compressing the antenna array response in an angle-independent manner [9, 22], [V, VI].

Consistent estimation and identifiability of the sampling matrix from array calibration measurements requires that the number of columns of $\boldsymbol{G}$, denoted by $\mathcal{L}$, is known and the condition $2Q \geq \mathcal{L}$ holds. The latter condition is typically satisfied in practice since calibration measurements usually oversample the antenna array under consideration [55, 84]. Here, oversampling means that the number samples employed in calibration measurements is larger than the strictly necessary to avoid aliasing. Oversampling reduces the estimation variance of the measured array responses since array calibration is always corrupted by measurement noise. The number of columns of the array sampling matrix may be estimated using state-of-the-art model order techniques, such as the minimum description length (MDL), the Bayesian information criterion (BIC), or the exponentially embedded families (EEF) [22, 68, 126, 147]. One approach for relaxing the condition $2Q \geq \mathcal{L}$ is obtained by assuming that

[1] In calibration measurements the transmitted signals are assumed known and therefore not explicitly considered herein for the sake of clarity; see expression (3.5).

the array sampling matrix is random, obeying a known prior distribution, and estimating $\boldsymbol{G}$ using Bayesian methods [69]. This thesis work assumes that the array sampling matrix is an unknown deterministic quantity, and the condition $2Q \geq \mathcal{L}$ is assumed herein.

When the assumption above hold, and matrix $\boldsymbol{Y}$ in (4.26) is of full row-rank, the least-squares estimator (LSE) of the array sampling matrix is:

$$\hat{\boldsymbol{G}}_{\text{lse}} = \boldsymbol{B}\,\boldsymbol{Y}^{\dagger}. \tag{4.28}$$

In case the columns of the measurement noise matrix $\boldsymbol{\mathcal{E}}$ in (4.27b) are i.i.d. zero-mean complex-circular Gaussian distributed, the estimator in (4.28) is also an MLE. The estimator $\hat{\boldsymbol{G}} \in \mathbb{C}^{N\times\mathcal{L}}$ is unbiased and the error covariance matrix is given by:

$$\begin{aligned}\boldsymbol{C}_{\text{lse}} &\triangleq \mathbb{E}\left\{(\text{vec}\{\hat{\boldsymbol{G}}_{\text{lse}}^{T}\} - \text{vec}\{\boldsymbol{G}^{T}\})(\text{vec}\{\hat{\boldsymbol{G}}_{\text{lse}}^{T}\} - \text{vec}\{\boldsymbol{G}^{T}\})^{H}\right\} \\ &= \sigma_{\text{cal}}^{2}\boldsymbol{I}_{N} \otimes (\boldsymbol{Y}^{*}\boldsymbol{Y}^{T})^{-1}.\end{aligned} \tag{4.29}$$

Ensuring that matrix $\boldsymbol{Y}$ in (4.26) is full row-rank typically requires employing an appropriate sampling grid in calibration measurements. Such a sampling grid may be designed so that the Gramian matrix $\boldsymbol{Y}^{*}\boldsymbol{Y}^{T}$ is well-conditioned. However, such an approach may lead to sampling grids that are not practical due to limitations of the positioner employed in array calibration measurements. A common rule of thumb is the choice of an equiangular sampling scheme since it is practical. The number of samples should satisfy $2Q \gg \mathcal{L}$ [123, 159], [55, Ch. 4]. A more rigorous approach for determining the minimum number of calibration points, given an antenna array described by a sampling matrix composed of $\mathcal{L}$ columns, employs a discrete vector spherical harmonic transform. Such an approach is described next.

4.3.2 Discrete vector spherical harmonic transform

An alternative approach to the LSE is based on the discrete vector spherical harmonic transform (DVSHT) and numerical integration on the 2-sphere. The integration needed in the vector spherical harmonic transform in (4.22b) may be done numerically by means of appropriate sampling grids and weights, given that the integrand function is bandlimited in the spherical harmonic domain. Examples of such sampling grids and weights, also known as quadrature rules, include the Chebyshev rule, Gauss-Legendre rule, and Lebedev rule [12, 42, 78, 119].

Discrete vector spherical harmonic transform is analogous to the discrete Fourier transform of one-dimensional bandlimited periodic signals. Topologically, such signals may be understood as being defined on a circle or 1-sphere. The quadrature rule is the well-known equidistant sampling over one period where the weights are given by the inverse of the total number of samples. The DVSHT deals with discrete signals on a spherical manifold. It differs from the 2-D DFT since the latter considers signals defined on the torus[2]. Indeed, 2-D periodic signals on the plane may be understood as being defined on the torus [175]. A more detailed discussion regarding signals defined on the 2-sphere and torus is included in sections 4.4.2 – 4.4.4.

Let matrix $\boldsymbol{Y} \in \mathbb{C}^{\mathcal{L}\times 2Q}$ be composed of vector spherical harmonics, as given in (4.27a), and discretized according to a quadrature rule on the 2-sphere. Also, let the diagonal matrix $\boldsymbol{W} \in \mathbb{R}^{Q\times Q}$ contain the weights for the corresponding quadrature rule. The array sampling matrix estimator based on the DVSHT is given by:

$$\hat{\boldsymbol{G}}_{\text{dvsht}} = \boldsymbol{B}\,(\boldsymbol{I}_2 \otimes \boldsymbol{W})\,\boldsymbol{Y}^H. \tag{4.30}$$

Employing quadrature rules ensures that the discretized vector spherical harmonics are orthogonal in the sense that $\boldsymbol{Y}(\boldsymbol{I}_2\otimes\boldsymbol{W})\boldsymbol{Y}^H = \boldsymbol{I}_{\mathcal{L}}$. Assuming that the columns of matrix $\boldsymbol{\mathcal{E}}$ in (4.27b) are i.i.d. and obey a multivariate zero-mean complex-circular Gaussian distribution with covariance $\boldsymbol{C}_{\mathcal{E}} = \sigma^2_{\text{cal}}\boldsymbol{I}_N$, the estimator in (4.30) is unbiased with an error covariance matrix given by:

$$\boldsymbol{C}_{\text{dvsht}} = \sigma^2_{\text{cal}}\boldsymbol{I}_N \otimes \boldsymbol{Y}^*(\boldsymbol{I}_2 \otimes \boldsymbol{W}^2)\boldsymbol{Y}^T. \tag{4.31}$$

Typically, the error variance of (4.30) is larger than that of (4.28). However, the excess variance of the array sampling matrix estimator based on DVSHT is often not significant, as illustrated in Fig. 4.2. The major advantage of using $\hat{\boldsymbol{G}}_{\text{dvsht}}$ rather than $\hat{\boldsymbol{G}}_{\text{lse}}$ is the ability to determine the minimum number of calibration points Q that are needed in order to uniquely estimate an array sampling matrix composed of $\mathcal{L}$ columns.

For an array sampling matrix composed of $\mathcal{L}(\mathcal{L} = 2L^2+4L)$ columns, the Chebyshev rule requires a minimum of $Q_a = 2(L+1)$ points in azimuth and $Q_e = 2L+3$ points in co-elevation [42, 78, 119]. On the other hand, $Q_a = 2(L+1)$ points in azimuth and $Q_e = (L+1)$ points in co-elevation suffice when employing the Gauss-Legendre rule [42, 119]. Other quadrature rules available in the literature may require a minimum of $Q = (L+1)^2$

[2]This is a torus as it is commonly understood, and not a degenerate torus.

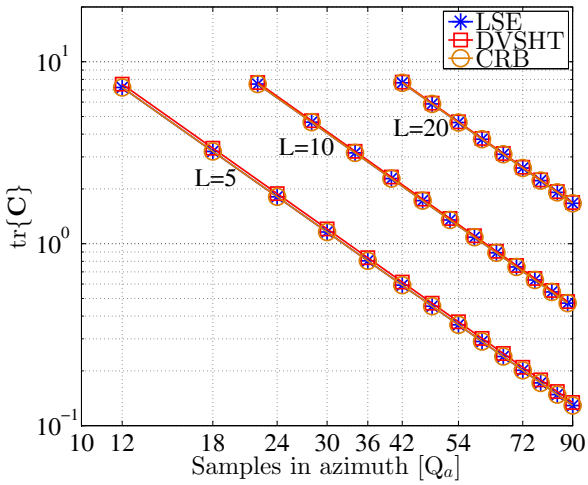

(a) Chebyshev (equiangular) sampling grid.

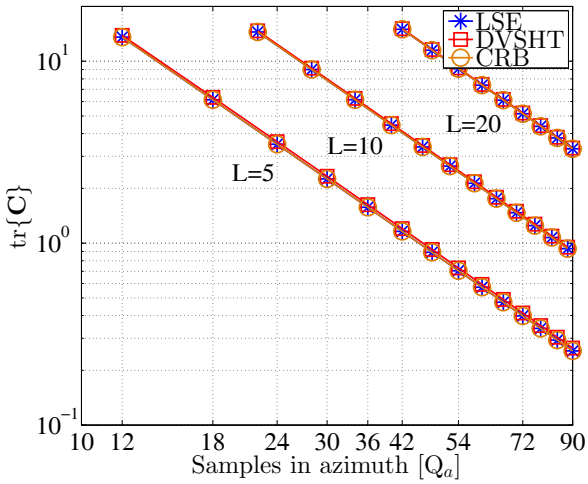

(b) Gauss-Legendre sampling grid.

Figure 4.2. Estimation variance of array sampling matrix estimators and corresponding CRB. Results are given for an array sampling matrix of 5 levels ($\mathcal{L} = 75$), 10 levels ($\mathcal{L} = 240$), and 20 levels ($\mathcal{L} = 880$). The excess variance of the sampling matrix estimator based on DVSHT is negligible since the plots overlap with the CRB.

points on the 2-sphere but the sampling grids following from such schemes are typically not practical and may not be exact since they *do not* ensure that the following orthogonality condition holds: $\boldsymbol{Y}(\boldsymbol{I}_2 \otimes \boldsymbol{W})\boldsymbol{Y}^H = \boldsymbol{I}_{\mathcal{L}}$ [119].

The Chebyshev rule is extremely useful in array calibration measurements since it employs an equiangular sampling scheme in both co-eleva-

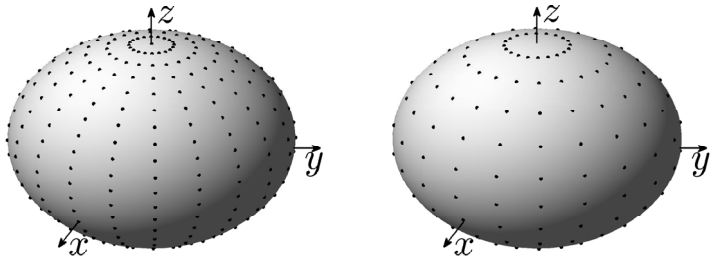

(a) Chebyshev (equiangular) grid. **(b)** Gauss-Legendre grid.

Figure 4.3. Quadrature grids on the 2-sphere employed in this thesis work. The minimum number of points employed by the Gauss-Legendre grid that is needed to uniquely estimate a sampling matrix from array calibration measurements is close to half than that of the Chebyshev grid but the latter is more practical for array calibration measurements.

tion and azimuth angles. Other equally useful rules that employ similar sampling schemes may be found in [59, 78, 101]. In particular, the equivalence matrix, described in Section 4.4, is the key quantity in the quadrature rule proposed in [101]. The equiangular grid may be written as:

$$\vartheta_{q_e} = \frac{\pi q_e}{Q_e - 1}, \quad q_e = 0, \ldots, Q_e - 1, \tag{4.32a}$$

$$\varphi_{q_a} = \frac{2\pi q_a}{Q_a}, \quad q_a = 0, \ldots, Q_a - 1. \tag{4.32b}$$

The corresponding Chebyshev weights are [42]:

$$w_{q_e} = \frac{2}{Q_e - 1} h(q_e, Q_e - 1) \sum_{q=0}^{Q_a/2} h(q, Q_a/2) \frac{2}{1 - 4q^2} \cos\left(\frac{2\pi q_e q}{Q_a}\right) \tag{4.33a}$$

$$w_{q_a} = \frac{2\pi}{Q_a}, \tag{4.33b}$$

where $h(q, Q)$ is a function that equals '$1/2$' for $q = 0, Q$, and '1', otherwise.

The Gauss-Legendre rule employs a sampling grid that is equiangular in azimuth only. The sampling grid and weights along co-elevation are found from the roots of Legendre polynomials. Let $\{x_{q_e}\}_{q_e=0}^{Q_e-1} \in \mathbb{R}$ denote the roots of the Q_eth-degree Legendre polynomial, denoted by $P_{Q_e}(x) \in \mathbb{R}$. Note that Legendre polynomials and the associated Legendre functions used in (4.18) are related as follows $P_\ell(x) = P_\ell^0(x)$, where $x = \cos\vartheta$. Consequently, the sampling grid for the Gauss-Legendre rule is then given by [1, Ch.25]:

$$\vartheta_{q_e} = \arccos(x_{q_e}), \quad q_e = 0, \ldots, Q_e - 1, \tag{4.34a}$$

$$\varphi_{q_a} = \frac{2\pi q_a}{Q_a}, \quad q_a = 0, \ldots, Q_a - 1, \tag{4.34b}$$

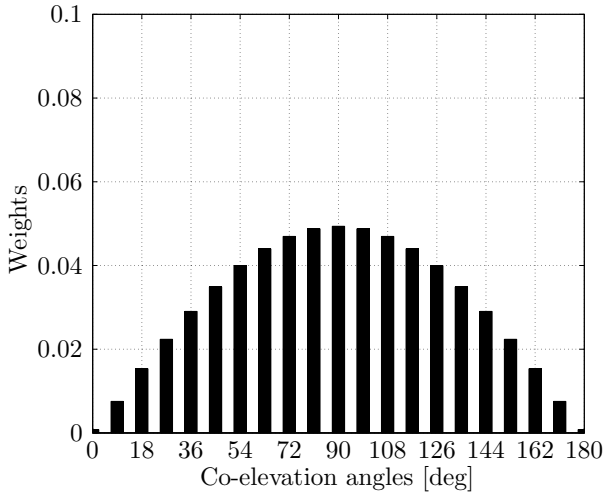

(a) Quadrature weights along co-elevation for the equiangular or Chebyshev rule.

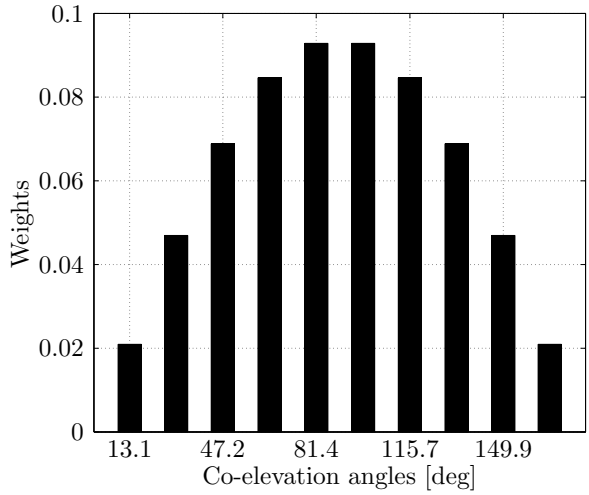

(b) Quadrature weights along co-elevation for the Gauss-Legendre rule.

Figure 4.4. Quadrature weights on the 2-sphere employed in this thesis work. Only the weights along co-elevation angle are shown. For a fixed co-elevation angle the weights along azimuth angle are identical.

while the corresponding weights are [1, Ch.25]:

$$w_{q_e} = \frac{2}{(1-x_{q_e}^2)(\partial P_{Q_e}(x)/\partial x|_{x=x_{q_e}})^2}, \qquad w_{q_a} = \frac{2\pi}{Q_a}. \tag{4.35a}$$

The Chebyshev and Gauss-Legendre sampling grids are illustrated in Fig. 4.3 while the corresponding weights along co-elevation are shown in Fig. 4.4.

In the next section, a novel computationally-efficient method for finding the DVSHT is described. It is an additional contribution to the work in [IV, V, VI]. The method is based on the equivalence matrix and assumes an equiangular sampling scheme such as (but not necessarily) the Chebyshev rule. The equivalence matrix provides more insight into discrete spherical harmonic transforms. It is also shown that the equivalence matrix contains the coefficients of the Legendre polynomials, thus facilitating the computation of the Gauss-Legendre sampling grid and weights.

4.4 Equivalence matrix

Vector spherical harmonics may be written in terms of a 2-D Fourier series [IV, V, VI]. In a matrix-vector notation, the coefficients of such a decomposition are contained in a matrix that is called *equivalence matrix* [IV]. The equivalence matrix plays a fundamental role in numerous applications that deal with data on a spherical manifold including harmonic analysis and spectral estimation on the sphere, measurement-based radio channel modeling [133, 138], 3-D beamforming, and related array processing tasks [80]. The equivalence matrix is an original contribution of this thesis work. It is proposed and further studied in the following publications [IV, V, VI]. This section describes the key concepts and results regarding the equivalence matrix while Chapter 5 considers such a quantity in the context of computationally-efficient signal processing methods for arbitrary array geometries.

The equivalence matrix shows that both the LS and the DVSHT based array sampling matrix estimators, described in Section 4.3, may be written in terms of 2-D Fourier basis. Such estimators may be implemented using the 2-D FFT given that an equiangular sampling scheme is employed. A by-product of such a result is that a novel fast spherical harmonic transform that is based on the 2-D FFT may be derived. This is an important result since many of the applications employing discrete spherical harmonic transforms may take full advantage of the robustness and efficiency of fast Fourier transform based computations. The equivalence matrix may also be employed in order to reformulate wavefield modeling and manifold separation in terms of 2-D Fourier basis. Such a result gives a rigorous theoretical foundation for using the 2-D *effective aperture distribution function* (EADF) in any array processing application. The 2-D EADF is a 2-D DFT of the "full-periodic" array calibration matrix. It is

widely used in measurement-based radio channel modeling as well as in related array processing tasks [42, 43, 84, 86, 125, 133].

4.4.1 Concepts and definitions

Let $\boldsymbol{y}_\theta(\vartheta,\varphi) \in \mathbb{C}^{\mathcal{L}\times 1}$ and $\boldsymbol{y}_\phi(\vartheta,\varphi) \in \mathbb{C}^{\mathcal{L}\times 1}$ be composed of vector spherical harmonics up to level L, or index $\mathcal{L} = 2L^2 + 4L$. Also, let $\boldsymbol{d}(\vartheta,\varphi) \in \mathbb{C}^{\mathcal{M}\times 1}$ denote a vector composed of 2-D Fourier basis, where $\mathcal{M} = (2L+1)^2$. Such a vector may written as $\boldsymbol{d}(\vartheta,\varphi) = \boldsymbol{d}(\varphi) \otimes \boldsymbol{d}(\vartheta)$, where $\boldsymbol{d}(\vartheta) \in \mathbb{C}^{\sqrt{\mathcal{M}}\times 1}$ and $\boldsymbol{d}(\varphi) \in \mathbb{C}^{\sqrt{\mathcal{M}}\times 1}$ are Vandermonde vectors comprised of 1-D Fourier basis in co-elevation and azimuth angles, respectively[3]. Vector spherical harmonics and 2-D Fourier basis are related as follows [IV, V, VI]:

$$\boldsymbol{y}_\theta(\vartheta,\varphi) = \boldsymbol{\Xi}_\theta\, \boldsymbol{d}(\vartheta,\varphi), \quad \boldsymbol{y}_\phi(\vartheta,\varphi) = \boldsymbol{\Xi}_\phi\, \boldsymbol{d}(\vartheta,\varphi), \tag{4.36}$$

where matrix $\bar{\boldsymbol{\Xi}} = [\boldsymbol{\Xi}_\theta,\, \boldsymbol{\Xi}_\phi] \in \mathbb{C}^{\mathcal{L}\times 2\mathcal{M}}$ is known as *equivalence matrix* [IV]. A vector spherical harmonic of mode m and degree ℓ may thus be written as a weighted double sum up to Fourier modes $(2\ell+1)$ and $(2m+1)$ in co-elevation and azimuth angles, respectively.

The equivalence matrix may be found in a closed-form or numerically from recurrence expressions [V], [Appx. A.2]. The latter approach is more attractive from a computational viewpoint since it requires only linear operations. In finite precision arithmetic, recurrence expressions may suffer from error propagation but many methods for preventing such numerical instabilities can be found in the literature; see [44] and references therein.

Consider the following three-term recurrence expressions [V]:

$$\boldsymbol{c}_{\ell+1}^m = \frac{2\ell+1}{2(\ell-m+1)}\bar{\boldsymbol{c}}_\ell^m - \frac{\ell+m}{\ell-m+1}\bar{\boldsymbol{c}}_{\ell-1}^m \tag{4.37a}$$

$$\boldsymbol{c}_\ell^{m+1} = \boldsymbol{J}_\ell \left[\mathrm{j}(\ell-m)\bar{\boldsymbol{c}}_\ell^m - 2\mathrm{j}(\ell+m)\bar{\boldsymbol{c}}_{\ell-1}^m\right], \tag{4.37b}$$

where vectors $\bar{\boldsymbol{c}}_\ell^m \in \mathbb{C}^{(2\ell+3)\times 1}$ and $\bar{\boldsymbol{c}}_{\ell-1}^m \in \mathbb{C}^{(2\ell+3)\times 1}$ are given by:

$$\bar{\boldsymbol{c}}_\ell^m = [0, 0, \boldsymbol{c}_\ell^{m^T}]^T + [\boldsymbol{c}_\ell^{m^T}, 0, 0]^T, \quad \bar{\boldsymbol{c}}_{\ell-1}^m = [0, 0, \boldsymbol{c}_{\ell-1}^{m^T}, 0, 0]^T. \tag{4.38}$$

The recurrence expressions in (4.37) may be initialized with $\boldsymbol{c}_0^0 = 1$ and $\boldsymbol{c}_1^0 = [(1/2), 0, (1/2)]^T$, while $\boldsymbol{J}_\ell \in \mathbb{N}^{(2\ell+1)\times(2\ell+3)}$ is a selection matrix that can be found in [V]. Also, let matrices $\boldsymbol{Z}_e, \boldsymbol{Z}_a \in \mathbb{C}^{(\mathcal{L}/2+1)\times\sqrt{\mathcal{M}}}$ be given as

[3] The dimensions of vectors $\boldsymbol{d}(\vartheta)$ and $\boldsymbol{d}(\varphi)$ are assumed identical for the sake of clarity. Hence, $\sqrt{\mathcal{M}}$ is an integer. The results in this thesis work are equally valid for 1-D Fourier vectors with nonidentical dimensions.

follows [V, VI][4,5]:

$$\boldsymbol{Z}_e = \begin{bmatrix} \boldsymbol{c}_0^0 & \vdots & \cdots & \vdots & \boldsymbol{c}_L^L \end{bmatrix}^T, \tag{4.39a}$$

$$\boldsymbol{Z}_a = \begin{bmatrix} 1 & \vdots & \boldsymbol{I}_3 & \vdots & \cdots & \vdots & \boldsymbol{I}_{\sqrt{\mathcal{M}}} \end{bmatrix}^T. \tag{4.39b}$$

Similarly, let matrix $\tilde{\boldsymbol{Z}}_e \in \mathbb{C}^{(\mathcal{L}/2+1)\times\sqrt{\mathcal{M}}}$ be given by:

$$\tilde{\boldsymbol{Z}}_e = \begin{bmatrix} \tilde{\boldsymbol{c}}_0^0 & \vdots & \cdots & \vdots & \tilde{\boldsymbol{c}}_L^L \end{bmatrix}^T, \tag{4.40}$$

where $\tilde{\boldsymbol{c}} \in \mathbb{C}^{(2\ell+1)\times 1}$ is found from the following expression:

$$\tilde{\boldsymbol{c}}_\ell^m = [\boldsymbol{0}, \boldsymbol{I}_{2\ell+1}, \boldsymbol{0}] \left[\frac{\mathrm{j}}{4}(\ell-m+1)(\ell+m)\bar{\boldsymbol{c}}_\ell^{m-1} + \frac{\mathrm{j}}{4}\bar{\boldsymbol{c}}_\ell^{m+1} + \frac{m}{2}\bar{\boldsymbol{c}}_\ell^m \right], \tag{4.41}$$

where m and ℓ denote the mode and level indices, respectively.

The equivalence matrix $\bar{\boldsymbol{\Xi}} \in \mathbb{C}^{\mathcal{L}\times 2\mathcal{M}}$ may be written in terms of the above matrices as follows:

$$\bar{\boldsymbol{\Xi}} = \Bigg[\underbrace{\boldsymbol{C}_\mathcal{L}\boldsymbol{J}_1 \begin{bmatrix} \boldsymbol{J}_2(\boldsymbol{Z}_a \otimes \boldsymbol{C}_y \tilde{\boldsymbol{Z}}_e) \\ \boldsymbol{J}_2(\boldsymbol{Z}_a \otimes \boldsymbol{C}_y \boldsymbol{Z}_e \boldsymbol{C}_e) \end{bmatrix}}_{\boldsymbol{\Xi}_\theta}, \quad \underbrace{\boldsymbol{C}_\mathcal{L}\boldsymbol{J}_1 \begin{bmatrix} -\boldsymbol{J}_2(\boldsymbol{Z}_a \otimes \boldsymbol{C}_y \boldsymbol{Z}_e \boldsymbol{C}_e) \\ \boldsymbol{J}_2(\boldsymbol{Z}_a \otimes \boldsymbol{C}_y \tilde{\boldsymbol{Z}}_e) \end{bmatrix}}_{\boldsymbol{\Xi}_\phi} \Bigg], \tag{4.42}$$

where $\boldsymbol{C}_\mathcal{L} \in \mathbb{R}^{\mathcal{L}\times\mathcal{L}}$ and $\boldsymbol{C}_e \in \mathbb{C}^{\sqrt{\mathcal{M}}\times\sqrt{\mathcal{M}}}$ denote diagonal matrices containing the normalization coefficients $1/\sqrt{\ell(\ell+1)}, \ell = 1, \ldots, L$ in (4.18) and the following vector $[-\mathrm{j}(\sqrt{\mathcal{M}}-1)/2, \ldots, 1, \ldots, \mathrm{j}(\sqrt{\mathcal{M}}-1)/2]^T$, respectively. Moreover, $\boldsymbol{J}_1 \in \mathbb{R}^{\mathcal{L}\times(\mathcal{L}+2)}$ denotes a selection matrix given by:

$$\boldsymbol{J}_1 = \begin{bmatrix} \boldsymbol{0} & \vdots & \boldsymbol{J}_3 & \vdots & \boldsymbol{0} & \vdots & \boldsymbol{J}_4 \end{bmatrix}, \tag{4.43}$$

where $\boldsymbol{J}_3 \in \mathbb{N}^{\mathcal{L}\times\mathcal{L}/2}$ and $\boldsymbol{J}_4 \in \mathbb{N}^{\mathcal{L}\times\mathcal{L}/2}$ are sparse matrices containing a single '1' in all of the columns and in each 'odd' or 'even' row, respectively. Finally, the diagonal matrix $\boldsymbol{C}_y \in \mathbb{C}^{(\mathcal{L}/2+1)\times(\mathcal{L}/2+1)}$ and the selection matrix $\boldsymbol{J}_2 \in \mathbb{N}^{(\mathcal{L}/2+1)\times(\mathcal{L}/2+1)^2}$ in (4.42) may be found in [V].

The equivalence matrix in (4.42) may be computed once in an offline manner, stored, and used when needed by appropriate selection of its columns and rows [V]. Such an approach may require a large amount of storage capacity when $L \gg 1$ but it is computationally efficient, especially in cases when the equivalence matrix is used often. Note also that the equivalence matrix is sparse since the number of nonzero elements is

[4]Note that $\sqrt{\mathcal{M}}$ is an integer. Note also that $\mathcal{L}$ is even so that $\mathcal{L}/2$ is an integer as well.

[5]Note that matrix $\boldsymbol{Z}_a$ is a concatenation of identity matrices. The zero entries of matrix $\boldsymbol{Z}_a$ that are needed in order to have consistent dimensions are not explicitly written for notational convenience.

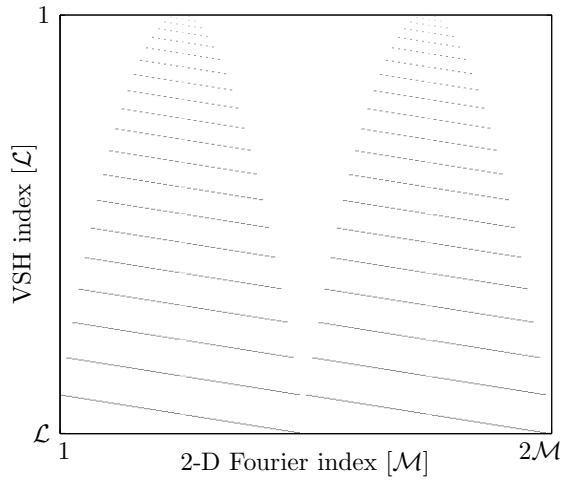

Figure 4.5. Illustration of the structure and sparseness of the equivalence matrix for $L = 20$. Dark entries denote nonzero elements. Typically, less than 2% of all the elements composing the equivalence matrix are nonzero.

$\mathcal{O}(\mathcal{L}^{1.5})$ [V]. Typically, less than 2% of all the entries of the equivalence matrix are nonzero. This follows from the observation that the equivalence matrix may be understood as the 2-D DFT of the "full-periodic" vector spherical harmonics; see [Appx. A.2] for details. Making vector spherical harmonics "full-periodic", which may be understood as extending such basis functions onto the torus, introduces redundancy in the angular domain which is translated into sparseness in the 2-D Fourier domain. The sparsity of the equivalence matrix is a key property for improving the computational complexity of the various methods employing $\bar{\boldsymbol{\Xi}}$, including the fast vector spherical harmonic transform proposed in Section 4.4.4. Figure 4.5 illustrates the structure and sparseness of $\bar{\boldsymbol{\Xi}}$.

4.4.2 Wavefield modeling and manifold separation based on 2-D Fourier basis

Expressions for the sampling matrix estimators, given in Section 4.3, that are based on the 2-D fast Fourier transform may be derived using the equivalence matrix. Also, wavefield modeling and manifold separation may be re-parameterized in terms of 2-D Fourier basis as well as equivalence matrix. In the following, it is assumed that array calibration measurements employ an equiangular sampling grid.

Let $\boldsymbol{\mathcal{B}}_\theta \in \mathbb{C}^{N\times 2(Q-Q_a)}$ and $\boldsymbol{\mathcal{B}}_\phi \in \mathbb{C}^{N\times 2(Q-Q_a)}$ denote the *full-periodic* array calibration matrices corresponding to $\boldsymbol{B}_\theta$ and $\boldsymbol{B}_\phi$, respectively. The

term "full-periodic" means that the array calibration matrices ($\boldsymbol{B}_\theta$ and $\boldsymbol{B}_\phi$) are extended in a manner that the measured co-elevation angle becomes periodic with period 2π. Let $\tilde{\vartheta} \in [0, 2\pi)$ denote such an extended, or periodic, co-elevation angle, and note that the standard array calibration matrices $\boldsymbol{B}_\theta$ and $\boldsymbol{B}_\phi$ are *not* periodic in co-elevation since the standard co-elevation angle is defined as $\vartheta \in [0, \pi]$. The full-periodic calibration matrices $\boldsymbol{\mathcal{B}}_\theta$ and $\boldsymbol{\mathcal{B}}_\phi$ may be obtained by two consecutive calibration measurements or directly from $\boldsymbol{B}_\theta$ and $\boldsymbol{B}_\phi$. The latter approach is more convenient since it does not require additional calibration measurements. In particular, the full-periodic calibration matrices may be obtained by mirroring the standard calibration measurements in the south-pole, rotating the measurements in azimuth by π, and shifting the phase of the data by 180°. Algebraically, such an operation may be accomplished as $\boldsymbol{\mathcal{B}}_\theta = \boldsymbol{B}_\theta \boldsymbol{\mathcal{R}}$, and similarly for $\boldsymbol{\mathcal{B}}_\phi$, where matrix $\boldsymbol{\mathcal{R}} \in \mathbb{N}^{Q \times 2(Q-Q_a)}$ is given by:

$$\boldsymbol{\mathcal{R}} = (\boldsymbol{I}_{Q_a} \otimes [\boldsymbol{I}_{Q_e},\, \boldsymbol{0}]) + \left(\boldsymbol{I}_{Q_a} \otimes \left[\boldsymbol{0},\, -\left[\boldsymbol{0},\, \tilde{\boldsymbol{I}}_{Q_e-2}, \boldsymbol{0} \right]^T \right] \right). \tag{4.44}$$

Matrix $\boldsymbol{\mathcal{R}}$ may be understood as extending a function on the 2-sphere onto the torus.

The least-squares estimator of the array sampling matrix in (4.28) may now be written as follows [Appx. A.3]:

$$\begin{aligned} \hat{\boldsymbol{G}}_{\text{lse}} = \underbrace{\left[\boldsymbol{\mathcal{B}}_\theta \boldsymbol{\mathcal{W}}_{\text{lse}} \boldsymbol{\mathcal{F}}^H \boldsymbol{J},\, \boldsymbol{\mathcal{B}}_\phi \boldsymbol{\mathcal{W}}_{\text{lse}} \boldsymbol{\mathcal{F}}^H \boldsymbol{J} \right]}_{\text{2-D FFTs}} \bar{\boldsymbol{\Xi}}^H \\ \times \left(\bar{\boldsymbol{\Xi}} \left(\boldsymbol{I}_2 \otimes \boldsymbol{J}^T \boldsymbol{\mathcal{F}} \boldsymbol{\mathcal{R}}^T \boldsymbol{C}^2 \boldsymbol{\mathcal{R}} \boldsymbol{\mathcal{F}}^H \boldsymbol{J} \right) \bar{\boldsymbol{\Xi}}^H \right)^{-1}, \end{aligned} \tag{4.45}$$

where $\boldsymbol{\mathcal{F}} \in \mathbb{C}^{2(Q-Q_a) \times 2(Q-Q_a)}$ denotes a 2-D discrete Fourier transform matrix. In (4.45), matrices $\boldsymbol{\mathcal{W}}_{\text{lse}} \in \mathbb{R}^{2(Q-Q_a) \times 2(Q-Q_a)}$ and $\boldsymbol{C} \in \mathbb{R}^{Q \times Q}$ denote diagonal weighting matrices, and $\boldsymbol{J} \in \mathbb{N}^{2(Q-Q_a) \times \mathcal{M}}$ denotes a selection matrix, respectively. These matrices are described in detail in [Appx. A.3]. Note that the matrix product in the right-hand side of (4.45) is full-rank. Similarly, the DVSHT-based array sampling matrix estimator in (4.30) can also be written as follows [Appx. A.3]:

$$\hat{\boldsymbol{G}}_{\text{dvsht}} = \underbrace{\left[\boldsymbol{\mathcal{B}}_\theta \boldsymbol{\mathcal{W}}_{\text{dvsht}} \boldsymbol{\mathcal{F}}^H \boldsymbol{J},\, \boldsymbol{\mathcal{B}}_\phi \boldsymbol{\mathcal{W}}_{\text{dvsht}} \boldsymbol{\mathcal{F}}^H \boldsymbol{J} \right]}_{\text{2-D FFTs}} \bar{\boldsymbol{\Xi}}^H, \tag{4.46}$$

where the diagonal matrix $\boldsymbol{\mathcal{W}}_{\text{dvsht}} \in \mathbb{R}^{2(Q-Q_a) \times 2(Q-Q_a)}$ is composed of quadrature weights such as the Chebyshev weights in (4.33a). Details are given in [Appx. A.3].

Expressions (4.45) and (4.46) show that both least-squares and DVSHT-based sampling matrix estimators may employ the 2-D fast Fourier transform, thus making such methods amenable to practical implementation in

any digital signal processor (DSP). Also, (4.46) gives more insight into the well-known discrete transform for vector spherical harmonics [12, 42, 78]. In particular, the DVSHT may be understood as *inherently* making the spherical data full-periodic, followed by a weighted 2-D DFT and a mapping from the Fourier to the spherical harmonic spectra. These observations hold true for *any* equiangular sampling grid, that includes at least one of the poles, and it is *not* restricted to the Chebyshev rule. Expression (4.46) is a key result in the novel fast spherical harmonic transform described in Section 4.4.4.

Another important consequence of expression (4.45) is that most of quadrature rules that are based on equiangular grids typically employ *more samples than necessary* in order to avoid aliasing. For example, the Chebyshev rule requires $Q_e = 2L+3$ samples in co-elevation angle so that aliasing may be avoided [12, 42, 119]. However, one may observe from (4.45) that such a requirement follows from the inherent convolution between the "full-periodic" data $(\boldsymbol{\mathcal{B}}_\theta, \boldsymbol{\mathcal{B}}_\phi)$ and the corresponding diagonal weighting matrix $\boldsymbol{\mathcal{W}}_{\text{dvsht}}$. Since the bandwidth of $(\boldsymbol{\mathcal{B}}_\theta, \boldsymbol{\mathcal{B}}_\phi)$ in the 2-D Fourier domain is $\mathcal{M} = (2L+1) \times (2L+1)$ [IV, V, VI], the Chebyshev rule needs only to consider $Q_e = L+1$ points in order to avoid aliasing[6]. Hence, a reduction of the number of samples by more than half is obtained. This is the reasoning behind the recent quadrature rule proposed in [101]. However, the method in [101] employs specific quadrature weights while the aforementioned observations hold for any quadrature rule that employs an equiangular grid. A detailed relationship between this thesis work and the method proposed in [101] is established in Section 4.4.4.

A bijective mapping between the array sampling matrix and the 2-D Fourier spectra of the extended (or full-periodic) array steering vectors $\tilde{\boldsymbol{a}}_\theta(\tilde{\vartheta}, \varphi) \in \mathbb{C}^{N\times 1}$ and $\tilde{\boldsymbol{a}}_\phi(\tilde{\vartheta}, \varphi) \in \mathbb{C}^{N\times 1}$ is obtained by employing the equivalence matrix as well [IV, V, VI]:

$$\boldsymbol{G}\,\bar{\boldsymbol{\Xi}} = \boldsymbol{\Phi}, \quad \boldsymbol{G} = \boldsymbol{\Phi}\,\bar{\boldsymbol{\Xi}}^{\dagger}. \tag{4.47}$$

Here, $\boldsymbol{\Phi} \in \mathbb{C}^{N\times 2\mathcal{M}}$ is composed of the 2-D Fourier spectra of the extended array steering vectors as follows $\boldsymbol{\Phi} = [\boldsymbol{\Phi}_\theta, \boldsymbol{\Phi}_\phi]$. In particular, $\boldsymbol{\Phi}_\theta \in \mathbb{C}^{N\times\mathcal{M}}$ and $\boldsymbol{\Phi}_\phi \in \mathbb{C}^{N\times\mathcal{M}}$ denote the 2-D Fourier spectrum of $\tilde{\boldsymbol{a}}_\theta(\tilde{\vartheta}, \varphi)$ and $\tilde{\boldsymbol{a}}_\phi(\tilde{\vartheta}, \varphi)$, respectively. Note that matrices $\boldsymbol{\mathcal{B}}_\theta$ and $\boldsymbol{\mathcal{B}}_\phi$ may be understood as the calibration data of $\tilde{\boldsymbol{a}}_\theta(\tilde{\vartheta}, \varphi)$ and $\tilde{\boldsymbol{a}}_\phi(\tilde{\vartheta}, \varphi)$, respectively. Figure 4.6 illustrates

[6]Note that extending a function on the sphere onto the torus nearly doubles the number of samples.

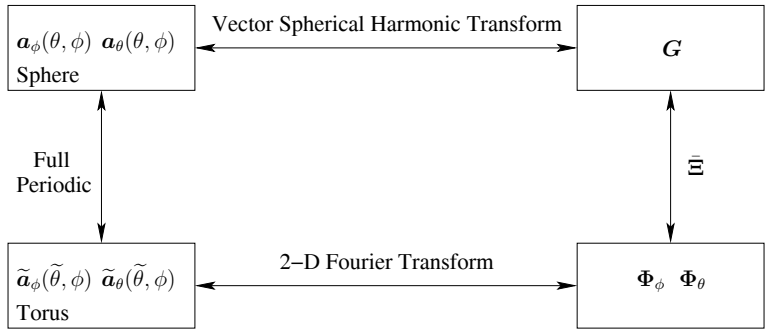

Figure 4.6. Block diagram illustrating the relationship among array steering vectors, extended steering vectors, and their spectra. The equivalence matrix provides a bijective mapping between spherical harmonic spectra and 2-D Fourier spectra.

the relationships among array steering vectors, extended steering vectors, and their spectra.

The result in (4.47) shows that a function defined on the 2-sphere and bandlimited on the spherical harmonic domain is associated with a unique *extended* function defined on the torus and bandlimited on the 2-D Fourier domain. Moreover, their spectra are related in a bijective manner by the equivalence matrix. Even though matrix $\boldsymbol{\Phi}$ has more elements than matrix $\boldsymbol{G}$, i.e. $2N\mathcal{M} > N\mathcal{L}$, the former may be uniquely identified by $N\mathcal{L}$ coefficients [IV, V, VI]. This follows from the result that the rows of $\boldsymbol{\Phi}$ span (or are contained in) the row-space of the equivalence matrix [IV, V, VI]:

$$\mathcal{R}\{\boldsymbol{\Phi}\} \subseteq \mathcal{R}\{\bar{\boldsymbol{\Xi}}\}. \tag{4.48}$$

Note that the dimension of $\mathcal{R}\{\bar{\boldsymbol{\Xi}}\}$ is $\mathcal{L}$. The following results also follow from (4.48) [IV, V, VI]:

$$\boldsymbol{\Phi}\boldsymbol{P}_{\bar{\Xi}} = \boldsymbol{\Phi}, \quad \boldsymbol{\Phi}\boldsymbol{P}_{\bar{\Xi}}^{\perp} = \boldsymbol{0}, \tag{4.49}$$

where $\boldsymbol{P}_{\bar{\Xi}} \in \mathbb{C}^{2\mathcal{M}\times 2\mathcal{M}}$ is an orthogonal projection matrix onto the row-space of the equivalence matrix, and it is given by $\boldsymbol{P}_{\bar{\Xi}} = \bar{\boldsymbol{\Xi}}^{\dagger}\bar{\boldsymbol{\Xi}}$. Similarly, $\boldsymbol{P}_{\bar{\Xi}}^{\perp} = \boldsymbol{I}_{\mathcal{M}} - \boldsymbol{P}_{\bar{\Xi}}$ is a projection matrix onto the orthogonal complement of $\mathcal{R}\{\bar{\boldsymbol{\Xi}}\}$. Note that both $\boldsymbol{P}_{\bar{\Xi}}$ and $\boldsymbol{P}_{\bar{\Xi}}^{\perp}$ are idempotent and Hermitian matrices. The structure of $\boldsymbol{\Phi}$, expressed in (4.48) and (4.49), may be understood as the result of extending a function defined on the 2-sphere onto the torus since such an extension introduces redundancy.

Another result that follows from the equivalence matrix consists in writing the manifold separation in (4.22) as follows [IV, V, VI]:

$$\boldsymbol{a}(\vartheta,\varphi,\gamma,\beta) = [\boldsymbol{\Phi}_\theta, \boldsymbol{\Phi}_\phi]\,(\boldsymbol{I}_2 \otimes \boldsymbol{d}(\vartheta,\varphi))\,\boldsymbol{v}(\gamma,\beta). \tag{4.50}$$

Note that (4.50) is a decomposition of the array steering vector defined on a spherical manifold in terms of 2-D Fourier basis. Similarly to the array sampling matrix $\boldsymbol{G}$, also $\boldsymbol{\Phi}_\theta$ and $\boldsymbol{\Phi}_\phi$ may be found in a closed-form given that an algebraic model for the array steering vector is known. However, a numerical method for finding $\boldsymbol{\Phi}$ may be more useful in practice since it does not rely on closed-form expressions for array steering vectors. In particular, matrix $\boldsymbol{\Phi}$ in (4.50) may be estimated from array calibration measurements using the following constrained least-squares estimator (CLSE) [69, Ch. 8], [53]:

$$\hat{\boldsymbol{\Phi}}_{\text{clse}} = \boldsymbol{B}(\boldsymbol{I}_2 \otimes \boldsymbol{D}^\dagger)\boldsymbol{\mathcal{P}}_{\bar{\Xi}}, \tag{4.51}$$

where $\boldsymbol{D} \in \mathbb{C}^{\mathcal{M}\times Q}$ is a matrix composed of 2-D Fourier basis, and it is given by:

$$\boldsymbol{D} = \left[\boldsymbol{d}(\vartheta_1, \varphi_1), \ldots, \boldsymbol{d}(\vartheta_{Q_e}, \varphi_{Q_a})\right]. \tag{4.52}$$

Moreover, matrix $\boldsymbol{\mathcal{P}}_{\bar{\Xi}} \in \mathbb{C}^{2\mathcal{M}\times 2\mathcal{M}}$ in (4.51) ensures that $\hat{\boldsymbol{\Phi}}_{\text{clse}}$ satisfies the equality constraint in (4.49). Such a matrix is given by:

$$\boldsymbol{\mathcal{P}}_{\bar{\Xi}} = \boldsymbol{I}_{2\mathcal{M}} - (\boldsymbol{P}_{\bar{\Xi}}^{\perp}(\boldsymbol{I}_2 \otimes (\boldsymbol{D}\boldsymbol{D}^H)^{-1})\boldsymbol{P}_{\bar{\Xi}}^{\perp})^\dagger(\boldsymbol{I}_2 \otimes (\boldsymbol{D}\boldsymbol{D}^H)^{-1}). \tag{4.53}$$

In case of calibration measurement noise that is i.i.d. zero-mean complex-circular Gaussian distributed, $\hat{\boldsymbol{\Phi}}_{\text{clse}}$ is statistically efficient in the sense that it achieves the constrained CRB [53].

An important observation is that array processing methods may now employ the steering vector model in (4.50) and exploit the convenient Vandermonde structure of $\boldsymbol{d}(\vartheta, \varphi)$ regardless of the array geometry or nonidealities. This is significantly different from the array mapping techniques described in Chapter 3. In particular, the accuracy of array mapping techniques is limited by the number of elements comprising the real sensor array, and degrades rapidly with increasing sector-size. However, the accuracy of wavefield modeling and manifold separation is limited by the variance of the calibration measurement noise, and not by the number of array elements. Typically, the number of columns of the sampling matrix found by calibration measurements is much larger than the number of array elements. Indeed, in case the sampling matrix is found in a closed-form, wavefield modeling and manifold separation can be as accurate as desired since the number of columns of the sampling matrix can be chosen freely. The cost is an increase of the computational complexity of signal processing methods. Finally, it is important to emphasize that the sampling matrix is *not* sector-dependent since it denotes the spherical har-

monic coefficients of the array elements. Recall that spherical harmonics are global rather than local orthogonal basis functions, and therefore avoid sector-by-sector processing.

4.4.3 Relationship to effective aperture distribution function

The 2-D effective aperture distribution function (EADF) is a 2-D discrete Fourier transform of the "full-periodic" array calibration matrices $\boldsymbol{\mathcal{B}}_\theta$ and $\boldsymbol{\mathcal{B}}_\phi$ [86]. The 2-D EADF is thus an estimate of the 2-D Fourier spectra of the extended array steering vectors $\tilde{\boldsymbol{a}}_\theta(\tilde{\vartheta},\varphi)$ and $\tilde{\boldsymbol{a}}_\phi(\tilde{\vartheta},\varphi)$. The EADF has been widely used in measurement-based radio channel modeling and related array processing tasks [42, 43, 84–86, 125, 132–134]. A decomposition of the extended array steering vector in 2-D Fourier basis has also been employed in direction-finding applications based on power measurements [94–96].

However, a rigorous theoretical analysis regarding the bandlimited assumption of sensor arrays in the 2-D Fourier domain and convergence rate of such an expansion has not been considered in the aforementioned research work. The results in [IV, V, VI], and in particular the equivalence matrix, overcome such a limitation by establishing a relationship between the array sampling matrix $\boldsymbol{G}$ and 2-D Fourier spectrum $\boldsymbol{\Phi}$ of the extended array steering vector. In particular, a sensor array that is modeled by a sampling matrix composed of $\mathcal{L}$ columns may be equally described (with the same modeling error) by matrix $\boldsymbol{\Phi}$, the latter being composed of additional $(6L^2+4L+2)$ columns [IV, V, VI].

The 2-D EADF *does not* exploit the structure of matrix $\boldsymbol{\Phi}$, expressed in (4.48)-(4.49), and therefore it is not a statistically efficient estimator [V]. A simple approach for reducing the estimation variance of the EADF consists in employing the equivalence matrix. In particular, let the 2-D EADF be written as

$$\hat{\boldsymbol{\Phi}}_{\text{eadf}} = [\boldsymbol{\mathcal{B}}_\theta, \boldsymbol{\mathcal{B}}_\phi](\boldsymbol{I}_2 \otimes \boldsymbol{\mathcal{F}}^H \boldsymbol{J}), \tag{4.54}$$

where $\boldsymbol{\mathcal{F}} \in \mathbb{C}^{2(Q-Q_a)\times 2(Q-Q_a)}$ and $\boldsymbol{J} \in \mathbb{N}^{2(Q-Q_a)\times \mathcal{M}}$ denote a unitary 2-D DFT matrix and a selection matrix, respectively. The estimation variance of (4.54) may be reduced by projecting $\hat{\boldsymbol{\Phi}}_{\text{eadf}}$ onto the row-space of the equivalence matrix as follows [V]:

$$\hat{\boldsymbol{\Phi}}_{\Xi} = \hat{\boldsymbol{\Phi}}_{\text{eadf}} \boldsymbol{P}_{\Xi}. \tag{4.55}$$

The estimation variance of (4.55) is strictly smaller than that of (4.54) [V]. This is because the 2-D DFT does not exploit the structure of the 2-D

Fourier spectrum of the extended data $(\boldsymbol{\mathcal{B}}_\theta, \boldsymbol{\mathcal{B}}_\phi)$, expressed in (4.48)-(4.49). Moreover, the estimator $\hat{\boldsymbol{\Phi}}_{\Xi}$ is computationally more attractive than that in (4.51) since it may be implemented by the 2-D FFT. However, the estimator $\hat{\boldsymbol{\Phi}}_{\text{clse}}$ in (4.51) is the method of choice when statistical optimality is the goal.

4.4.4 Fast vector spherical harmonic transform by 2-D FFT

A novel computationally efficient discrete vector spherical harmonic transform may also be derived by using the equivalence matrix [V, VI]. Computational advances in discrete spherical harmonic transforms have been an intensive field of research for the past two decades [27,32,59,78,101,140]. Many areas of engineering deal with data on a spherical manifold, and a computationally-efficient solution to harmonic analysis on the 2-sphere is in some cases the only feasible approach to process the acquired data. Fields of signal processing where data are defined on the 2-sphere include geodesy [12, 175], radioastronomy and cosmology [17, 89], measurement-based radio channel modeling [133, 138], 3-D beamforming and related array processing tasks [80].

Research efforts towards a fast spherical harmonic transform have been mainly focused on computationally-efficient solutions for associated Legendre functions. Indeed, a simple separation of variables makes it possible to employ the fast Fourier transform in azimuth-angle for each point in co-elevation. Such an approach assumes that an equiangular grid in azimuth is employed. Even though fast spherical harmonic transforms for non-equidistant sampling do exist [82], they are typically approximate quadrature rules and may be numerically unstable. Most of fast spherical harmonic transforms thus employ an equiangular grid in both azimuth and co-elevation angles [32,59,78,102]. The most efficient method for discrete spherical harmonic transform has a complexity of $\mathcal{O}(L^2 \log^2 L)$ [59]. However, such a technique assumes that the bandwidth of the signals under consideration is a power of two. Moreover, the technique in [59] is known to be numerically unstable [78]. Indeed, fast spherical harmonic transforms that are exact and known to be stable are still $\mathcal{O}(L^3)$ [78].

The fast spherical harmonic transform that is obtained by employing the equivalence matrix is also $\mathcal{O}(L^3)$ [V, VI]. Nonetheless, it allows one to use the fast Fourier transform in *both* azimuth and co-elevation angles given that an equiangular grid is employed. Even though the complexity remains $\mathcal{O}(L^3)$, using the 2-D FFT leads to significant computational

Table 4.1. Summary of the fast vector spherical harmonic transform based on the equivalence matrix.

Step 1:	Acquire Q samples of both orthogonal tangential components of a vector-valued function $[b_\theta(\vartheta,\varphi), b_\phi(\vartheta,\varphi)]^T$. Denote the sampled components by $\boldsymbol{b}_\theta \in \mathbb{C}^{Q\times 1}$ and $\boldsymbol{b}_\phi \in \mathbb{C}^{Q\times 1}$.
Step 2:	Obtain the "full-periodic" data as $\mathfrak{b}_\theta = \boldsymbol{\mathcal{R}}^T\boldsymbol{b}_\theta$ and $\mathfrak{b}_\phi = \boldsymbol{\mathcal{R}}^T\boldsymbol{b}_\phi$, and weight the data using the diagonal matrix $\boldsymbol{\mathcal{W}}_{\mathrm{dvsht}}$.
Step 3:	Take the 2-D fast Fourier transform as $\tilde{\boldsymbol{f}}_\theta = \mathrm{FFT2}\{\boldsymbol{\mathcal{W}}_{\mathrm{dvsht}}\mathfrak{b}_\theta\}$ and $\tilde{\boldsymbol{f}}_\phi = \mathrm{FFT2}\{\boldsymbol{\mathcal{W}}_{\mathrm{dvsht}}\mathfrak{b}_\phi\}$.
Step 4:	Select the $\mathcal{M}$ Fourier coefficients as $\boldsymbol{f}_\theta = \boldsymbol{J}_1^T\tilde{\boldsymbol{f}}_\theta$ and $\boldsymbol{f}_\phi = \boldsymbol{J}_1^T\tilde{\boldsymbol{f}}_\phi$.
Step 5:	Obtain the vector spherical harmonic coefficients as $\boldsymbol{g} = \bar{\boldsymbol{\Xi}}^*[\boldsymbol{f}_\theta^T, \boldsymbol{f}_\phi^T]^T$.

savings in applications where a few hundreds coefficients are relevant, such as in array processing. Harmonic analysis on the sphere using the 2-D FFT is also convenient from an implementation viewpoint and leads to improved numerical stability. Table 4.1 summarizes the proposed fast vector spherical harmonic transform.

The proposed fast vector spherical harmonic transform has a complexity of $\mathcal{O}(Q\log Q)$ given that $Q \gg L$. The latter condition means that the number of samples Q in the 2-sphere is much larger than the bandwidth L of the observed function. Note that no oversampling may be needed in noise-free scenarios or in cases where the bandwidth of the observed function is known. In cases where the observations are corrupted by measurement noise, or the bandwidth of the function is unknown and needs to be estimated by model order selection methods, oversampling is usually employed. Typically, oversampling leads to reduced estimation variance. Array calibration measurements usually oversample the sensor array under consideration due to the aforementioned reasons [55, 84].

The idea of using the 2-D fast Fourier transform in harmonic analysis on the sphere goes back to [27]. However, the method in [27] is approximate and may lead to discontinuities. Perhaps the first contribution establishing a relationship between spherical harmonic spectra and 2-D Fourier spectra through a "full-periodic" extension of the function defined on the sphere can be found in [140]. It is important to emphasize that the equivalence matrix proposed in this thesis work was found in an independent manner from the result in [140]. Moreover, the work in [140] is restricted to scalar-fields while the equivalence matrix is valid for both

scalar and vector-fields. Note that vector-fields are of high-importance in signal processing using antenna arrays and radio-frequency signals. Also, the structure of the 2-D Fourier spectrum of the extended function is not addressed in [140]. Exploiting such a structure is crucial in obtaining minimum variance estimates, as described in the previous section.

More recently, a novel sampling rule on the 2-sphere has been proposed that has remarkable connections with the equivalence matrix [101]. Indeed, the work in [101] is based on a representation of Wigner D-functions in terms of Fourier basis [55, Appx. A2]. Since Wigner D-functions (also known as Wigner D-matrix) are identical, up to a normalization term, to spherical harmonics [79], the coefficients $\Delta^{\ell}_{m'm}$ used in [101] may be understood as being the elements of the equivalence matrix; see [Appx. A.2] for details. The work in [101] also leads to a fast spherical harmonic transform with a complexity of $\mathcal{O}(L^3)$. However, the method in [101] employs specific quadrature weights while the technique proposed in Table 4.1 is applicable regardless of the quadrature weights, including those in [101]. This is important since one may employ the 2-D FFT *without* compromising the statistical performance or optimality of the estimated spherical harmonic coefficients. Recall that the error covariance matrix of the estimators based on the DVSHT depend on the employed quadrature weights.

4.5 Array calibration example

A practical example illustrating the contributions in this chapter is now given by considering a typical array calibration task. Let $\boldsymbol{B}_{\theta}$ and $\boldsymbol{B}_{\phi}$ denote the calibration matrices of the 5-elements inverted-F antenna array (IFA), illustrated in Fig. 2.4-2. Assume that calibration measurements are taken using an equiangular grid. Consider that an estimate of the corresponding array sampling matrix is obtained from the acquired calibration matrices by a discrete vector spherical harmonic transform, and denote it by $\hat{\boldsymbol{G}}_{\mathrm{dvsht}}$. Similarly, let $\hat{\boldsymbol{\Phi}}_{\Xi}$ denote the constrained estimator of the 2-D Fourier spectrum of the 5-elements IFA.

Figure 4.7 illustrates the estimation results for $\hat{\boldsymbol{G}}_{\mathrm{dvsht}}$ and $\hat{\boldsymbol{\Phi}}_{\Xi}$, in terms of normalized power for three calibration measurement scenarios: 1) $Q = 35 \times 34$ calibration points with $\mathrm{SNR}_{\mathrm{cal}} = 20$dB; 2) $Q = 35 \times 34$ calibration points with $\mathrm{SNR}_{\mathrm{cal}} = 30$dB; and $Q = 61 \times 60$ calibration points with $\mathrm{SNR}_{\mathrm{cal}} = 30$dB. Figure 4.8 illustrates the corresponding MSEs for the

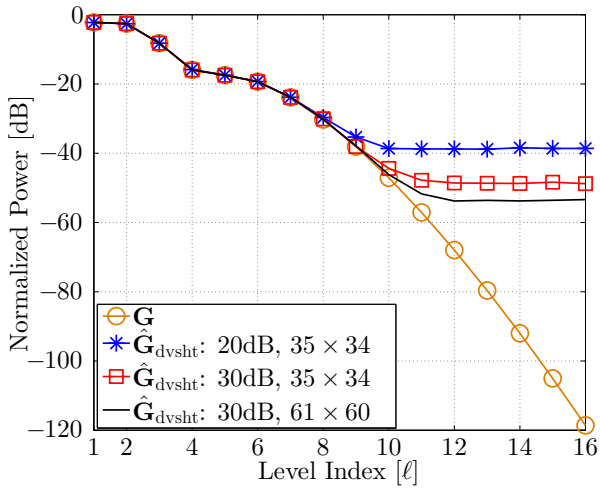

(a) Estimates of the array sampling matrix based on discrete vector spherical harmonic transform.

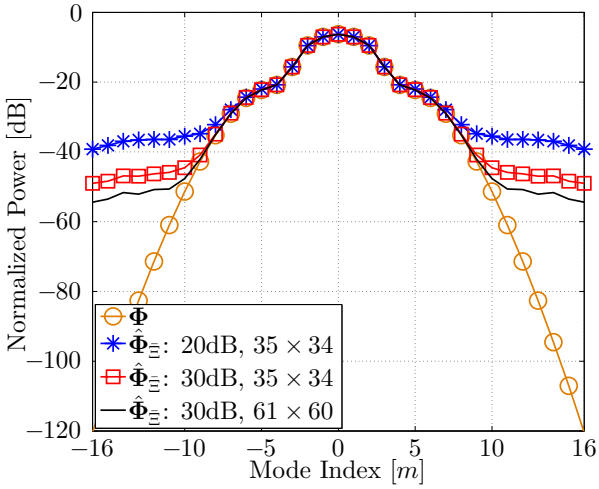

(b) Constrained estimates of the 2-D Fourier spectrum.

Figure 4.7. Illustration of estimates obtained by $\hat{G}_{\text{dvsht}}$ and $\hat{\Phi}_{\Xi}$, in terms of normalized power, for three calibration measurement scenarios. Coefficients for large levels/modes may be discarded since their power is negligible compared to the estimation variance.

third calibration measurement scenario, as a function of the number of columns employed by the estimators in order to reconstruct the array steering vector.

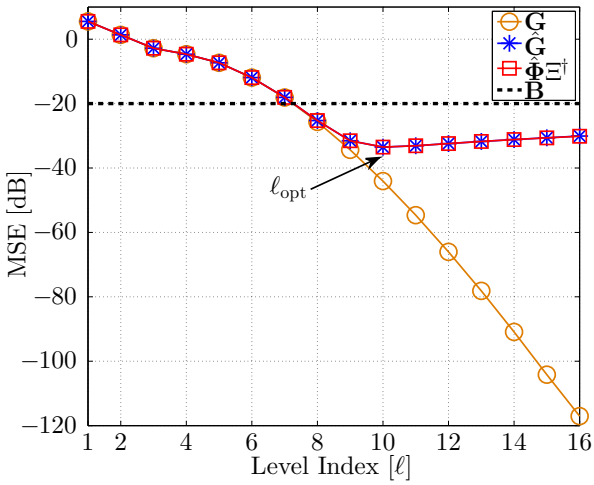

Figure 4.8. Illustration of the mean-squared-error obtained from the sampling matrix estimator based on DVSHT, constrained estimator of the 2-D Fourier spectrum, and array calibration matrix. The calibration measurement scenario is given by $Q = 61 \times 60$ calibration points with $\text{SNR}_{\text{cal}} = 30$dB. Truncating the sampling matrix at $\ell_{\text{opt}} = 10$ improves the MSE in comparison to the array calibration matrix by ~ 15dB. Employing manifold separation in array calibration measurements may be understood as denoising the calibration data.

The definitions of normalized power used in Fig. 4.7 are given by:

$$P(\ell) = \frac{1}{4\ell+2} \sum_{\xi=1}^{2\ell^2+4\ell} \left\| [\hat{\boldsymbol{G}}]_\xi \right\|^2, \tag{4.56}$$

$$P(m) = \frac{1}{2\sqrt{\mathcal{M}}} \sum_{\xi=1}^{\sqrt{\mathcal{M}}} \left\| [\hat{\boldsymbol{\Phi}}_\theta]_{m+M+(\xi-1)\sqrt{\mathcal{M}}} \right\|^2 + \left\| [\hat{\boldsymbol{\Phi}}_\phi]_{m+M+(\xi-1)\sqrt{\mathcal{M}}} \right\|^2, \tag{4.57}$$

where $M = (\sqrt{\mathcal{M}}+1)/2$. Also, mean-squared-error is defined as follows:

$$\text{MSE} = \frac{1}{4\pi}\mathbb{E}\Big\{ \int_{\mathcal{S}^2} \|\boldsymbol{a}_\theta(\vartheta,\varphi) - \hat{\boldsymbol{a}}_\theta(\vartheta,\varphi)\|^2 + \|\boldsymbol{a}_\phi(\vartheta,\varphi) - \hat{\boldsymbol{a}}_\phi(\vartheta,\varphi)\|^2 d\Omega \Big\}, \tag{4.58}$$

$$= \frac{1}{4\pi}\mathbb{E}\left\{ \sum_{\xi=1}^{+\infty} \|[\boldsymbol{G}]_\xi - [\hat{\boldsymbol{G}}]_\xi\|^2 \right\}, \tag{4.59}$$

where $\hat{\boldsymbol{a}}_\theta(\vartheta,\varphi) = \sum_{\xi=1}^{\mathcal{L}} [\hat{\boldsymbol{G}}]_\xi [\boldsymbol{y}_\theta(\vartheta,\varphi)]_\xi$, and similarly for $\hat{\boldsymbol{a}}_\phi(\vartheta,\varphi)$. Finally, calibration signal-to-noise-ratio, denoted by SNR_{cal}, is given by:

$$\text{SNR}_{\text{cal}} = \frac{\sigma_s^2}{N\sigma_{\text{cal}}^2} \frac{1}{4\pi} \int_{\mathcal{S}^2} \|\boldsymbol{a}_\theta(\vartheta,\varphi)\|^2 + \|\boldsymbol{a}_\phi(\vartheta,\varphi)\|^2 d\Omega \tag{4.60}$$

$$= \frac{\sigma_s^2}{N\sigma_{\text{cal}}^2} \frac{\|\boldsymbol{G}\|_F^2}{4\pi}. \tag{4.61}$$

Results show that the response of real-world antenna arrays, including their nonidealities, may be equally well described by a discrete vector

spherical harmonic transform of the calibration matrix or by projecting the 2-D EADF onto the row-space of the equivalence matrix. These estimators may outperform the array calibration matrix, in terms of MSE, by an appropriate selection of the columns of $\hat{\boldsymbol{G}}$ and $\hat{\boldsymbol{\Phi}}_{\Xi}$. Such a selection may be done in a rigorous manner and free of heuristic design-parameters by employing model order selection methods [22, 68, 126, 147]. The main theoretical contributions of this thesis work, namely the equivalence matrix and the superexponential decay of the sampling matrix for polarization sensitive antenna arrays, are thus shown to facilitate denoising of array calibration measurements as well as compressing the calibration data and modeling the steering vector of real-world arrays.

4.6 Discussion

Wavefield modeling and manifold separation are important results in many fields of engineering employing sensor arrays. The array output is decomposed into two independent parts: the coefficient vector depending on the wavefield only and the sampling matrix depending only on the sensor array, including nonideaities. Describing array nonidealities as well as the array geometry and directional beampatterns of the array elements in a nonparametric manner by the sampling matrix is convenient in array processing. Indeed, such an approach overcomes the challenging task of describing complex electromagnetic interactions among array elements in a closed-form. These results allow for employing high-resolution and optimal array processing methods in real-world arrays with nonidealities.

Array calibration measurements do not limit the practical relevance of wavefield modeling or manifold separation. The sampling matrix may also be estimated from the array output in multipath channels given that the spatial distribution of the wavefield is known. This is equivalent to know the coefficient vector used in wavefield modeling. Also, the rational behind auto-calibration methods may be employed for relaxing the requirement of a fully known coefficient vector when estimating the sampling matrix.

The superexponential decay of the sampling matrix is one of the most important properties in wavefield modeling and manifold separation. It is useful in a variety of tasks including array processing, calibration measurements, MIMO systems, and indoor positioning [8, 70, 71, 117]. The superexponential decay is a rigorous argument for considering that a few

columns of the sampling matrix describe most of the array characteristics including its nonidealities. Such a result also leads to denoising of calibration measurements and data compression. The physical interpretation of the superexponential decay is that of attenuating the coefficients of the wavefield corresponding to spatial harmonics for increasing orders. It may be understood as the well-known limit in resolution of sensor arrays imposed by their finite aperture.

The equivalence matrix is useful in many areas of engineering dealing with data on a spherical manifold. The ability to write vector spherical harmonics in terms of an exact and finite 2-D Fourier basis expansion as well as the one-to-one relationship among spherical harmonic spectra and 2-D Fourier spectra provides more insight into many of the well-known discrete spherical harmonic transforms. The equivalence matrix proves useful in array processing by enabling a reformulation of wavefield modeling and manifold separation in terms of 2-D Fourier basis. This is important since array processing methods may exploit the computational efficiency and widespread usage of the FFT regardless of the sensor array geometry. Moreover, a rigorous theoretical justification for using the 2-D EADF in any array processing task as well as for improving its estimation variance is obtained by employing the equivalence matrix as well. Other important results that follow from the equivalence matrix include a novel fast vector spherical harmonic transform and sampling theorems for exact reconstruction on the 2-sphere.

Sector-by-sector processing on the sphere is not considered in this thesis work. However, it is important to emphasize that wavefield modeling and manifold separation may also incorporate prior information regarding the location of the sources. The resulting sampling matrix can be shown to retain the superexponential decay property as well [28, 29, 29]. Note also that spherical harmonics may be used in sector-by-sector processing by using appropriate window functions [72]. Hence, the equivalence matrix may be employed in related fast transforms [73]. This is useful when calibration measurements may only be acquired on a limited angular sector, for example. Even though wavefield modeling and manifold separation as well as the equivalence matrix are by no means the only approach to sector-by-sector processing or multi-resolution on the sphere, the contributions of this chapter are certainly an attractive alternative to the methods in [14, 15, 40, 47, 64, 163, 176].

In the next chapter, wavefield modeling and manifold separation as well

as the equivalence matrix are employed in the context of computationally efficient signal processing methods for arbitrary array geometries and in the face of nonidealities.

5. Signal processing methods for arbitrary array geometries

High-resolution and optimal array processing methods are known to be sensitive to misspecification of the array response [46, 77, 163]. These may be due to mismodeling of array nonidealities, misplacement of array elements, and uncertainties on the location and polarization of the signal-of-interest (SOI). This chapter extends well-known array processing methods in order to taken into account array nonidealities such as mutual coupling, cross-polarization effects, and mounting platform reflections [I, II, VIII, III, VII]. The proposed methods are based on wavefield modeling, manifold separation, and equivalence matrix.

The array processing methods proposed in this chapter extend the conventional and Capon beamformers to azimuth, elevation and polarimetric domains. Similarly, subspace methods including multiple signal classification (MUSIC), root-MUSIC, and weighted subspace fitting (WSF) are extended to angle and polarization estimation using manifold separation. The proposed methods *do not* assume any specific array geometry. The employed antenna array may have a regular geometry or be composed of elements arranged on an arbitrary configuration. Also, the array elements need not be identical and each of them may have an individual directional beampattern. Note that the array steering vector, including nonidealities, need not be known in a closed-form in order to achieve high-resolution capability and optimal performance [II, VIII, III]. This is an important feature since cross-polarization effects and elements' directional beampatterns are extremely challenging to describe in a closed-form.

The equivalence matrix introduced in [V, VI] and in Chapter 4 allows one to improve the computational complexity of the array processing methods that are based on manifold separation. Many optimization tasks needed in array processing may exploit the fast Fourier transform and polynomial rooting based computational methods. This is achieved with-

out restricting the proposed methods to regular array geometries. For example, the computationally-efficient root-MUSIC method may be extended to conformal or volumetric arrays in the face of nonidealities [II, VIII, III].

This chapter also includes an expression for the widely-used stochastic CRB for the DoA and polarization estimation problem that is based on the equivalence matrix as well as manifold separation [VII]. Such an expression is particularly useful in assessing the performance achievable by real-world antenna arrays.

5.1 Beamforming techniques

Beamforming refers to combining signals received or transmitted by sensor arrays in order to separate radiating sources or users based on their spatial locations. It amounts at steering energy to or from desired directions and polarizations. Receive beamforming may be understood as a spatial filter aiming at enhancing a signal-of-interest (SOI) while attenuating interfering sources. Transmit beamforming aims at generating a propagating wavefield so that the transmitted signals are coherently combined only at the desired users. Receive and transmit beamforming exploit the degrees-of-freedom provided by the spatial and polarimetric domains in addition to temporal, waveform, and frequency diversity. Beamforming finds applications in radar and sonar, wireless communications and radio channel modeling, audio processing, radio astronomy, and many others [17, 80, 121, 160, 162]. This section considers receive polarimetric beamforming in the context of wavefield modeling and manifold separation. A survey on beamforming including many transmit schemes can be found in [48, 162].

Let $\boldsymbol{w}_p \in \mathbb{C}^{N\times 1}$ and $\boldsymbol{x}(k) \in \mathbb{C}^{N\times 1}$ denote a beamformer weight vector towards the pth source and the output of a polarization sensitive array, as described in Chapter 2, respectively. The transmitted signal $s_p(k) \in \mathbb{C}$ may be estimated as follows:

$$\hat{s}_p(k) = \boldsymbol{w}_p^H \boldsymbol{x}(k). \tag{5.1}$$

Note that employing polarization sensitive arrays allows one to separate co-located sources based on the polarization state of the transmitted Electric-fields.

The polarimetric spatial spectrum $P(\vartheta, \varphi, \gamma, \beta) \in \mathbb{R}$ describes the distri-

bution of power around the antenna array in the 3-D Euclidean space in terms of elevation and azimuth angles as well as polarization. The polarimetric spatial spectrum may be used for direction-finding purposes and to estimate the angle and polarization of the sources needed in many receive and transmit beamformers. An estimate of the polarimetric spatial spectrum may be obtained from the beamformer weight vector as follows:

$$\hat{P}(\vartheta, \varphi, \gamma, \beta) = \boldsymbol{w}^H(\vartheta, \varphi, \gamma, \beta)\, \hat{\boldsymbol{R}}_x\, \boldsymbol{w}(\vartheta, \varphi, \gamma, \beta), \tag{5.2}$$

where $\hat{\boldsymbol{R}}_x \in \mathbb{C}^{N \times N}$ denotes the array covariance matrix estimate, described in Chapter 2.

Beamformers may be classified either as *data-independent* or *statistically optimum* methods [162]. A common optimality criterion for beamformers is given by the array output SINR [46, 162]:

$$\mathrm{SINR}_{\mathrm{out}} = \frac{\sigma^2_{\mathrm{soi}} |\boldsymbol{w}^H \boldsymbol{a}_{\mathrm{soi}}|^2}{\boldsymbol{w}^H \boldsymbol{R}_{i+n} \boldsymbol{w}}, \tag{5.3}$$

where $\boldsymbol{a}_{\mathrm{soi}} \in \mathbb{C}^{N \times 1}$ and $\sigma^2_{\mathrm{soi}} \in \mathbb{R}$ denote the steering vector due to the SOI and corresponding received power, respectively. Moreover, $\boldsymbol{R}_{i+n} \in \mathbb{C}^{N \times N}$ denote the "interference-plus-noise" covariance matrix. Two widely used beamformers are considered next in the context of wavefield modeling and manifold separation, namely the conventional beamformer and the Capon beamformer.

5.1.1 Conventional beamformer

The conventional beamformer, also known as Bartlett beamformer, is arguably the simplest and most well-known beamforming method. It is a data-independent beamformer and may be understood as a spatial (and polarimetric) matched-filter aiming at equalizing the antenna gains as well as coherently combining the output of an antenna array [80, 162]. The weight vector of the conventional beamformer, in the context of wavefield modeling and manifold separation, matched to the angle (ϑ_p, φ_p) and polarization (γ_p, β_p) is [80, 160], [VII]:

$$\boldsymbol{w}_{\mathrm{bf}}(\vartheta_p, \varphi_p, \gamma_p, \beta_p) = \frac{\boldsymbol{\Phi}(\boldsymbol{I}_2 \otimes \boldsymbol{d}(\vartheta_p, \varphi_p))\boldsymbol{v}(\gamma_p, \beta_p)}{\sqrt{\boldsymbol{v}^H(\gamma_p, \beta_p)\boldsymbol{N}(\vartheta_p, \varphi_p)\boldsymbol{v}(\gamma_p, \beta_p)}}, \tag{5.4}$$

where matrix $\boldsymbol{N}(\vartheta, \varphi) \in \mathbb{C}^{2 \times 2}$ is given by:

$$\boldsymbol{N}(\vartheta, \varphi) = (\boldsymbol{I}_2 \otimes \boldsymbol{d}^H(\vartheta, \varphi))\boldsymbol{\Phi}^H \boldsymbol{\Phi}(\boldsymbol{I}_2 \otimes \boldsymbol{d}(\vartheta, \varphi)). \tag{5.5}$$

Note that matrix $\boldsymbol{N}(\vartheta, \varphi)$ is positive-definite given that the polarization sensitive array is unambiguous in the sense defined in Chapter 2.

The polarimetric spatial spectrum estimated by the conventional beamformer is:

$$\hat{P}_{\mathrm{bf}}(\vartheta,\varphi,\gamma,\beta)=\frac{\boldsymbol{v}^H(\gamma,\beta)\boldsymbol{M}_{\mathrm{bf}}(\vartheta,\varphi)\boldsymbol{v}(\gamma,\beta)}{\boldsymbol{v}^H(\gamma,\beta)\boldsymbol{N}(\vartheta,\varphi)\boldsymbol{v}(\gamma,\beta)}, \tag{5.6}$$

where matrix $\boldsymbol{M}_{\mathrm{bf}}(\vartheta,\varphi)\in\mathbb{C}^{2\times 2}$ is given by:

$$\boldsymbol{M}_{\mathrm{bf}}(\vartheta,\varphi)=(\boldsymbol{I}_2\otimes\boldsymbol{d}^H(\vartheta,\varphi))\boldsymbol{\Phi}^H\hat{\boldsymbol{R}}_x\boldsymbol{\Phi}(\boldsymbol{I}_2\otimes\boldsymbol{d}(\vartheta,\varphi)). \tag{5.7}$$

Expression (5.6) is a generalized Rayleigh quotient, and may thus be efficiently optimized by maximizing the largest eigenvalue $\mu_{\max}(\vartheta,\varphi)\in\mathbb{R}$ of the matrix pencil $(\boldsymbol{M}_{\mathrm{bf}}(\vartheta,\varphi),\boldsymbol{N}(\vartheta,\varphi))$ with respect to (ϑ,φ), as well as finding the corresponding eigenvector $\boldsymbol{u}_{\max}(\gamma,\beta)\in\mathbb{C}^{2\times 1}$. Such a matrix pencil involves (2×2) matrices, and therefore its eigenvalues/eigenvectors may be found in a closed-form by solving the corresponding characteristic polynomial of 2nd degree [151]. Moreover, maximizing the largest eigenvalue $\mu_{\max}(\vartheta,\varphi)$ may be efficiently implemented by an FFT-based 2-D line search in *both* azimuth and elevation angles [VII].

Assuming that a single source impinges on the sensor array, in the presence of spatially white measurement noise, the conventional beamformer maximizes the array output SINR in (5.3) [80], [49, Ch. 2]. Therefore, the conventional beamformer is the deterministic maximum likelihood estimator of the angle (ϑ_p,φ_p) and polarization (γ_p,β_p) for a single source [145, 146, 148]. However, the resolution of the conventional beamformer is limited by the array aperture and does not improve with increasing snapshots [80, 162]. Hence, it does not converge to the spatial spectrum of the wavefield for a fixed array aperture. This is an important limitation in applications employing array apertures in the order of one wavelength.

5.1.2 Capon beamformer

The Capon beamformer, also known as minimum variance distortionless response (MVDR) beamformer, is one of the most well-known optimum beamformers [16, 48, 80, 92, 162], [49, Ch. 2], [143, Ch. 6]. It aims at minimizing the array output power under a unit-gain constraint towards the direction and polarization of the SOI. The weight vector of the Capon beamformer, in the context of wavefield modeling and manifold separation, towards the angle (ϑ_p,φ_p) and polarization (γ_p,β_p) is [21, 46, 80, 162], [VII]:

$$\boldsymbol{w}_{\mathrm{capon}}=\frac{\hat{\boldsymbol{R}}_x^{-1}\boldsymbol{\Phi}(\boldsymbol{I}_2\otimes\boldsymbol{d}(\vartheta_p,\varphi_p))\boldsymbol{v}(\gamma_p,\beta_p)}{\boldsymbol{v}^H(\gamma_p,\beta_p)\boldsymbol{M}_{\mathrm{capon}}(\vartheta_p,\varphi_p)\boldsymbol{v}(\gamma_p,\beta_p)}, \tag{5.8}$$

where matrix $\boldsymbol{M}_{\text{capon}}(\vartheta,\varphi) \in \mathbb{C}^{2\times 2}$ is given by:

$$\boldsymbol{M}_{\text{capon}}(\vartheta,\varphi) = (\boldsymbol{I}_2 \otimes \boldsymbol{d}^H(\vartheta,\varphi))\boldsymbol{\Phi}^H \hat{\boldsymbol{R}}_x^{-1} \boldsymbol{\Phi}(\boldsymbol{I}_2 \otimes \boldsymbol{d}(\vartheta,\varphi)). \tag{5.9}$$

The polarimetric spatial spectrum estimated by the Capon beamformer is [21, 46, 80, 162], [VII]:

$$\hat{P}_{\text{capon}}(\vartheta,\varphi,\gamma,\beta) = \frac{1}{\boldsymbol{v}^H(\gamma,\beta)\boldsymbol{M}_{\text{capon}}(\vartheta,\varphi)\boldsymbol{v}(\gamma,\beta)}, \tag{5.10}$$

and its optimization typically requires an exhaustive 4-D search. However, a high-SINR approximation of (5.10) may be optimized efficiently in a similar manner to that in (5.6) [21]. Such a result is a good approximation even at low and moderate SINRs. In particular, angle and polarization estimates may be found by minimizing the determinant of $\boldsymbol{M}_{\text{capon}}(\vartheta,\varphi)$, and finding the eigenvector $\boldsymbol{u}_{\min}(\gamma,\beta) \in \mathbb{C}^{2\times 1}$ corresponding to the smallest eigenvalue of $\boldsymbol{M}_{\text{capon}}(\vartheta,\varphi)$ [21]. Since $\boldsymbol{M}_{\text{capon}}(\vartheta,\varphi)$ is a (2×2) matrix its eigenvalues and eigenvectors may be found in a closed-form. Moreover, minimizing the determinant of $\boldsymbol{M}_{\text{capon}}(\vartheta,\varphi)$ with respect to (ϑ,φ) may be efficiently implemented by an FFT-based 2-D line search in *both* azimuth and elevation angles [21].

The Capon beamformer maximizes the array output SINR in (5.3) given that *both* array covariance matrix and array steering vector are fully known [48, 162], [49, Ch. 2]. Indeed, for a scenario where a single source impinges the antenna array in spatially white Gaussian noise, the following relationship can be found $\boldsymbol{w}_{\text{capon}} \propto \boldsymbol{w}_{\text{bf}}$ [46]. However, in scenarios comprised of spatially interfering fields, the Capon beamformer typically outperforms the conventional beamformer in terms of resolution as well as in array output SINR. Even though the resolution of the spatial spectrum in (5.10) is limited by the array aperture, its resolution improves for increasing snapshots *and* SINR [21, 106], [160, Ch. 9]. Figure 5.1 illustrates the polarimetric spatial power spectra of the conventional and Capon beamformers.

The performance of the Capon beamformer degrades significantly when the array sample covariance matrix is ill-conditioned [18, 46, 92]. This may be the case when the number of acquired snapshots is not sufficient for building the rank of $\hat{\boldsymbol{R}}_x$. In such cases a *regularized* sample covariance matrix, denoted by $\tilde{\boldsymbol{R}}_x$, is typically used in (5.8) and (5.10) in place of $\hat{\boldsymbol{R}}_x$. In the context of array processing and Capon beamformer, a widely used regularization method, known as *diagonal loading*, is given as follows [18, 23, 46, 48]:

$$\tilde{\boldsymbol{R}}_x = \hat{\boldsymbol{R}}_x + \lambda \boldsymbol{I}_N, \tag{5.11}$$

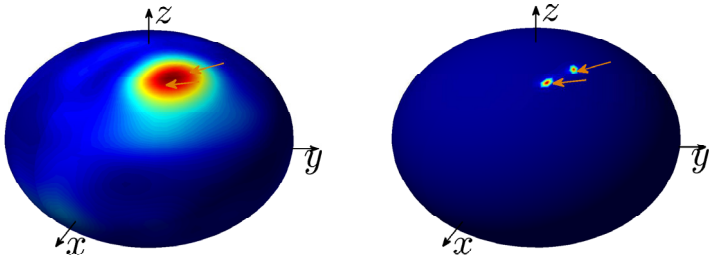

(a) Conventional beamformer. **(b)** Capon beamformer.

Figure 5.1. Polarimetric spatial power spectra of conventional beamformer and Capon beamformer. Two uncorrelated point-sources, with an $\mathrm{SNR} = 20dB$, are assumed to impinge on the PSSPA depicted in Fig. 2.4-1 from $\boldsymbol{\vartheta} = [30°, 25°]^T$ and $\boldsymbol{\varphi} = [60°, 90°]^T$. The polarization parameters of the sources are $\boldsymbol{\gamma} = [10°, 50°]^T$ and $\boldsymbol{\beta} = [0°, 30°]^T$. The Capon beamformer outperforms the conventional beamformer in terms of resolution since the Capon beampattern is close to the ideal Dirac-delta.

where $\lambda \in \mathbb{R}^+$ is called loading factor. Diagonal loading may be understood as artificially increasing the noise power. Such an approach improves the condition number of the array sample covariance matrix, and thus the resulting Capon beampattern, at the cost of making the Capon beamformer less sensitive to weak interferences [18]. Typically, diagonal loading also increases the width mainlobe of the resulting beampattern. The loading factor in (5.11) is typically a user-design parameter but some regularization techniques that find a suitable λ in a manner that is free of design-parameters can be found in [33, 34].

The Capon beamformer is also sensitive to misspecification of the array steering vectors [46, 48, 92]. This may be due to array nonidealities that are not considered by the steering vector model or inaccurate DoA and polarization estimates of the SOI. Measurement noise in array calibration may also deteriorate significantly the performance of the Capon beamformer in terms of array output SINR [21], [VIII]. Employing robust methods based on uncertainty sets, as described in Chapter (3), in the context of wavefield modeling and manifold separation allows for making the Capon beamformer robust to the aforementioned uncertainties [21,48,93,98,168], [VIII]. In particular, the denoising of array calibration measurements obtained by exploiting manifold separation typically leads to increased array output SINR of robust Capon beamformers. It is important to note that robust Capon beamformers based on uncertainty sets or worst-case performance optimization may be understood as finding the optimal loading factor in (5.11) given a tolerable uncertainty between

the actual and presumed steering vectors [48, 93, 98, 168].

5.2 Subspace methods

Subspace methods exploit the eigenstructure of the array covariance matrix and its sample estimate in estimating wavefield parameters [80], [160, Ch. 9]; see also Chapter 2. In particular, the DoAs and polarization of the sources impinging on a sensor array may be estimated from the eigenvectors and eigenvalues of the array sample covariance matrix. Typically, subspace methods outperform beamforming techniques in terms of resolution and estimation variance [80]. Unlike beamforming techniques, the resolution of subspace methods improves with increasing number of snapshots. Moreover, subspace methods are computationally more attractive that optimal maximum likelihood approaches [110]. Even thought maximum likelihood approaches outperform most subspace methods in terms of estimation variance, especially in highly-correlated scenarios, asymptotically statistically efficient subspace methods can also be found in the literature [148, 164].

Subspace methods typically rely on a low-rank model for the array output. In particular, given that the number of array elements N and radiating point-sources P satisfies $P < N$, the *exact* array covariance matrix may be written as follows (see also Chapter 2) [80]:

$$\boldsymbol{R}_x = \boldsymbol{U}_s \boldsymbol{\Lambda}_s \boldsymbol{U}_s^H + \boldsymbol{U}_n \boldsymbol{\Lambda}_n \boldsymbol{U}_n^H, \tag{5.12}$$

where $\boldsymbol{U}_s \in \mathbb{C}^{N \times P'}$ and $\boldsymbol{U}_n \in \mathbb{C}^{N \times (N-P')}$ contain the eigenvectors of $\boldsymbol{R}_x$ spanning the signal and noise subspaces while $\boldsymbol{\Lambda}_s \in \mathbb{R}^{P' \times P'}$ and $\boldsymbol{\Lambda}_n \in \mathbb{R}^{(N-P') \times (N-P')}$ contain the corresponding eigenvalues on their diagonal. Subspace methods are based on the result that the columns of $\boldsymbol{U}_s$ span the same subspace as the columns of $\boldsymbol{A}(\boldsymbol{\xi})$ (in the case of coherent signals $\boldsymbol{U}_s$ is contained in the subspace spanned by the columns of $\boldsymbol{A}(\boldsymbol{\xi})$), and that both $\boldsymbol{U}_s$ and $\boldsymbol{A}(\boldsymbol{\xi})$ are orthogonal to $\boldsymbol{U}_n$. In the more practical case when a sample estimate of the array covariance matrix is obtained, subspace methods employ the corresponding estimates of the eigenvectors $\hat{\boldsymbol{U}}_s, \hat{\boldsymbol{U}}_n$ and eigenvalues $\hat{\boldsymbol{\Lambda}}_s, \hat{\boldsymbol{\Lambda}}_s$; see also Chapter 2.

The low-rank model in (5.12) is applicable when both point-source and narrowband assumptions hold true. Subspace methods are thus parametric techniques, similarly to spectral estimation, unlike nonparametric beamforming methods [143]. The impact of spatially distributed sources

on subspace methods as well as the effects due to increasing bandwidth of the signals can be found in [10, 141]. Subspace methods may also be sensitive to modeling errors of the array steering vector [163]. This may be due to array nonidealities that are challenging to represent in a closed-form or calibration measurement noise. Such modeling errors typically result in parameter estimates with large bias and excess variance [7, 37, 38, 88, 153, 154, 166].

In this section, two well-known subspace methods are considered in the context of wavefield modeling and manifold separation, namely the MUSIC and weighted subspace fitting (WSF) methods. The usefulness of wavefield modeling and manifold separation is twofold. Firstly, it is a convenient way of taking into account array nonidealities such as mutual coupling, cross-polarization effects, and individual directional beampatterns into subspace based array processing methods. Secondly, computationally-efficient solutions for finding the DoAs and polarization of the sources may be found, similarly to the case with ULAs.

5.2.1 Multiple signal classification (MUSIC)

The MUltiple SIgnal Classification (MUSIC) method is perhaps the most widely-used and well-known subspace method in array processing [58, 80, 129, 136, 144, 180], [160, Ch. 9]. Indeed, most of the research efforts in subspace based array processing methods follow the seminal work in [136] as well as Pisarenko's method in [116]. The MUSIC method measures the squared-length of the steering vectors projected onto the noise subspace of the array sample covariance matrix. In particular, the MUSIC expression, in the context of wavefield modeling and manifold separation, is given by [36, 136, 173], [III, VII]:

$$f_{\text{music}}(\vartheta, \varphi, \gamma, \beta) = \frac{1}{\boldsymbol{v}^H(\gamma, \beta)\boldsymbol{M}_{\text{music}}(\vartheta, \varphi)\boldsymbol{v}(\gamma, \beta)}, \tag{5.13}$$

where matrix $\boldsymbol{M}_{\text{music}}(\vartheta, \varphi) \in \mathbb{C}^{2\times 2}$ is given by:

$$\boldsymbol{M}_{\text{music}}(\vartheta, \varphi) = (\boldsymbol{I}_2 \otimes \boldsymbol{d}^H(\vartheta, \varphi))\boldsymbol{\Phi}^H\hat{\boldsymbol{U}}_n\hat{\boldsymbol{U}}_n^H\boldsymbol{\Phi}(\boldsymbol{I}_2 \otimes \boldsymbol{d}(\vartheta, \varphi)). \tag{5.14}$$

Expression (5.13) is known as *pseudo-spectrum* since it is an index of orthogonality between a steering vector $\boldsymbol{a}(\boldsymbol{\xi})$ and the whole noise subspace $\hat{\boldsymbol{U}}_n$, rather than a power-spectrum.

The MUSIC estimates of DoA and polarization may be found efficiently by minimizing the determinant of $\boldsymbol{M}_{\text{music}}(\vartheta, \varphi)$, and finding the eigenvector $\boldsymbol{u}_{\min}(\gamma, \beta) \in \mathbb{C}^{2\times 1}$ corresponding to the smallest eigenvalue of (5.14)

[36,115,173], [III, VII]. Such an approach may be understood as an asymptotic approximation to minimizing the smallest eigenvalue of $\boldsymbol{M}_{\text{music}}(\vartheta,\varphi)$. Typically, optimizing the determinant of an Hermitian matrix is more convenient than minimizing the smallest eigenvalue.

In particular, the determinant of $\boldsymbol{M}_{\text{music}}(\vartheta,\varphi)$ may be written as follows [III, VII]:

$$\det\{\boldsymbol{M}_{\text{music}}(\vartheta,\varphi)\} = \bar{\boldsymbol{d}}^H(\varphi)\boldsymbol{C}\bar{\boldsymbol{d}}(\vartheta), \tag{5.15}$$

where $\bar{\boldsymbol{d}}(\vartheta) \in \mathbb{C}^{(4\sqrt{\mathcal{M}}-3)\times 1}$ and $\bar{\boldsymbol{d}}(\varphi) \in \mathbb{C}^{(4\sqrt{\mathcal{M}}-3)\times 1}$ denote Vandermonde structured vectors composed of 1-D Fourier basis. Moreover, the coefficients matrix $\boldsymbol{C} \in \mathbb{C}^{(4\sqrt{\mathcal{M}}-3)\times(4\sqrt{\mathcal{M}}-3)}$ can be found in a computationally-efficient manner as follows [VII, III]:

$$\boldsymbol{C} = \text{FFT2}\Bigg\{ \Big(\sum_{i=1}^{N-P} \Big|\text{IFFT2}\{\boldsymbol{C}_i^{\phi}\}\Big|^2 \Big) \odot \Big(\sum_{i=1}^{N-P} \Big|\text{IFFT2}\{\boldsymbol{C}_i^{\theta}\}\Big|^2 \Big) - \Big| \sum_{i=1}^{N-P} \text{IFFT2}\{\boldsymbol{C}_i^{\phi}\} \odot \text{IFFT2}\{\tilde{\boldsymbol{I}}\boldsymbol{C}_i^{\theta^c}\tilde{\boldsymbol{I}}\} \Big|^2 \Bigg\}, \tag{5.16}$$

where $\boldsymbol{C}_i^{\phi} = \text{ivec}\{[\hat{\boldsymbol{U}}_n]_i^H \boldsymbol{G}_{\phi}\} \in \mathbb{C}^{\sqrt{\mathcal{M}}\times\sqrt{\mathcal{M}}}$ and similarly for $\boldsymbol{C}_i^{\theta} \in \mathbb{C}^{\sqrt{\mathcal{M}}\times\sqrt{\mathcal{M}}}$. Note that each FFT2/IFFT2 operation in (5.16) should be taken using at least $(4\sqrt{\mathcal{M}}-3)\times(4\sqrt{\mathcal{M}}-3)$ points, and by zero-padding in order to avoid aliasing. Expression (5.15) may be minimized in an efficient manner using an FFT-based line search. The complexity of such an approach is $\mathcal{O}(Q\log Q)$ given that $Q >> \mathcal{M}$ and Q is a power of 2 [VII].

Expressions (5.15) and (5.16) may also be useful in optimizing the Capon spatial spectrum (5.6). In particular, using the square-root factor of the array sample covariance matrix in place of $\hat{\boldsymbol{U}}_n$ in (5.15) and (5.16) results on a high SINR approximation to minimizing the smallest eigenvalue of $\boldsymbol{M}_{\text{capon}}(\vartheta,\varphi)$ [21]. This may be understood by noting that the MUSIC pseudo-spectrum and Capon spatial spectrum are related as follows [21]:

$$P_{\text{capon}}(\vartheta,\varphi,\gamma,\beta) \to \frac{1}{\sigma_{i+n}^2} f_{\text{music}}(\vartheta,\varphi,\gamma,\beta), \quad \text{when} \quad \text{SINR} \to +\infty, \tag{5.17}$$

where the σ_{i+n}^2 is assumed fixed.

Once the angle estimates $(\hat{\boldsymbol{\vartheta}},\hat{\boldsymbol{\varphi}})$ of the P sources are found, the polarization parameters may be estimated as follows [173], [III, VII]:

$$\hat{\gamma}_p = \arccos\{[\boldsymbol{v}_p]_1\} \quad \hat{\beta}_p = \angle[\boldsymbol{v}_p]_2, \quad p = 1,\ldots,P, \tag{5.18}$$

where $\boldsymbol{v}_p = \boldsymbol{u}_p \frac{[\boldsymbol{u}_p^c]_1}{|[\boldsymbol{u}_p]_1|}$, and $\boldsymbol{u}_p \in \mathbb{C}^{2\times 1}$ denotes the eigenvector corresponding to the smallest eigenvalue of $\boldsymbol{M}_{\text{music}}([\hat{\boldsymbol{\vartheta}}]_p,[\hat{\boldsymbol{\varphi}}]_p)$. Note that the above normalization of vector $\boldsymbol{v}_p$ ensures that $\hat{\gamma}_p \in \mathbb{R}$ [173]. It is also important

to emphasize that the eigenvector $\boldsymbol{u}_p$ may be found in a computationally-efficient manner using either Rayleigh quotient iterations or Lanczos method [50]. In fact, the eigenvalues and eigenvectors of (2×2) matrices, such as those of $\boldsymbol{M}_{\text{music}}(\vartheta, \varphi)$, may be found in a closed-form.

5.2.2 Root-MUSIC

Root-MUSIC is a method for finding the P maxima of the MUSIC pseudo-spectrum that is based on polynomial rooting [6]. Root-MUSIC is known to have higher resolution than the spectral MUSIC [124]. However, it typically requires regular array geometries such as uniform linear arrays. In the following, manifold separation is employed for finding the P maxima of the *polarimetric* MUSIC pseudo-spectrum in (5.13) by polynomial rooting. It is assumed that the co-elevation angles of the sources are known. Conversely, the azimuth-angles of the sources may be held fixed and the co-elevation angles found by polynomial rooting. When both co-elevation and azimuth angles are unknown one could employ the above procedure in an alternating fashion. However, such an approach may require solving of a large number of polynomials.

The root-MUSIC proposed in this thesis is applicable for antenna arrays of arbitrary geometries, including nonidealities. It may be understood as an extension of the element-space root-MUSIC [9] for polarimetric arrays, and co-elevation angles. Using manifold separation overcomes the requirement of uniform circular arrays in beamspace root-MUSIC and sector-by-sector processing in interpolated root-MUSIC methods [7, 100, 173].

In particular, the P minima of $\det\{\boldsymbol{M}_{\text{music}}(\vartheta_0, \varphi)\}$ in (5.15), for a *fixed* co-elevation angle ϑ_0, may be found from the roots of the following polynomial:

$$p(z) = c_{2\sqrt{\mathcal{M}}-2} z^{2\sqrt{\mathcal{M}}-2}, \ldots, c_1\, z,\, c_0,\, c_{-1}\, z^{-1}, \ldots, c_{-(2\sqrt{\mathcal{M}}-2)} z^{-(2\sqrt{\mathcal{M}}-2)}, \tag{5.19}$$

where $\{c_m \in \mathbb{C}\}_{m=2\sqrt{\mathcal{M}}-2}^{-(2\sqrt{\mathcal{M}}-2)}$ are the elements of vector $\boldsymbol{c} = \boldsymbol{C}\bar{\boldsymbol{d}}(\vartheta_0)$. Alternatively, the P minima of $\det\{\boldsymbol{M}_{\text{music}}(\vartheta, \varphi_0)\}$, for a fixed azimuth-angle φ_0, may be found from the roots of a polynomial similar to (5.19) with coefficients taken from $\boldsymbol{c}^H = \bar{\boldsymbol{d}}^H(\varphi_0)\boldsymbol{C}$.

The polynomial $p(z)$ in (5.19) is a Laurent polynomial since its coefficients have the following property $\{c_m = c_{-m}^*\}_{m=0}^{2\sqrt{\mathcal{M}}-2}$ [135]. This may be understood by noting that $\boldsymbol{M}_{\text{music}}(\vartheta, \varphi)$ in (5.13) is an Hermitian matrix,

and the MUSIC pseudo-spectrum is real-valued. Indeed, Laurent polynomials such as $p(z)$ have a number of useful properties [135]. In particular, the roots of $p(z)$ are so-called conjugate-reciprocal in the sense that if $z_0 \in \mathbb{C}$ is a zero of $p(z)$ then $1/z_0^*$ also vanishes $p(z)$. Furthermore, if $\det\{\boldsymbol{M}_{\text{music}}(\vartheta_0, \varphi)\} > 0$, $\forall \varphi$ then $p(z)$ has $(2\sqrt{\mathcal{M}} - 2)$ zeros strictly inside the unit circle $(0 < |z| < 1)$, and similarly $(2\sqrt{\mathcal{M}} - 2)$ roots strictly outside the unit circle.

One may thus proceed in a manner similar to the root-MUSIC for ULAs, and estimate the DoAs from the phase-angles of the P roots closest to the unit circle by discarding the $(2\sqrt{\mathcal{M}} - 2)$ zeros that lie strictly outside the unit circle, for example. However, such an approach may be inefficient since it requires finding *all* of the $(4\sqrt{\mathcal{M}} - 4)$ roots of (5.19)[1]. Typically, roots of polynomials are found from the eigenvalues of the associated companion matrix, and such an approach is $\mathcal{O}(n^2)$ [11, 112].

A more computationally-efficient method for finding the P roots closest to the unit-circle consists in factorizing $p(z)$ in (5.19) in terms of two polynomials, each of them containing the roots inside and outside the unit-circle separately [135, 181]. The P roots associated with the sources may then be found from the "extreme eigenvalues" (largest or smallest magnitude) of the associated companion matrix by means of Arnoldi iteration [50, Ch.9], [181]. Another approach for finding the P minima of $\det\{\boldsymbol{M}_{\text{music}}(\vartheta_0, \varphi)\}$ consists in determining the roots of a real-valued polynomial [21], [VIII]. Such a method is particularly useful in nonstationary environments since computationally efficient root tracking techniques for real-valued polynomials can be found in [152], for example. Note that the above observations are also applicable in finding the P minima of the Capon spatial-spectrum in (5.10) [21], [VIII].

A comment regarding the Fourier-domain (FD) root-MUSIC is now in place [129]. Such a method expresses the MUSIC null-spectrum in terms of a polynomial in φ, similarly to (5.19). The FD root-MUSIC finds the polynomial coefficients by sampling the MUSIC null-spectrum followed by a discrete Fourier transform. Such an approach of obtaining the polynomial coefficients may outperform the method based on manifold separation in (5.16) in terms of average-squared error. This may be understood by noting that the polynomial coefficients of the MUSIC null-spectrum may be obtained from an auto-correlation of the array sampling

[1]As an example, for a polarimetric array with an aperture of one wavelength it may be required to find 28 roots

matrix [29]. Since the auto-correlation of the sampling matrix involves all of the columns of $\boldsymbol{G}$, a larger modeling error results from truncating $\boldsymbol{G}$ prior to the auto-correlation operation, as it is done in manifold separation.

However, the approach followed by the FD root-MUSIC has two limitations with respect to using manifold separation. Firstly, the pseudo-spectrum of the FD root-MUSIC is not strictly positive and may take negative values [129]. Consequently, one may not employ the polynomial factorization described in [135, 181], and the FD root-MUSIC may still require finding all of the $(4\sqrt{\mathcal{M}}-4)$ roots in order to estimate the DoAs. Secondly, when the array response is acquired from calibration measurements, the polynomial coefficients obtained by using manifold separation typically have a lower MSE than those found by the FD root-MUSIC. This follows from the observation that the auto-correlation of a zero-mean white complex Gaussian vector of dimension Q is Chi-squared distributed with $2Q$ degrees-of-freedom, at the zero-lag. Therefore, truncating the sampling matrix prior to the auto-correlation operation, as in manifold separation, decreases the estimation variance of the polynomial coefficients since such a truncation reduces the degrees-of-freedom of the so-obtained Chi-squared distributed coefficients.

5.2.3 Weighted subspace fitting (WSF)

Subspace fitting is a unified framework for parameter estimation in array processing [10, 66, 110, 148, 149, 164]. Most of array processing methods found in the literature may be seen as special cases of the more general subspace fitting expression, including the deterministic maximum-likelihood estimator and the MUSIC method. Weighted subspace fitting (WSF) is obtained by employing an appropriate positive-definite weighting matrix on the subspace fitting criterion. The resulting parameter estimates attain the stochastic CRB asymptotically under the assumption of complex Gaussian noise [109]. The asymptotically statistically efficient method of direction estimation (MODE) [148, 149] may also be seen as a weighted subspace fitting approach [110]. The MODE method is based on the noise subspace of the array sample covariance matrix while the WSF exploits the corresponding signal subspace. The latter is thus appropriate for scenarios where fully correlated sources may be present.

The WSF criterion in the context of wavefield modeling and manifold separation is obtained in a straightforward manner from the results in

[164, 165], and it is given by [III, VII]:

$$\hat{\boldsymbol{\xi}} = \arg\min_{\boldsymbol{\xi}} \operatorname{tr}\left\{ \boldsymbol{P}_{\Phi}^{\perp}(\boldsymbol{\xi}) \hat{\boldsymbol{U}}_s \boldsymbol{W} \hat{\boldsymbol{U}}_s^H \right\}, \tag{5.20}$$

where $\boldsymbol{P}_{\Phi}^{\perp}(\boldsymbol{\xi}) \in \mathbb{C}^{N \times N}$ and $\boldsymbol{P}_{\Phi}(\boldsymbol{\xi}) \in \mathbb{C}^{N \times N}$ denote projection matrices. They are given by $\boldsymbol{P}_{\Phi}^{\perp}(\boldsymbol{\xi}) = \boldsymbol{I}_N - \boldsymbol{P}_{\Phi}(\boldsymbol{\xi})$ and

$$\boldsymbol{P}_{\Phi}(\boldsymbol{\xi}) = \boldsymbol{\Phi}(\boldsymbol{I}_2 \otimes \boldsymbol{D}(\vartheta, \boldsymbol{\varphi}))\boldsymbol{V}(\boldsymbol{\gamma}, \boldsymbol{\beta}) \left(\boldsymbol{\Phi}(\boldsymbol{I}_2 \otimes \boldsymbol{D}(\vartheta, \boldsymbol{\varphi}))\boldsymbol{V}(\boldsymbol{\gamma}, \boldsymbol{\beta})\right)^{\dagger}, \tag{5.21}$$

respectively. The weighting matrix $\boldsymbol{W} \in \mathbb{R}^{P' \times P'}$ ensures asymptotically statistically efficient parameter estimates under complex Gaussian noise, and can be found in [164, 165].

Expression (5.20) is convenient since the parameterization of $\boldsymbol{\xi}$ is fixed regardless of the geometry of the antenna array and nonidealities. Moreover, closed-form expressions for the gradient and Hessian of (5.20) can be found in a straightforward manner [VII]. Such expressions are typically needed in optimizing expression (5.20) [165].

5.3 Stochastic CRB for real-world antenna arrays

The Cramér-Rao bound (CRB) is a lower bound on the estimation error variance of any unbiased estimator [69]. In array processing, the stochastic (or unconditional) CRB is a well-known and widely used benchmark for assessing the performance of array processing methods, especially in the high SNR regime [109, 142, 146]. Conversely, it facilitates the practitioner to decide whether a given antenna array is appropriate for the parameter estimation task under consideration. Manifold separation is a convenient approach for finding an approximate but tight CRB expression for real-world antenna arrays, including nonidealities. In particular, the stochastic CRB is given by [109, 142], [VII]:

$$\begin{aligned} \mathbf{CRB}(\boldsymbol{\xi}) = \frac{\sigma_n^2}{2K} \Re\Big\{ &(\dot{\boldsymbol{\mathcal{D}}}^H(\boldsymbol{\xi}) \boldsymbol{P}_{\Phi}^{\perp}(\boldsymbol{\xi}) \dot{\boldsymbol{\mathcal{D}}}(\boldsymbol{\xi})) \odot (\boldsymbol{J}^T \boldsymbol{R}_s \boldsymbol{V}^H(\boldsymbol{\gamma}, \boldsymbol{\beta}) \\ &(\boldsymbol{I}_2 \otimes \boldsymbol{D}^H(\vartheta, \boldsymbol{\varphi})) \boldsymbol{\Phi}^H \boldsymbol{R}_x^{-1} \boldsymbol{\Phi} (\boldsymbol{I}_2 \otimes \boldsymbol{D}(\vartheta, \boldsymbol{\varphi})) \boldsymbol{V}(\boldsymbol{\gamma}, \boldsymbol{\beta}) \boldsymbol{R}_s \boldsymbol{J})^T \Big\}^{-1}, \end{aligned} \tag{5.22}$$

where $\dot{\boldsymbol{\mathcal{D}}}(\boldsymbol{\xi}) \in \mathbb{C}^{N \times 4P}$ is composed of partial derivatives and $\boldsymbol{J} \in \mathbb{N}^{P \times 4P}$ denotes a selection matrix. Both of these matrices can be found in [VII].

Expression (5.22) is an extension of the stochastic CRB for array processing [142] since it does not require closed-form expressions for the array steering vectors. This is an important feature since array nonidealities such as mutual coupling, cross-polarization effects and elements' directional beampatterns should be taken into account by the CRB but are

typically extremely challenging to describe in a closed-form. The bound in (5.22) overcomes such a difficulty by using manifold separation since the array nonidealities can be isolated from the wavefield parameters.

The tightness of the bound in (5.22) depends on the accuracy of the array sampling matrix, and thus to the accuracy of $\mathbf{\Phi}$ in (5.22). When the array response is fully known, expression (5.22) is exact in terms of numerical accuracy of the digital processor. In case of array calibration measurements, where measurement noise is unavoidable, expression (5.22) is typically tight for most of the calibration SNR employed in practice [55, 84]. Both of these observations follow from the superexponential decay of the sampling matrix, addressed in Chapter 4.

It should be noted that expression (5.22) is equivalent to the expression proposed in [108], where a representation in vector spherical harmonics is used. This follows from the equivalence matrix, described in Chapter 4. The advantages of using 2-D Fourier basis along with the equivalence matrix include simplicity of the derivatives and numerical accuracy. Indeed, vector spherical harmonics may suffer from numerical instabilities [78].

5.4 Numerical examples

The performance of the proposed array processing methods is illustrated next by numerical examples. First, two completely polarized signals are assumed to impinge on the polarimetric semi-spherical patch array depicted in Fig. 2.4-1. The signals are uncorrelated and their co-elevation angles are assumed to be identical and known ($\vartheta_1 = \vartheta_2 = \pi/2$). The azimuth angles of the sources are $\boldsymbol{\varphi} = [70^\circ, 80^\circ]^T$ while their polarization parameters are given by $\boldsymbol{\gamma} = [20^\circ, 10^\circ]^T$ and $\boldsymbol{\beta} = [10^\circ, 30^\circ]^T$. The SNR of both sources is 10dB. Figure 5.2 illustrates the performance of the polarimetric element-space root-MUSIC method in terms of root mean-squared error (RMSE) for a varying number of snapshots. The stochastic CRB is illustrated for comparison as well. It is a particular case of that in (5.22) and may be found in [21]. A discussion regarding the tightness of the CRB expression in (5.22) for real-world arrays can be found in Section 5.3 as well as in [VII].

The second example considers two fully-correlated signals impinging on the PSSPA. The co-elevation and azimuth angles are $\boldsymbol{\vartheta} = [70^\circ, 90^\circ]^T$ and $\boldsymbol{\varphi} = [40^\circ, 60^\circ]^T$, respectively. The polarization parameters of the sources are $\boldsymbol{\gamma} = [20^\circ, 10^\circ]^T$ and $\boldsymbol{\beta} = [10^\circ, 30^\circ]^T$. Figure 5.3 illustrates the per-

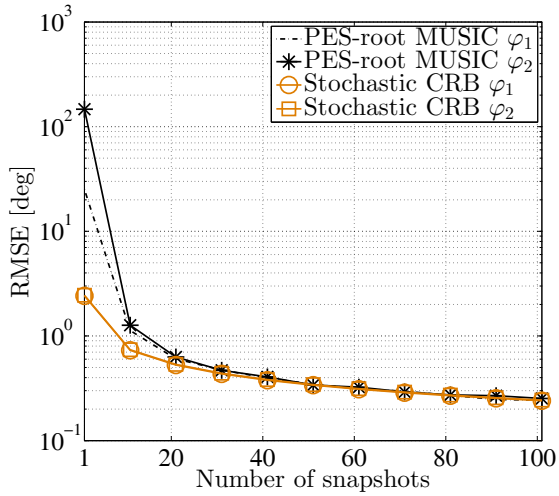

(a) Azimuth angle estimates.

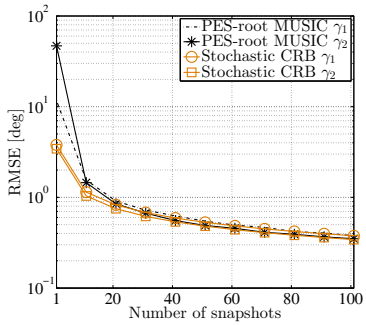

(b) Polarization parameter estimates.

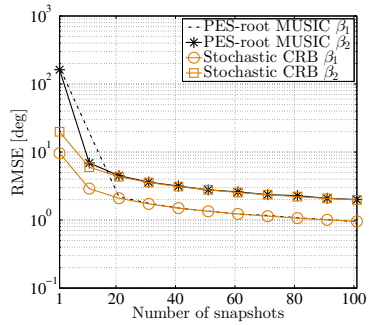

(c) Polarization parameter estimates.

Figure 5.2. Performance of the proposed PES root-MUSIC method in terms of RMSE for a varying number of snapshots. Two uncorrelated signals, with a signal-to-noise ratio of $\mathrm{SNR} = 10$dB, are assumed to impinge on the PSSPA depicted in Fig. 2.4-1 from $\boldsymbol{\varphi} = [70°, 80°]^T$. The co-elevation angle of the sources is assumed to be identical and known at $\vartheta_1 = \vartheta_2 = \pi/2$. The polarization parameters of the sources are $\boldsymbol{\gamma} = [20°, 10°]^T$ and $\boldsymbol{\beta} = [10°, 30°]^T$. The PES root-MUSIC has a performance close to the stochastic CRB.

formance of the polarimetric element-space WSF in terms of RMSE for varying SNR. It is assumed that $K = 50$ snapshots are acquired at the array output. The stochastic CRB is illustrated as well.

The last numerical example illustrates that using manifold separation in the robust Capon beamformer may increase the array output SINR. The robust Capon beamformer based on uncertainty sets is considered [93, 98, 168]. The SOI is assumed to impinge on the PSSPA from angles $\vartheta_{\mathrm{soi}} = 10°$ and $\varphi_{\mathrm{soi}} = 20°$. The polarization of the SOI is described by $\gamma_{\mathrm{soi}} = 5°$ and $\beta_{\mathrm{soi}} = 10°$. The SOI is observed in the presence of 8 equi-power

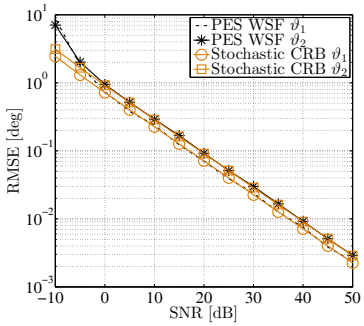

(a) Elevation angle estimates.

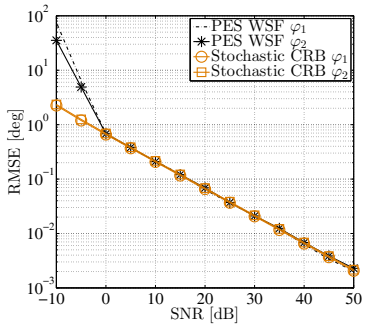

(b) Azimuth angle estimates.

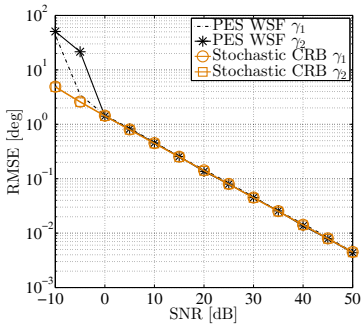

(c) Polarization parameter estimates.

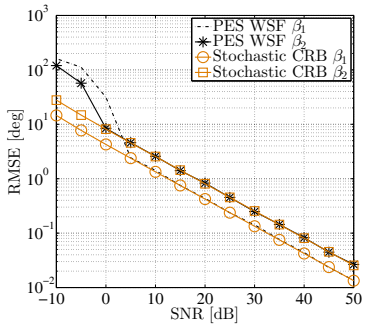

(d) Polarization parameter estimates.

Figure 5.3. Performance of the proposed PES WSF method in terms of RMSE for increasing SNR. Two fully correlated (coherent) signals are assumed to impinge on the PSSPA depicted in Fig. 2.4-1 from $\boldsymbol{\vartheta} = [70^\circ, 90^\circ]^T$ and $\boldsymbol{\varphi} = [40^\circ, 60^\circ]^T$. The polarization parameters of the sources are $\boldsymbol{\gamma} = [20^\circ, 10^\circ]^T$ and $\boldsymbol{\beta} = [10^\circ, 30^\circ]^T$. The number of snapshots acquired at the array output is $K = 50$. The PES WSF method has a performance very close to the stochastic CRB.

interfering signals as well as zero-mean complex circular Gaussian noise. Two types of errors in the steering vector are considered. In particular, they are due to uncertainties in the angle and polarization of the SOI as well as due to calibration measurement noise. The errors on the angle and polarization parameters are $\tilde{\vartheta}_{\text{soi}} = 5^\circ$, $\tilde{\varphi}_{\text{soi}} = 3^\circ$, $\tilde{\gamma}_{\text{soi}} = 2^\circ$, $\tilde{\beta}_{\text{soi}} = 5^\circ$. Moreover, array calibration measurements are acquired with $Q = 35 \times 34$ samples. The number of array snapshots is $K = 30$. Figure 5.4 illustrates the performance of the standard robust Capon beamformer (RCB) and the RCB obtained by using manifold separation technique (MST). Results show that employing manifold separation leads to improved array output SINR since it may capture array nonidealities and denoise calibration measurements.

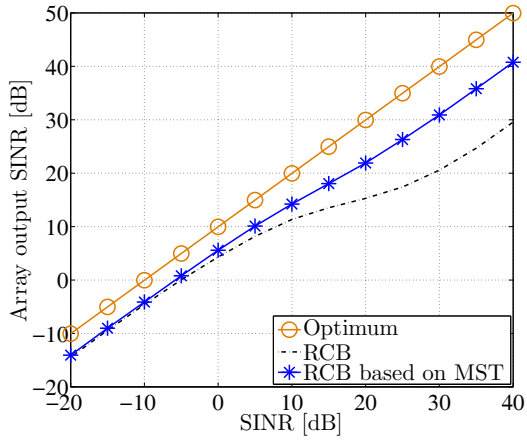

(a) Performance of the robust Capon beamformer for varying SINR.

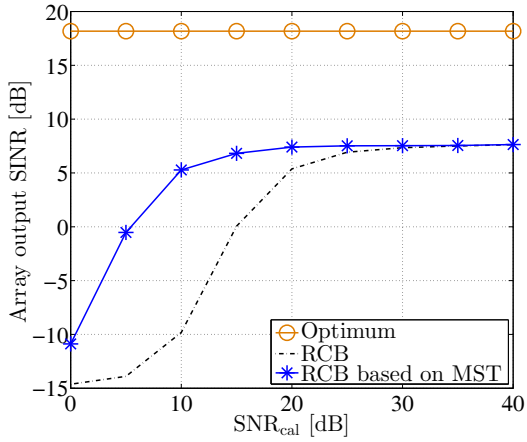

(b) Performance of the robust Capon beamformer for varying calibration measurement SNR and SINR $= 10$dB.

Figure 5.4. Performance of the standard robust Capon beamformer and the RCB obtained by using MST in terms of array output SINR. The SOI is assumed to impinge on the PSSPA from angles $\vartheta_{\mathrm{soi}} = 10^\circ$ and $\varphi_{\mathrm{soi}} = 20^\circ$. The polarization of the SOI is described by $\gamma_{\mathrm{soi}} = 5^\circ$ and $\beta_{\mathrm{soi}} = 10^\circ$. The SOI is observed in the presence of 8 equi-power interfering signals as well as zero-mean complex circular Gaussian noise. The number of array snapshots is $K = 30$. Two types of errors in the steering vector are considered, namely due to uncertainties in the angle and polarization of the SOI as well as due to calibration measurement noise. Employing manifold separation leads to improved SINR since it may capture array nonidealities and denoise calibration measurements.

5.5 Discussion

This chapter focuses on receive beamforming and subspace methods in the context of wavefield modeling and manifold separation. In particular,

the conventional and Capon beamformers are reformulated using manifold separation and equivalence matrix. Similarly, the MUSIC method, root-MUSIC, and weighted subspace fitting (WSF) approach are considered in the context of manifold separation based on 2-D Fourier basis. The proposed beamformers and subspace methods take into account array nonidealities and exploit the azimuth, elevation, and polarimetric domains of the sources. Significant computational savings are obtained by exploiting the Vandermonde structure of Fourier basis, namely the fast Fourier transform and polynomial rooting methods.

The proposed root-MUSIC method is based on manifold separation and equivalence matrix is not restricted to regular array geometries such as uniform linear arrays. The PES root-MUSIC estimates the azimuth angles and polarization of the sources by polynomial rooting for a fixed co-elevation angle. Alternatively, the co-elevation angles and polarization of the sources may be found from the roots of a polynomial by fixing the azimuth-angle. The proposed PES root-MUSIC is a computationally efficient method and fully takes into account array nonidealities that are common in real-world antenna arrays.

Estimating both azimuth *and* co-elevation angles by polynomial rooting is not considered in this chapter. A polynomial rooting method known as PRIME [56] has been considered in the context of manifold separation for joint azimuth and co-elevation angle estimation in [II]. However, such a method is of practical interest for antenna arrays with apertures in the order of one wavelength. Another approach for joint azimuth and co-elevation angle estimation consists in employing the rank reduction estimator (RARE) with manifold separation based Davis transform [115], [I]. See also Chapter 4. However, such an approach is appropriate for so-called oversampled arrays, only [31]. Informally, sensor arrays are called oversampled when the number of array elements is larger than the number of columns of the employed sampling matrix. Note that oversampled arrays are similar to large-scale MIMO systems [130].

It is important to emphasize that the complexity of the array processing methods proposed in this chapter scales with the number of columns of the sampling matrix. This may be a limiting factor for antenna arrays with very large apertures, relative to the wavelength. In such cases one may consider wavefield modeling and manifold separation in the context of sector-by-sector processing. Indeed, the number of columns of the sampling matrix may be reduced by processing data in angular sectors [28,29].

6. Conclusions

6.1 Summary

Array signal processing is used in many areas of engineering including wireless communications systems, radio astronomy and cosmology, radar and sonar applications, global navigation satellite systems and indoor positioning as well as in biomedicine. This dissertation contributes to wavefield modeling, array processing for arbitrary array geometries in the face of nonidealities. Moreover, novel results on harmonic analysis on the sphere are provided.

A rigorous generalization of wavefield modeling and manifold separation to vector-fields and diversely polarized antenna arrays is proposed. Scalar-fields such as acoustic pressure are a special case of the more general vector-field model. This contribution is important since many array processing applications deal with radio-frequency signals, and the polarization of the received signals may not be known. Exploiting the polarimetric domain may provide increased capacity, diversity and robustness to channel fading even in line-of-sight scenarios. The proposed generalization of manifold separation is important in many array processing tasks including parameter estimation and detection of fully correlated signals as well as in receive and transmit beamforming. These contributions are also useful in source tracking as well as in computationally-efficient solutions for high-resolution DoA estimation using sensor arrays of arbitrary geometries and in the face of nonidealities.

The proposed generalization of wavefield modeling and manifold separation to vector-fields employs vector spherical harmonic basis functions. This basis have a number of useful properties, including orthogonality on the sphere, invariance under rotations on $SO(3)$, and may be used to

give a compact representation of the array response. A rigorous derivation of the superexponential decaying property of the sampling matrix is provided, thus filling an important theoretical gap in the literature dealing with diversely polarized antenna arrays. The practical implications of these contributions are in indoor positioning based on antenna arrays, array calibration (measurements), and in large-scale MIMO systems.

A relationship between vector spherical harmonics and 2-D Fourier basis called equivalence matrix is established in this dissertation. This is important in areas of engineering dealing with data on a spherical manifold including measurement based radio channel modeling, biomedicine, 3-D beamforming and related array processing tasks. A number of results that follow from the equivalence matrix are established. These include a novel fast spherical harmonic transform, a reformulation of wavefield modeling and manifold separation in terms of 2-D Fourier basis, and a reduction of the estimation variance of the 2-D effective aperture distribution function (EADF). The theoretical implications of these contributions give more insight into the well-known discrete spherical harmonic transform, show the one-to-one mapping between spherical harmonic spectra and 2-D Fourier spectra, and lead to improvements of the minimum number of samples on the sphere that are needed in order to avoid aliasing. The practical relevance of the equivalence matrix is the possibility of employing the 2-D fast Fourier transform, along with its numerical robustness and low computational complexity, in areas of engineering that deal with data on a spherical manifold.

Signal processing methods for arbitrary array geometries and in the face of nonidealities are proposed. This is important since diversely polarized antenna arrays are typically subject to complex electromagnetic interactions among the array elements, thus changing the phase-centers and beampatterns of the array elements. Taking these array nonidealities into account prevents from steering unnecessary energy towards unwanted directions and from canceling the signal-of-interest. The conventional and Capon beamformers are extended to elevation, azimuth, and polarimetric domains by means of manifold separation and equivalence matrix. Similarly, the MUSIC method, root-MUSIC, and WSF technique are extended to elevation, azimuth, and polarization estimation as well as to arbitrary array geometries and arrays with nonidealities. Computationally-efficient implementations of the proposed beamforming techniques and subspace methods are provided. They are based on 2-D fast Fourier trans-

forms and polynomial rooting techniques. The practical relevance of these contributions are threefold. Firstly, the tedious task of describing array nonidealities using a high-dimensional parametric model is avoided. Secondly, establishing statistical performance bounds for sensor arrays with nonidealities is facilitated. Finally, computationally-efficient solutions to high-resolution signal processing methods are achieved without restricting the methods to regular array geometries.

6.2 Future research

Future research may consider employing auto-calibration techniques in the context of wavefield modeling. Array calibration in anechoic chambers may not be possible when the sensor array is mounted on a large platform such as an airplane or a vessel. In such a scenario, sector-by-sector processing and local basis may also be considered. Auto-calibration methods may exploit the array output model given by wavefield modeling, where the part depending on the wavefield is decoupled from that of the sensor array, and estimate both sampling matrix and coefficient vector in an alternating manner, for example.

A theoretical study of the condition number of the equivalence matrix is also desirable. Numerical results illustrate that the mapping provided by the equivalence matrix is numerically stable but a more rigorous analysis is necessary. It may also be useful to apply the equivalence matrix in other areas of engineering in addition to array processing.

Parametric estimation of distributed sources may also be considered in the context of wavefield modeling and manifold separation. The point-source model employed in this dissertation is not appropriate for describing rich scattering environments or large sources such as a ship hull, and if optimality is the goal, parametric estimation of distributed sources should be considered. Extensions of the Von-Mises distribution to the sphere include the Fisher as well as the Kent distributions [99].

Also, given that the sampling matrices of a group of users is known at the transmitter, one may synthesize a wavefield that is observable only by a desired user. This follows from the observation that the nullspace of the sampling matrix has nonzero dimension. Such a result may be useful in secure and multi-user communications.

Wavefield modeling may also be used in order to apply compressive sensing methods in rich scattering environments. This is important since most

of array processing methods based on compressive sensing exploit sparsity in the angular domain (point-source model), and may fail to work in rich scattering environments. However, the auto-correlation function of the coefficient vector in wavefield modeling is sparse even in rich scattering environments, which may be used to overcome the aforementioned limitation of compressive sensing methods. Such an observation follows from the so-called uncertainty principle and it is similar to the time-bandwidth product in spectral analysis [143, Ch. 2].

A. Appendix

A.1 Derivation of expression (4.25)

Let us start with the average-squared error:

$$\begin{aligned}\bar{\epsilon}^2(L) &= \frac{1}{4\pi}\int_{\mathcal{S}^2} \|\boldsymbol{\epsilon}_\theta(\vartheta,\varphi,L)\|^2 + \|\boldsymbol{\epsilon}_\phi(\vartheta,\varphi,L)\|^2\, d\Omega, \\ &= \sum_{n=1}^{N}\frac{1}{4\pi}\int_{\mathcal{S}^2} |\epsilon_n^\theta(\vartheta,\varphi,L)|^2 + |\epsilon_n^\phi(\vartheta,\varphi,L)|^2\, d\Omega. \end{aligned} \tag{A.1.1}$$

Using the Lipschitz condition [28] we may write:

$$\begin{aligned}&\frac{1}{4\pi}\int_{\mathcal{S}^2} |\epsilon_n^\theta(\vartheta,\varphi,L)|^2 + |\epsilon_n^\phi(\vartheta,\varphi,L)|^2\, d\Omega \\ &\leq \frac{1}{4\pi}\int_{\mathcal{S}^2} \alpha^2 \frac{1}{\frac{4\pi}{3}R_{\min}^3}\int_0^{R_{\min}}\int_{\mathcal{S}^2} \|\boldsymbol{\Psi}(\boldsymbol{r}) - \boldsymbol{\Psi}(\boldsymbol{r},L)\|^2\, r^2 d\Omega' dr d\Omega. \end{aligned} \tag{A.1.2}$$

Here, $\boldsymbol{\Psi}(\boldsymbol{r},L) \in \mathbb{C}^{2\times 1}$ denotes the wavefield decomposition in (4.17a) involving $\mathcal{L}$ terms, where $\mathcal{L} = 2L^2 + 4L$. Note that the time-domain variable t has been dropped for convenience. Moreover, $\alpha(\alpha < +\infty)$ denotes a finite constant, $\boldsymbol{r} = [r,\, \vartheta',\, \varphi']^T$ denotes a point in the 3-D Euclidean-space and $d\Omega' = \sin\vartheta' d\vartheta' d\varphi'$. Using Parvesal's theorem we get:

$$\begin{aligned}\frac{1}{4\pi}\int_{\mathcal{S}^2} \|\boldsymbol{\Psi}(\boldsymbol{r}) - \boldsymbol{\Psi}(\boldsymbol{r},L)\|^2\, d\Omega &= \frac{1}{4\pi}\sum_{\xi=\mathcal{L}+1}^{+\infty} \|\boldsymbol{h}_\xi(\boldsymbol{r})\|^2, \\ &= \frac{1}{4\pi}\sum_{\ell=L+1}^{+\infty} \frac{(2\ell+1)}{4\pi}\left(j_\ell^2(\kappa r) + \left(j_{\ell-1}(\kappa r) - \frac{\ell}{\kappa r} j_\ell(\kappa r)\right)^2\right), \end{aligned} \tag{A.1.3}$$

where the following results have been used [55, Appx. A1], [65, Ch. 9]:

$$\boldsymbol{h}_{1m\ell}(\boldsymbol{r}) = j_\ell(\kappa r)\boldsymbol{y}_{1m\ell}(\vartheta',\varphi'), \tag{A.1.4a}$$

$$\boldsymbol{h}_{2m\ell}(\boldsymbol{r}) = \frac{1}{\kappa r}\frac{\partial}{\partial(\kappa r)}\left\{\kappa r j_\ell(\kappa r)\right\}\boldsymbol{y}_{2m\ell}(\vartheta',\varphi'), \tag{A.1.4b}$$

$$\sum_{m=-\ell}^{+\ell}\|\boldsymbol{y}_{1m\ell}(\vartheta',\varphi')\|^2 = \sum_{m=-\ell}^{+\ell}\|\boldsymbol{y}_{2m\ell}(\vartheta',\varphi')\|^2 = \frac{2\ell+1}{4\pi}, \tag{A.1.4c}$$

$$\frac{1}{\kappa r}\frac{\partial}{\partial(\kappa r)}\left\{\kappa r j_\ell(\kappa r)\right\} = j_{\ell-1}(\kappa r) - \frac{\ell}{\kappa r}j_\ell(\kappa r). \tag{A.1.4d}$$

Assuming that $L > \lceil \kappa R_{\min} \rceil$, and absorbing constant terms into α, we may upper-bound the right-hand-side of expression (A.1.2) and finally obtain the following result:

$$\bar{\epsilon}^2(L) \leq N\alpha^2 \sum_{\ell=L+1}^{+\infty}(2\ell{+}1)\left(j_\ell^2(\kappa R_{\min}) + \left(j_{\ell-1}(\kappa R_{\min}) - \frac{\ell}{\kappa R_{\min}}j_\ell(\kappa R_{\min})\right)^2\right). \tag{A.1.5}$$

Let us now consider the following maximum error:

$$\begin{aligned}\epsilon_{\max}(L) &= \max_{(\vartheta,\varphi)}\|\boldsymbol{\epsilon}_\theta(\vartheta,\varphi,L)\|_1 + \|\boldsymbol{\epsilon}_\phi(\vartheta,\varphi,L)\|_1, \\ &= \max_{(\vartheta,\varphi)}\sum_{n=1}^{N}|\epsilon_\theta^n(\vartheta,\varphi,L)| + |\epsilon_\phi^n(\vartheta,\varphi,L)|.\end{aligned} \tag{A.1.6}$$

Using the Lipschitz condition, followed by triangle inequality and Parseval's theorem we get:

$$|\epsilon_\theta^n(\vartheta,\varphi,L)| + |\epsilon_\phi^n(\vartheta,\varphi,L)|$$

$$\leq \alpha\left(\frac{1}{\frac{4\pi}{3}R_{\min}^3}\int_0^{R_{\min}}\int_{\mathcal{S}^2}\|\sum_{\xi=\mathcal{L}+1}^{+\infty}\psi_\xi(\vartheta,\varphi)\,\boldsymbol{h}_\xi(\boldsymbol{r})\|^2\,r^2 d\Omega' dr\right)^{1/2}, \tag{A.1.7a}$$

$$\leq \alpha\sum_{\xi=\mathcal{L}+1}^{+\infty}\left(\frac{1}{\frac{4\pi}{3}R_{\min}^3}\int_0^{R_{\min}}\int_{\mathcal{S}^2}\|\psi_\xi(\vartheta,\varphi)\,\boldsymbol{h}_\xi(\boldsymbol{r})\|^2\,r^2 d\Omega' dr\right)^{1/2}, \tag{A.1.7b}$$

$$= \frac{\alpha}{\sqrt{4\pi/3}}\sum_{\ell=L+1}^{+\infty}\sum_{m=-\ell}^{+\ell}|\psi_{1\ell m}(\vartheta,\varphi)||j_\ell(\kappa R_{\min})| + |\psi_{2\ell m}(\vartheta,\varphi)|\left|j_{\ell-1}(\kappa R_{\min}) - \frac{\ell}{\kappa R_{\min}}j_\ell(\kappa R_{\min})\right|. \tag{A.1.7c}$$

Finally, using (A.1.4c) and Hölder's inequality we get:

$$\epsilon_{\max}(L) \leq N\alpha\sum_{\ell=L+1}^{+\infty}(2\ell{+}1)\left(|j_\ell(\kappa R_{\min})| + \left|j_{\ell-1}(\kappa R_{\min}) - \frac{\ell}{\kappa R_{\min}}j_\ell(\kappa R_{\min})\right|\right). \tag{A.1.8}$$

A.2 Closed-form expression for the equivalence matrix

The equivalence matrix may be found in a closed-form using the following results:

$$[\boldsymbol{y}_{1m\ell}(\vartheta,\varphi)]_\theta = -\frac{1}{2}\sqrt{\frac{2\ell+1}{4\pi}}\left[\mathrm{j}^{m-1}\boldsymbol{\Delta}_1^\ell + \mathrm{j}^{m+1}\boldsymbol{\Delta}_{-1}^\ell\right]^T \mathrm{diag}\{\boldsymbol{\Delta}_m^\ell\}\boldsymbol{d}(\vartheta)\mathrm{e}^{\mathrm{j}m\varphi} \tag{A.2.1a}$$

$$[\boldsymbol{y}_{1m\ell}(\vartheta,\varphi)]_\phi = \frac{1}{2}\sqrt{\frac{2\ell+1}{4\pi}}\left[\mathrm{j}^{m-1}\boldsymbol{\Delta}_1^\ell - \mathrm{j}^{m+1}\boldsymbol{\Delta}_{-1}^\ell\right]^T \mathrm{diag}\{\boldsymbol{\Delta}_m^\ell\}\boldsymbol{d}(\vartheta)\mathrm{e}^{\mathrm{j}m\varphi}, \tag{A.2.1b}$$

where $\boldsymbol{\Delta}_m^\ell \in \mathbb{R}^{(2\ell+1)\times 1}$ is given by

$$\boldsymbol{\Delta}_m^\ell = [\Delta_{-\ell,m}^\ell, \ldots, 0, \ldots, \Delta_{+\ell,m}^\ell]^T. \tag{A.2.2}$$

Here, $\Delta_{-\ell,m}^\ell$ denotes a so-called Wigner-d function evaluated at $\pi/2$ [55, Appx. A2], [79]. Note also that:

$$[\boldsymbol{y}_{2m\ell}(\vartheta,\varphi)]_\theta = -[\boldsymbol{y}_{1m\ell}(\vartheta,\varphi)]_\phi, \tag{A.2.3a}$$

$$[\boldsymbol{y}_{2m\ell}(\vartheta,\varphi)]_\phi = [\boldsymbol{y}_{1m\ell}(\vartheta,\varphi)]_\theta. \tag{A.2.3b}$$

The following results may also be useful:

$$\bar{\boldsymbol{\Xi}} = \frac{1}{2(Q-Q_a)}\boldsymbol{Y}(\boldsymbol{I}_2 \otimes \boldsymbol{\mathcal{R}}\boldsymbol{\mathcal{F}}^H\boldsymbol{J}) \tag{A.2.4}$$

$$\boldsymbol{Y} = \bar{\boldsymbol{\Xi}}(\boldsymbol{I}_2 \otimes \boldsymbol{J}^T\boldsymbol{\mathcal{F}}\boldsymbol{\mathcal{R}}^T\boldsymbol{C}), \tag{A.2.5}$$

where $\boldsymbol{\mathcal{R}} \in \mathbb{N}^{Q\times 2(Q-Q_a)}$ is given in (4.44) and $\boldsymbol{\mathcal{F}} \in \mathbb{C}^{2(Q-Q_a)\times 2(Q-Q_a)}$ denotes the 2-D DFT matrix. Such a matrix is defined as follows $\boldsymbol{\mathcal{F}} = \boldsymbol{\mathcal{F}}_{Q_a} \otimes \boldsymbol{\mathcal{F}}_{Q_e}$, where $\boldsymbol{\mathcal{F}}_{Q_a} \in \mathbb{C}^{Q_a\times Q_a}$ and $\boldsymbol{\mathcal{F}}_{Q_e} \in \mathbb{C}^{(2Q_e-Q_e)\times(2Q_e-Q_e)}$ denote 1-D DFT matrices. In (A.2.4), $\boldsymbol{J} \in \mathbb{N}^{2(Q-Q_a)\times\mathcal{M}}$ is a selection matrix given by:

$$\boldsymbol{J} = \left[\boldsymbol{0}\,\vdots\,\boldsymbol{I}_{\sqrt{\mathcal{M}}}\,\vdots\,\boldsymbol{0}\right] \otimes \left[\boldsymbol{0}\,\vdots\,\boldsymbol{I}_{\sqrt{\mathcal{M}}}\,\vdots\,\boldsymbol{0}\right], \tag{A.2.6}$$

while $\boldsymbol{C} \in \mathbb{R}^{Q\times Q}$ is given by:

$$\boldsymbol{C} = \boldsymbol{I}_{Q_a} \otimes \begin{bmatrix} 1 & & \\ & \frac{1}{2}\mathbf{I}_{Q_e-2} & \\ & & 1 \end{bmatrix}. \tag{A.2.7}$$

A.3 Derivation of expressions (4.45) and (4.46)

Using (A.2.4) in the least-squares estimator of the array sampling matrix (4.28) we get:

$$\hat{\boldsymbol{G}}_{\text{lse}} = \boldsymbol{B}(\boldsymbol{I}_2 \otimes \boldsymbol{C}\boldsymbol{\mathcal{R}}\boldsymbol{\mathcal{F}}^H\boldsymbol{J})\bar{\boldsymbol{\Xi}}^H(\bar{\boldsymbol{\Xi}}(\boldsymbol{I}_2 \otimes \boldsymbol{J}^T\boldsymbol{\mathcal{F}}\boldsymbol{\mathcal{R}}^T\boldsymbol{C}^2\boldsymbol{\mathcal{R}}\boldsymbol{\mathcal{F}}^H\boldsymbol{J})\bar{\boldsymbol{\Xi}}^H)^{-1} \tag{A.3.1}$$

$$= [\boldsymbol{\mathcal{B}}_\theta\boldsymbol{\mathcal{W}}_{\text{lse}}\boldsymbol{\mathcal{F}}^H\boldsymbol{J},\, \boldsymbol{\mathcal{B}}_\phi\boldsymbol{\mathcal{W}}_{\text{lse}}\boldsymbol{\mathcal{F}}^H\boldsymbol{J}]\bar{\boldsymbol{\Xi}}^H \times (\bar{\boldsymbol{\Xi}}(\boldsymbol{I}_2 \otimes \boldsymbol{J}^T\boldsymbol{\mathcal{F}}\boldsymbol{\mathcal{R}}^T\boldsymbol{C}^2\boldsymbol{\mathcal{R}}\boldsymbol{\mathcal{F}}^H\boldsymbol{J})\bar{\boldsymbol{\Xi}}^H)^{-1}, \tag{A.3.2}$$

where $\boldsymbol{\mathcal{W}}_{\text{lse}} \in \mathbb{R}^{2(Q-Q_a)\times 2(Q-Q_a)}$ denotes a diagonal matrix given by:

$$\boldsymbol{\mathcal{W}}_{\text{lse}} = \text{diag}\left\{\text{diag}\left\{\boldsymbol{C}\right\}^T\boldsymbol{\mathcal{R}}_2\right\}. \tag{A.3.3}$$

Here, $\boldsymbol{\mathcal{R}}_2 \in \mathbb{N}^{Q\times 2(Q-Q_a)}$ is given by:

$$\boldsymbol{\mathcal{R}}_2 = (\boldsymbol{I}_{Q_a} \otimes [\boldsymbol{I}_{Q_e},\, \boldsymbol{0}]) + \left(\boldsymbol{I}_{Q_a} \otimes \left[\boldsymbol{0},\, \left[\boldsymbol{0},\, \tilde{\boldsymbol{I}}_{Q_e-2}, \boldsymbol{0}\right]^T\right]\right). \tag{A.3.4}$$

Using (A.2.4) in the DVSHT-based sampling matrix estimator (4.30) we get:

$$\hat{\boldsymbol{G}}_{\text{dvsht}} = \boldsymbol{B}(\boldsymbol{I}_2 \otimes \boldsymbol{W}\boldsymbol{C}\boldsymbol{\mathcal{R}}\boldsymbol{\mathcal{F}}^H\boldsymbol{J})\bar{\boldsymbol{\Xi}}^H \tag{A.3.5}$$

$$= [\boldsymbol{\mathcal{B}}_\theta\boldsymbol{\mathcal{W}}_{\text{dvsht}}\boldsymbol{\mathcal{F}}^H\boldsymbol{J},\, \boldsymbol{\mathcal{B}}_\phi\boldsymbol{\mathcal{W}}_{\text{dvsht}}\boldsymbol{\mathcal{F}}^H\boldsymbol{J}]\bar{\boldsymbol{\Xi}}^H, \tag{A.3.6}$$

where $\boldsymbol{\mathcal{W}}_{\text{dvsht}} \in \mathbb{R}^{2(Q-Q_a)\times 2(Q-Q_a)}$ denotes a diagonal matrix given by:

$$\boldsymbol{\mathcal{W}}_{\text{dvsht}} = \text{diag}\left\{\text{diag}\left\{\boldsymbol{W}\boldsymbol{C}\right\}^T\boldsymbol{\mathcal{R}}_2\right\}. \tag{A.3.7}$$

Note that $\boldsymbol{W} \in \mathbb{R}^{Q\times Q}$ denotes a diagonal matrix containing the quadrature weights of the employed equiangular sampling rule.

Bibliography

[1] M. Abramowitz and I. A. Stegun, editors. *Handbook of Mathematical Functions with Formulas, Graphs, and Mathematical Tables*. Dover, New York, 1059 pages, 1964. *Cited on pages 33, 41, 48, 55, and 56.*

[2] F. Antreich, J. A. Nossek, G. Seco-Granados, and A. L. Swindlehurst. The extended invariance principle for signal parameter estimation in an unknown spatial field. *IEEE Transactions on Signal Processing*, 59(7):3213–3225, July 2011. *Cited on page 11.*

[3] H. Arslan and G. E. Bottomley. Channel estimation in narrowband wireless communication systems. *Wireless Communications and Mobile Computing*, 1(2):201–219, April/June 2001. *Cited on page 28.*

[4] D. Astely, A. L. Swindlehurst, and B. Ottersten. Spatial signature estimation for uniform linear arrays with unknown receiver gains and phases. *IEEE Transactions on Signal Processing*, 47(8):2128–2138, August 1999. *Cited on pages 16 and 24.*

[5] A. Azremi, M. Kyro, J. Ilvonen, J. Holopainen, S. Ranvier, C. Icheln, and P. Vainikainen. Five-element inverted-F antenna array for MIMO communications and radio direction finding on mobile terminal. In *Loughborough Antennas and Propagation Conference*, pages 557–560, 2009. *Cited on page 22.*

[6] A. J. Barabell. Improving the resolution performance of the eigenstructure-based direction-finding algorithms. In *IEEE International Conference on Acoustics, Speech, and Signal Processing*, pages 336–339, 1983. *Cited on page 84.*

[7] F. Belloni and V. Koivunen. Beamspace transform for UCA: Error analysis and bias reduction. *IEEE Transactions on Signal Processing*, 54(8):3078–3089, August 2006. *Cited on pages 33, 82, and 84.*

[8] F. Belloni, V. Ranki, A. Kainulainen, and A. Richter. Angle-based indoor positioning system for open indoor environments. In *Workshop on Positioning, Navigation and Communication*, pages 261–265, 2009. *Cited on pages 1, 13, 45, and 71.*

[9] F. Belloni, A. Richter, and V. Koivunen. DoA estimation via manifold separation for arbitrary array structures. *IEEE Transactions on Signal Processing*, 55(10):4800–4810, October 2007. *Cited on pages 30, 35, 40, 51, and 84.*

[10] M. Bengtsson and B. Ottersten. A generalization of weighted subspace fitting to full-rank models. *IEEE Transactions on Signal Processing*, 49(5):1002–1012, May 2001. *Cited on pages 82 and 86.*

[11] D. A. Bini, P. Boito, Y. Eidelman, L. Gemignani, and I. Gohberg. A fast implicit QR eigenvalue algorithm for companion matrices. *Linear Algebra and its Applications*, 432(8):2006–2031, April 2010. *Cited on page 85.*

[12] J. Blais. Discrete spherical harmonic transforms for equiangular grids of spatial and spectral data. *Journal of Geodetic Science*, 1(1):9–16, March 2011. *Cited on pages 39, 52, 62, and 66.*

[13] H. Bölcskei, D. Gesbert, C. B. Papadias, and A.-J. van der Veen, editors. *Space-Time Wireless Systems: From Array Processing to MIMO communications*. Cambridge University Press, 575 pages, 2006. *Cited on page 1.*

[14] M. Bühren, M. Pesavento, and J. F. Böhme. A new approach to array interpolation by generation of artificial shift invariances: Interpolated ESPRIT. In *IEEE International Conference on Acoustics, Speech, and Signal Processing*, volume 5, pages 205–208, 2003. *Cited on pages 31 and 72.*

[15] M. Bühren, M. Pesavento, and J. F. Böhme. Virtual array design for array interpolation using differential geometry. In *IEEE International Conference on Acoustics, Speech, and Signal Processing*, volume 2, pages 229–232, 2004. *Cited on pages 31 and 72.*

[16] J. Capon. High-resolution frequency-wavenumber spectrum analysis. *Proceedings of the IEEE*, 57(8):1408–1418, August 1969. *Cited on page 78.*

[17] J. F. Cardoso. Precision cosmology with the cosmic microwave background. *IEEE Signal Processing Magazine*, 27(1):55–66, January 2010. *Cited on pages 1, 39, 66, and 76.*

[18] B. Carlson. Covariance matrix estimation errors and diagonal loading in adaptive arrays. *IEEE Transactions on Aerospace and Electronic Systems*, 24(4):397–401, July 1988. *Cited on pages 27, 79, and 80.*

[19] W. C. Cheuk, M. Trinkle, and D. A. Gray. Null-steering LMS dual-polarised adaptive antenna arrays for GPS. *Journal of Global Positioning Systems*, 4(1-2):258–267, 2005. *Cited on page 45.*

[20] P.-J. Chung and J. F. Böhme. The methodology of the maximum likelihood approach: Estimation, detection, and exploration of seismic events. *IEEE Signal Processing Magazine*, 29(3):40–46, May 2012. *Cited on page 1.*

[21] M. Costa and V. Koivunen. Application of manifold separation to polarimetric Capon beamformer and source tracking. *submitted to IEEE Transactions on Signal Processing*. *Cited on pages 78, 79, 80, 83, 85, and 88.*

[22] M. Costa, A. Richter, and V. Koivunen. Model order selection in sensor array response modeling. In *45th IEEE Asilomar Conference on Signals, Systems, and Computers, Pacific Grove, California, USA, November*, pages 634–638, 2011. *Cited on pages 45, 51, and 71.*

[23] H. Cox, R. M. Zeskind, and M. M. Owen. Robust adaptive beamforming. *IEEE Transactions on Acoustics, Speech, and Signal Processing*, ASSP-35(10):1365–1376, October 1988. *Cited on page 79.*

[24] D. E. N. Davies. A transformation between the phasing techniques required for linear and circular aerial arrays. *Proceedings of the IEE*, 112(11):2041–2045, November 1965. *Cited on pages 32, 33, 34, and 44.*

[25] D. E. N. Davies. Circular arrays. In A. W. Rudge, K. Milne, A. D. Olver, and P. Knight, editors, *The Handbook of Antenna Design*, volume 2, chapter 12, pages 298–328. Peter Peregrinus Ltd., 1983. *Cited on pages 32, 33, 34, and 44.*

[26] G. A. Deschamps. Geometrical representation of the polarization of a plane electromagnetic wave. *Proceedings of the IRE*, 39(5):540–544, May 1951. *Cited on page 14.*

[27] G. A. Dilts. Computation of spherical harmonic expansion coefficients via FFTs. *Journal of Computational Physics*, 57(3):439–453, 1985. *Cited on pages 66 and 67.*

[28] M. A. Doron and E. Doron. Wavefield modeling and array processing, part I - spatial sampling. *IEEE Transactions on Signal Processing*, 42(10):2549–2559, October 1994. *Cited on pages 30, 31, 33, 34, 35, 36, 40, 41, 42, 43, 44, 48, 72, 92, and 97.*

[29] M. A. Doron and E. Doron. Wavefield modeling and array processing, part II - algorithms. *IEEE Transactions on Signal Processing*, 42(10):2560–2570, October 1994. *Cited on pages 30, 35, 72, 86, and 92.*

[30] M. A. Doron and E. Doron. Wavefield modeling and array processing, part III - resolution capacity. *IEEE Transactions on Signal Processing*, 42(10):2571–2580, October 1994. *Cited on pages 30, 34, and 35.*

[31] M. A. Doron and E. Doron. Reduced rank processing for oversampled arrays. *IEEE Transactions on Signal Processing*, 44(4):900–911, April 1996. *Cited on page 92.*

[32] J. R. Driscoll and D. M. Healy. Computing Fourier transforms and convolutions on the 2-sphere. *Advances in Applied Mathematics*, 15:202–250, 1994. *Cited on page 66.*

[33] L. Du, J. Li, and P. Stoica. Fully automatic computation of diagonal loading levels for robust adaptive beamforming. *IEEE Transactions on Aerospace and Electronic Systems*, 46(1):449–458, January 2010. *Cited on page 80.*

[34] L. Du, T. Yardibi, J. Li, and P. Stoica. Review of user parameter-free robust adaptive beamforming algorithms. *Digital Signal Processing*, 19(4):567–582, July 2009. *Cited on page 80.*

[35] R. Eiges and H. D. Griffiths. Mode-space spatial spectral estimation for circular arrays. *IEE Proceedings - Radar, Sonar, Navigation*, 141(6):300–3006, December 1994. *Cited on page 33.*

[36] E. R. Ferrara and T. M. Parks. Direction finding with an array of antennas having diverse polarizations. *IEEE Transactions on Antennas and Propagation*, 31(2):231– 236, March 1983. *Cited on pages 82 and 83.*

[37] A. Ferréol, P. Larzabal, and M. Viberg. On the asymptotic performance analysis of subspace DOA estimation in the presence of modeling errors: Case of MUSIC. *IEEE Transactions on Signal Processing*, 54(3):907–920, March 2006. *Cited on page 82.*

[38] A. Ferréol, P. Larzabal, and M. Viberg. Statistical analysis of the MUSIC algorithm in the presence of modeling errors, taking into account the resolution probability. *IEEE Transactions on Signal Processing*, 58(8):4156–4166, August 2010. *Cited on page 82.*

[39] J. A. Fessler and A. O. Hero. Space-alternating generalized expectation-maximization algorithm. *IEEE Transactions on Signal Processing*, 42(10):2664–2677, October 1994. *Cited on page 24.*

[40] B. Friedlander. The root–MUSIC algorithm for direction finding with interpolated arrays. *Signal Processing*, 30(1):15–19, January 1993. *Cited on pages 6, 31, 32, and 72.*

[41] B. Friedlander and A. J. Weiss. Direction finding using spatial smoothing with interpolated arrays. *IEEE Transactions on Aerospace and Electronic Systems*, 28(2):574–587, April 1992. *Cited on page 31.*

[42] G. D. Galdo. *Geometry-based Channel Modeling for Multi-User MIMO Systems and Applications*. PhD thesis, Ilmenau University of Technology, http://www.delgaldo.com/research/delgaldo_phd_final_online.pdf, 2007. *Cited on pages 50, 52, 53, 55, 58, 62, and 65.*

[43] G. D. Galdo, J. Lotze, M. Landmann, and M. Haardt. Modelling and manipulation of polarimetric antenna beam patterns via spherical harmonics. In 14*th European Signal Processing Conference, Florence, Italy, September*, 2006. *Cited on pages 58 and 65.*

[44] W. Gautschi. Computational aspects of three-term recurrence relations. *Society of Industrial and Applied Mathematics (SIAM) Review*, 9(1):24–82, January 1967. *Cited on page 58.*

[45] C. Gennarelli, A. Capozzoli, L. J. Foged, J. Fordham, and D. J. van Rensburg, editors. *Recent Advances in Near-Field to Far-Field Transformation Techniques*, volume 2012. (Special Issue) International Journal of Antennas and Propagation, 2012. *Cited on pages 27 and 30.*

[46] A. Gershman. Robust adaptive beamforming in sensor arrays. *International Journal of Electronics and Communications*, 53(6):305–314, 1999. *Cited on pages 18, 20, 23, 25, 75, 77, 78, 79, and 80.*

[47] A. Gershman and J. Böhme. A note on most favorable array geometries for DOA estimation and array interpolation. *IEEE Signal Processing Letters*, 4(8):232–235, August 1997. *Cited on pages 31 and 72.*

[48] A. B. Gershman, N. D. Sidiropoulos, S. Shahbazpanahi, M. Bengtsson, and B. Ottersten. Convex optimization-based beamforming. *IEEE Signal Processing Magazine*, 27(3):62–75, May 2010. *Cited on pages 25, 76, 78, 79, 80, and 81.*

[49] L. C. Godara. *Smart Antennas*. CRC Press, 448 pages, 2004. *Cited on pages 1, 78, and 79.*

[50] G. H. Golub and C. F. Van Loan. *Matrix Computations*. John Hopkins University Press, third edition, 687 pages, 1996. *Cited on pages 84 and 85.*

[51] R. Goossens and H. Rogier. A hybrid UCA-RARE/root-MUSIC approach for 2-D direction of arrival estimation in uniform circular arrays in the presence of mutual coupling. *IEEE Transactions on Antennas and Propagation*, 55(3):841–849, March 2007. *Cited on page 35.*

[52] R. Goossens and H. Rogier. Unitary spherical ESPRIT: 2-D angle estimation with spherical arrays for scalar fields. *IET Signal Processing*, 3(3):221–231, May 2009. *Cited on pages 33 and 35.*

[53] J. D. Gordman and A. O. Hero. Lower bound for parametric estimation with constraints. *IEEE Transactions on Information Theory*, 26(6):1285–1301, November 1990. *Cited on page 64.*

[54] M. S. Grewal, A. P. Andrews, and C. G. Bartone. *Global Navigation Satellite Systems, Inertial Navigation, and Integration*. John Wiley & Sons, Inc., third edition, 561 pages, 2013. *Cited on page 1.*

[55] J. E. Hansen, editor. *Spherical Near-Field Antenna Measurements*. Peter Peregrinus Ltd., 377 pages, 1988. *Cited on pages 12, 20, 30, 46, 47, 50, 51, 52, 67, 68, 88, 98, and 99.*

[56] G. F. Hatke. Superresolution source location with planar arrays. *The Lincoln Laboratory Journal*, 10(2):127–146, November 1997. *Cited on pages 7 and 92.*

[57] G. F. Hatke and K. W. Forsythe. A class of polynomial rooting algorithms for joint azimuth/elevation estimation using multidimensional arrays. In *28th IEEE Asilomar Conference on Signals, Systems and Computers, Pacific Grove, California, USA, November-October*, volume 1, pages 694–699, 1995. *Cited on page 7.*

[58] J. He, M. O. Ahmad, and M. N. S. Swamy. Near-field localization of partially polarized sources with a cross-dipole array. *IEEE Transactions on Aerospace and Electronic Systems*, 49(2):857–870, April 2013. *Cited on page 82.*

[59] D. M. Healy, D. Rockmore, P. J. Kostelec, and S. S. Moore. FFTs for the 2-sphere - improvements and variations. *The Journal of Fourier Analysis and Applications*, 9:341–385, 1998. *Cited on pages 55 and 66.*

[60] B. Hochwald and A. Nehorai. Polarimetric modeling and parameter estimation with applications to remote sensing. *IEEE Transactions on Signal Processing*, 43(8):1923–1935, August 1995. *Cited on page 13.*

[61] B. Hochwald and A. Nehorai. Identifiability in array processing models with vector-sensor applications. *IEEE Transactions on Signal Processing*, 44(1):83–95, January 1996. *Cited on pages 14 and 16.*

[62] M. Hurtado, J. J. Xiao, and Arye Nehorai. Target estimation, detection, and tracking. *IEEE Signal Processing Magazine*, 26(1):42–52, January 2009. *Cited on pages 18 and 45.*

[63] P. Hyberg, M. Jansson, and B. Ottersten. Array interpolation and bias reduction. *IEEE Transactions on Signal Processing*, 52(10):2711–2720, October 2004. *Cited on pages 31 and 32.*

[64] P. Hyberg, M. Jansson, and B. Ottersten. Array interpolation and DOA MSE reduction. *IEEE Transactions on Signal Processing*, 53(12):4464–4471, December 2005. *Cited on pages 31, 32, and 72.*

[65] J. D. Jackson. *Classical Electrodynamics*. John Wiley & Sons, Inc., third edition, 808 pages, 1999. *Cited on pages 2, 46, and 98.*

[66] M. Jansson, A. L. Swindlehurst, and B. Ottersten. Weighted subspace fitting for general array error models. *IEEE Transactions on Signal Processing*, 46(9):2484–2498, September 1998. *Cited on pages 20, 25, and 86.*

[67] D. H. Johnson and D. E. Dudgeon. *Array Signal Processing: Concepts and Techniques*. PTR Prentice-Hall, Inc., 523 pages, 1993. *Cited on pages 12 and 17.*

[68] S. Kay. Exponentially embedded families - new approaches to model order estimation. *IEEE Transactions on Aerospace and Electronic Systems*, 41(1):333–345, January 2005. *Cited on pages 51 and 71.*

[69] S. Kay. *Fundamentals of Statistical Signal Processing: Estimation Theory*. Prentice Hall, 589 pages, 1993. *Cited on pages 16, 25, 28, 52, 64, and 87.*

[70] P. Kemppi, T. Rautiainen, V. Ranki, F. Belloni, and J. Pajunen. Hybrid positioning system combining angle-based localization, pedestrian dead reckoning, and map-filtering. In *International Conference on Indoor Positioning and Indoor Navigation, Zurich, Switzerland, September*, pages 1–7, 2010. *Cited on pages 1, 13, and 71.*

[71] R. A. Kennedy, P. Sadeghi, T. D. Abhayapala, and H. M. Jones. Intrinsic limits of dimensionality and richness in random multipath fields. *IEEE Transactions on Signal Processing*, 55(6):2542–2556, June 2007. *Cited on pages 42 and 71.*

[72] Z. Khalid, S. Durrani, P. Sadeghi, and R. A. Kennedy. Spatio-spectral analysis on the sphere using spatially localized spherical harmonics transform. *IEEE Transactions on Signal Processing*, 60(3):1487–1492, March 2012. *Cited on page 72.*

[73] Z. Khalid, R. A. Kennedy, S. Durrani, P. Sadeghi, Y. Wiaux, and J. D. McEwen. Fast directional spatially localized spherical harmonic transform. *IEEE Transactions on Signal Processing*, 61(9):2192–2203, May 2013. *Cited on page 72.*

[74] R. Klemm. *Principles of Space-Time Adaptive Processing*. The Institution of Electrical Engineers, 620 pages, 2002. *Cited on page 12.*

[75] R. Klemm, editor. *Applications of Space-Time Adaptive Processing*. The Institution of Engineering and Technology, 909 pages, 2004. *Cited on page 1.*

[76] P. Koivisto. Reduction of errors in antenna radiation patterns using optimally truncated spherical wave expansion. *Progress in Electromagnetics Research*, 47:313–333, 2004. *Cited on page 50.*

[77] V. Koivunen and E. Ollila. Direction of arrival estimation under uncertainty. In Sathish Chandran, editor, *Advances in Direction of Arrival Estimation*, chapter 12, pages 241–258. Artech House, 2006. *Cited on pages 18, 23, 25, and 75.*

[78] P. Kostelec, D. K Maslen, D. M. Healy Jr., and D. N. Rockmore. Computational harmonic analysis for tensor fields on the two-sphere. *Journal of Computational Physics*, 162(2):514–535, August 2000. *Cited on pages 46, 47, 50, 52, 53, 55, 62, 66, and 88.*

[79] P. J. Kostelec and D. N. Rockmore. FFTs on the rotation group. *Journal of Fourier Analysis and Applications*, 14(2):145–179, April 2008. *Cited on pages 68 and 99.*

[80] H. Krim and M. Viberg. Two decades of array signal processing. *IEEE Signal Processing Magazine*, pages 67–94, July 1996. *Cited on pages 17, 39, 57, 66, 76, 77, 78, 79, 81, and 82.*

[81] K. Kumatani, J. McDonough, and B. Raj. Microphone array processing for distant speech recognition. *IEEE Signal Processing Magazine*, 29(6):127–140, November 2012. *Cited on page 1.*

[82] S. Kunis and D. Potts. Fast spherical Fourier algorithms. *Journal of Computational and Applied Mathematics*, 161(1):75–98, December 2003. *Cited on page 66.*

[83] H. Kwok-Chiang, T. Kah-Chye, and A. Nehorai. Estimating directions of arrival of completely and incompletely polarized signals with electromagnetic vector sensors. *IEEE Transactions on Signal Processing*, 47(10):2845–2852, October 1999. *Cited on pages 18 and 19.*

[84] M. Landmann. *Limitations of Experimental Channel Characterization*. PhD thesis, Ilmenau University of Technology, http://www.db-thueringen.de/servlets/DerivateServlet/Derivate-15967/ilm1-2008000090.pdf, 2008. *Cited on pages 1, 51, 58, 65, 67, and 88.*

[85] M. Landmann, M. Käske, and R. S. Thomä. Impact of incomplete and inaccurate data models on high resolution parameter estimation in multidimensional channel sounding. *IEEE Transactions on Antennas and Propagation*, 60(2):557–573, February 2012. *Cited on pages 15, 20, 29, 30, 45, and 65.*

[86] M. Landmann, A. Richter, and R. S. Thomä. DoA resolution limits in MIMO channel sounding. In *International Symposium on Antennas and Propagation and USNC/URSI National Radio Science Meeting, Monterey, CA, USA, June*, volume 2, pages 1708–1711, 2004. *Cited on pages 58 and 65.*

[87] M. Landmann, A. Richter, and R. S. Thomä. Performance evaluation of antenna arrays for high-resolution DoA estimation in channel sounding. In *International Symposium on Antennas and Propagation, Sendai, Japan, August*, 2004. *Cited on page 22.*

[88] B. K. Lau, Y. H. Leung, Y. Liu, and K. L. Teo. Transformations for nonideal uniform circular arrays operating in correlated signal environments. *IEEE Transactions on Signal Processing*, 54(1):34–48, January 2006. *Cited on pages 34, 35, 44, and 82.*

[89] R. Levanda and A. Leshem. Synthetic aperture radio telescopes: A look at image formation techniques. *IEEE Signal Processing Magazine*, 27(1):14–29, January 2010. *Cited on pages 1, 39, and 66.*

[90] J. Li. Direction and polarization estimation using arrays with small loops and short dipoles. *IEEE Transactions on Antennas and Propagation*, 41(3):379–387, March 1993. *Cited on pages 18 and 19.*

[91] J. Li and P. Stoica. Efficient parameter estimation of partially polarized electromagnetic waves. *IEEE Transactions on Signal Processing*, 42(11):3114–3125, November 1994. *Cited on pages 14 and 19.*

[92] J. Li and P. Stoica, editors. *Robust Adaptive Beamforming*. John Wiley & Sons, Inc., 422 pages, 2006. *Cited on pages 25, 78, 79, and 80.*

[93] J. Li, P. Stoica, and Z. Wang. On robust Capon beamforming and diagonal loading. *IEEE Transactions on Signal Processing*, 51(7):1702–1715, July 2003. *Cited on pages 26, 27, 80, 81, and 89.*

[94] J. P. Lie, T. Blu, and C.-M. S. See. Single antenna power measurements based direction finding. *IEEE Transactions on Signal Processing*, 58(11):5682–5692, November 2010. *Cited on page 65.*

[95] J. P. Lie, T. Blu, and C.-M. S. See. Azimuth-elevation direction finding using power measurements from single antenna. In *IEEE International Conference on Acoustics, Speech, and Signal Processing*, pages 2608–2611, 2011. *Cited on page 65.*

[96] J. P. Lie, T. Blu, and C.-M. S. See. Single antenna power measurements based direction finding with incomplete spatial coverage. In *IEEE International Conference on Acoustics, Speech, and Signal Processing*, pages 2641–2644, 2012. *Cited on page 65.*

[97] I. D. Longstaff, P. E. K. Chow, and D. E. N. Davies. Directional properties of circular arrays. *Proceedings of the IEE*, 114(6):713–718, June 1967. *Cited on pages 32, 33, and 34.*

[98] R. G. Lorenz and S. P. Boyd. Robust minimum variance beamforming. *IEEE Transactions on Signal Processing*, 53(5):1684–1696, May 2005. *Cited on pages 26, 80, 81, and 89.*

[99] K. V. Mardia and P. E. Jupp. *Directional Statistics*. John Wiley & Sons, Ldt., 415 pages, 2000. *Cited on page 95.*

[100] C. P. Mathews and M. D. Zoltowski. Eigenstructure techniques for 2-D angle estimation with uniform circular arrays. *IEEE Transactions on Signal Processing*, 42(9):2395–2407, September 1994. *Cited on pages 6, 33, 34, and 84.*

[101] J. D. McEwen and Y. Wiaux. A novel sampling theorem on the sphere. *IEEE Transactions on Signal Processing*, 59(12):5876–5887, December 2011. *Cited on pages 55, 62, 66, and 68.*

[102] M. J. Mohlenkamp. A fast transform for spherical harmonics. *The Journal of Fourier Analysis and Applications*, 5(2-3):159–184, 1999. *Cited on page 66.*

[103] A. Moreira, P. Prats-Iraola, M. Younis, G. Krieger, I. Hajnsek, and K. P. Papathanassiou. A tutorial on synthetic aperture radar. *IEEE Geoscience and Remote Sensing Magazine*, 1(1):6–43, March 2013. *Cited on page 1.*

[104] A. Nehorai, K. C. Ho, and B. T. G. Tan. Minimum-noise-variance beamformer with an electromagnetic vector sensor. *IEEE Transactions on Signal Processing*, 47(3):601–618, March 1999. *Cited on pages 14 and 18.*

[105] A. Nehorai and E. Paldi. Vector-sensor array processing for electromagnetic source localization. *IEEE Transactions on Signal Processing*, 42(2):376–398, February 1994. *Cited on pages 14 and 18.*

[106] U. Nickel. Algebraic formulation of Kumaresan-Tufts superresolution method, showing relation to ME and MUSIC methods. *IEE Proceedings F Communications, Radar and Signal Processing*, 135(1):7–10, February 1988. *Cited on page 79.*

[107] U. Nickel. On the influence of channel errors on array signal processing methods. *International Journal of Electronics and Communications*, 47(4):209–219, 1993. *Cited on page 14.*

[108] S. Nordebo, M. Gustafsson, and J. Lundbäck. Fundamental limitations for DOA and polarization estimation with applications in array signal processing. *IEEE Transactions on Signal Processing*, 54(10):4055–4061, October 2006. *Cited on pages 50 and 88.*

[109] B. Ottersten, M. Viberg, and T. Kailath. Analysis of subspace fitting and ML techniques for parameter estimation from sensor array data. *IEEE Transactions on Signal Processing*, 40(3):590–600, March 1992. *Cited on pages 16, 24, 86, and 87.*

[110] B. Ottersten, M. Viberg, P. Stoica, and A. Nehorai. Exact and large sample maximum likelihood techniques for parameter estimation and detection in array processing. In Haykin, Litva, and Shepherd, editors, *Radar Array Processing*, chapter 4, pages 99–151. Springer-Verlag, 1993. *Cited on pages 81 and 86.*

[111] I. J. Myung P. D. Grünwald and M. A. Pitt, editors. *Advances in Minimum Description Length: Theory and Applications*. MIT Press, 435 pages, 2005. *Cited on page 30.*

[112] V. Y. Pan. Solving a polynomial equation: Some history and recent progress. *Society for Industrial and Applied Mathematics*, 39(2):187–220, June 1997. *Cited on page 85.*

[113] A. Paulraj, R. Nabar, and D. Gore. *Introduction to Space-Time Wireless Communications*. Cambridge University Press, 272 pages, 2003. *Cited on page 1.*

[114] M. Pesavento, A. B. Gershman, and Z. Q. Luo. Robust array interpolation using second-order cone programming. *IEEE Signal Processing Letters*, 9(1):8–11, January 2002. *Cited on page 32.*

[115] M. Pesavento, C. F. Mecklenbräuker, and J. F. Böhme. Multidimensional rank reduction estimator for parametric MIMO channel models. *EURASIP Journal on Advances in Signal Processing*, 2004(9):1354–1363, 2004. *Cited on pages 83 and 92.*

[116] V. F. Pisarenko. The retrieval of harmonics from a covariance function. *Geophysical Journal of the Royal Astronomical Society*, 33(3):347–366, September 1973. *Cited on page 82.*

[117] A. S. Y. Poon, R. W. Brodersen, and D. N. C. Tse. Degrees of freedom in multiple-antenna channels: A signal space approach. *IEEE Transactions on Information Theory*, 51(2):523–536, February 2005. *Cited on pages 42, 45, and 71.*

[118] B. Rafaely. Plane-wave decomposition of the sound field on a sphere by spherical convolution. *Journal of the Acoustical Society of America*, 116(4):2149–2157, October 2004. *Cited on pages 34 and 35.*

[119] B. Rafaely. Analysis and design of spherical microphone arrays. *IEEE Transactions on Speech and Audio Processing*, 13(1):135–143, January 2005. *Cited on pages 35, 50, 52, 53, 54, and 62.*

[120] B. Rafaely and M. Kleider. Spherical microphone array beam steering using Wigner-D weighting. *IEEE Signal Processing Letters*, 15:417–420, 2008. *Cited on page 35.*

[121] B. Rafaely and M. Kleider. Spherical microphone array beam steering using Wigner-D weighting. *IEEE Signal Processing Letters*, 15:417–420, 2008. *Cited on page 76.*

[122] B. Rafaely, B. Weiss, and Eitan Bachmat. Spatial aliasing in spherical microphone arrays. *IEEE Transactions on Signal Processing*, 55(3):1003–1010, March 2007. *Cited on page 35.*

[123] J. Rahola, F. Belloni, and A. Richter. Modelling of radiation patterns using scalar spherical harmonics with vector coefficients. In *3rd European Conference on Antennas and Propagation, Berlin, Germany, March*, pages 3361–3365, 2009. *Cited on page 52.*

[124] B. D. Rao and K. V. S. Hari. Performance analysis of root-MUSIC. *IEEE Transactions on Acoustics, Speech, and Signal Processing*, 37(12):1939–1949, December 1989. *Cited on page 84.*

[125] A. Richter. *Estimation of Radio Channel Parameters: Models and Algorithms*. PhD thesis, Ilmenau University of Technology, http://www.db-thueringen.de/servlets/DerivateServlet/Derivate-7407/ilm1-2005000111.pdf, 2005. *Cited on pages 1, 11, 13, 58, and 65.*

[126] J. Rissanen. MDL denoising. *IEEE Transactions on Information Theory*, 46(7):2537–2543, November 2000. *Cited on pages 45, 51, and 71.*

[127] Y. Rockah and P. Schultheiss. Array shape calibration using sources in unknown locations - part I: Far-field sources. *IEEE Transactions on Acoustics, Speech and Signal Processing*, 35(3):286–299, March 1987. *Cited on page 24.*

[128] R. Roy and T. Kailath. ESPRIT - estimation of signal parameters via rotational invariance techniques. *IEEE Transactions on Acoustics, Speech, and Signal Processing*, 37(7):984–995, July 1989. *Cited on page 31.*

[129] M. Rübsamen and A. B. Gershman. Direction-of-arrival estimation for nonuniform sensor arrays: From manifold separation to Fourier domain MUSIC methods. *IEEE Transactions on Signal Processing*, 57(2):588–599, February 2009. *Cited on pages 82, 85, and 86.*

[130] F. Rusek, D. Persson, B. K. Lau, E. G. Larsson, T. L. Marzetta, O. Edfors, and F. Tufvesson. Scaling up MIMO: Opportunities and challenges with very large arrays. *IEEE Signal Processing Magazine*, 30(1):40–60, January 2013. *Cited on pages 1 and 92.*

[131] J. Salmi. *Contributions to Measurement-based Dynamic MIMO Channel Modeling and Propagation Parameter Estimation*. PhD thesis, Helsinki University of Technology, http://lib.tkk.fi/Diss/2009/isbn9789522480194/isbn9789522480194.pdf, 2009. *Cited on page 1.*

[132] J. Salmi and A. F. Molisch. Propagation parameter estimation, modeling and measurements for ultrawideband MIMO radar. *IEEE Transactions on Antennas and Propagation*, 59(11):4257–4267, November 2011. *Cited on page 65.*

[133] J. Salmi, A. Richter, and V. Koivunen. Detection and tracking of MIMO propagation path parameters using state-space approach. *IEEE Transactions of Signal Processing*, 57(4):1538–1550, April 2009. *Cited on pages 13, 39, 57, 58, 65, and 66.*

[134] J. Salmi, A. Richter, and V. Koivunen. Sequential unfolding SVD for tensors with applications in array signal processing. *IEEE Transactions on Signal Processing*, 57(12):4719–4733, December 2009. *Cited on page 65.*

[135] A. H. Sayed and T. Kailath. A survey of spectral factorization methods. *Numerical Linear Algebra with Applications*, 8(6-7):467–496, 2001. *Cited on pages 84, 85, and 86.*

[136] R. O. Schmidt. Multiple emitter location and signal parameter estimation. *IEEE Transaction on Antennas and Propagation*, AP-34(3):276–280, March 1986. *Cited on page 82.*

[137] S. Sesia, I. Toufik, and M. Baker, editors. *LTE - The UMTS Long Term Evolution: From Theory to Practice*. John Wiley & Sons, Ltd., 591 pages, 2009. *Cited on page 1.*

[138] M. Shafi, M. Zhang, A. L. Moustakas, P. J. Smith, A. F. Molisch, F. Tufvesson, and S. H. Simon. Polarized MIMO channels in 3-D: models, measurements and mutual information. *IEEE Journal on Selected Areas in Communications*, 24(3):514–527, March 2006. *Cited on pages 39, 45, 57, and 66.*

[139] T. Shan, M. Wax, and T. Kailath. On spatial smoothing for direction-of-arrival estimation of coherent signals. *IEEE Transactions on Acoustics, Speech, and Signal Processing*, 33(4):806–811, August 1985. *Cited on page 31.*

[140] N. Sneeuw and R. Bun. Global spherical harmonic computation by two-dimensional Fourier methods. *Journal of Geodesy*, 70(4):224–232, January 1996. *Cited on pages 66, 67, and 68.*

[141] J. Sorelius, R. L. Moses, T. Söderström, and A. L. Swindlehurst. Effects of nonzero bandwidth on direction of arrival estimators in array signal processing. *IEE Proceedings - Radar, Sonar and Navigation*, 145(6):317–324, December 1998. *Cited on pages 12 and 82.*

[142] P. Stoica, E. G. Larsson, and A. B. Gershman. The stochastic CRB for array processing: A textbook derivation. *IEEE Signal Processing Letters*, 8(5):148–150, May 2001. *Cited on pages 87 and 117.*

[143] P. Stoica and R. L. Moses. *Introduction to Spectral Analysis*. Prentice-Hall, Inc., 313 pages, 1997. *Cited on pages 11, 17, 78, 81, and 96.*

[144] P. Stoica and A. Nehorai. MUSIC, maximum likelihood and Cramér-Rao bound. *IEEE Transactions on Acoustics, Speech, and Signal Processing*, 37(5):720–741, May 1989. *Cited on pages 16, 24, and 82.*

[145] P. Stoica and A. Nehorai. MUSIC, maximum likelihood and Cramér-Rao bound: further results and comparisons. *IEEE Transactions on Acoustics, Speech, and Signal Processing*, 38(12):2140–2150, December 1990. *Cited on page 78.*

[146] P. Stoica and A. Nehorai. Performance study of conditional and unconditional direction-of-arrival estimation. *IEEE Transactions on Acoustics, Speech, and Signal Processing*, 38(10):1783–1795, October 1990. *Cited on pages 16, 24, 78, and 87.*

[147] P. Stoica and Y. Selén. Model-order selection: A review of information criterion rules. *IEEE Signal Processing Magazine*, 21(4):36–47, July 2004. *Cited on pages 30, 45, 51, and 71.*

[148] P. Stoica and K. C. Sharman. Maximum likelihood methods for direction-of-arrival estimation. *IEEE Transactions on Acoustics, Speech, and Signal Processing*, 38(7):1132–1143, July 1990. *Cited on pages 6, 78, 81, and 86.*

[149] P. Stoica and K. C. Sharman. Novel eigenanalysis method for direction estimation. *IEE Proceedings F - Radar and Signal Processing*, 137(1):19–26, February 1990. *Cited on pages 6 and 86.*

[150] P. Stoica, Z. Wang, and J. Li. Extended derivations of MUSIC in the presence of steering vector errors. *IEEE Transactions on Signal Processing*, 53(3):1209–1211, March 2005. *Cited on page 27.*

[151] G. Strang. *Introduction to Linear Algebra*. Wellesley-Cambridge Press, third edition, 567 pages, 2003. *Cited on page 78.*

[152] P. Strobach. The recursive companion matrix root tracker. *IEEE Transactions on Signal Processing*, 45(8):1931–1942, August 1997. *Cited on page 85.*

[153] A. Swindlehurst and T. Kailath. A performance analysis of subspace-based methods in the presence of model errors - part I: the MUSIC algorithm. *IEEE Transactions on Signal Processing*, 40(7):1758–1774, July 1992. *Cited on pages 16, 20, 25, and 82.*

[154] A. Swindlehurst and T. Kailath. A performance analysis of subspace-based methods in the presence of model errors - part II: multidimensional algorithms. *IEEE Transactions on Signal Processing*, 41(9):2882–2890, September 1993. *Cited on pages 20, 25, and 82.*

[155] A. Swindlehurst and M. Viberg. Subspace fitting with diversely polarized antenna arrays. *IEEE Transactions on Antennas and Propagation*, 41(12):1687–1694, December 1993. *Cited on pages 15 and 16.*

[156] H. Teutsch and W. Kellermann. Acoustic source detection and localization based on wavefield decomposition using circular microphone arrays. *Journal of the Acoustical Society of America*, 120(5):2724–2736, November 2006. *Cited on pages 33 and 34.*

[157] A. H. Tewfik and W. Hong. On the application of uniform linear array bearing estimation techniques to uniform circular arrays. *IEEE Transactions on Signal Processing*, 40(4):1008–1011, April 1992. *Cited on page 34.*

[158] J. T. Toivanen, T. A. Laitinen, V. M. Kolmonen, and P. Vainikainen. Reproduction of arbitrary multipath environments in laboratory conditions. *IEEE Transactions on Instrumentation and Measurements*, 60(1):275–281, January 2011. *Cited on page 50.*

[159] J. T. Toivanen, T. A. Laitinen, and P. Vainikainen. Modified test zone field compensation for small-antenna measurements. *IEEE Transactions on Antennas and Propagation*, 58(11):3471–3479, November 2010. *Cited on pages 30, 50, and 52.*

[160] H. L. V. Trees. *Optimum Array Processing. Part IV of Detection, Estimation and Modulation Theory*. John Wiley & Sons, Inc., 1434 pages, 2002. *Cited on pages 76, 77, 79, 81, and 82.*

[161] M. Valkama, A. Springer, and G. Hueber. Digital signal processing for reducing the effects of RF imperfections in radio devices - an overview. In *Proceedings of the IEEE International Symposium on Circuits and Systems*, pages 813–816, 2010. *Cited on page 14.*

[162] B. V. Veen and K. M. Buckley. Beamforming: A versatile approach to spatial filtering. *IEEE Acoustics, Speech, and Signal Processing Magazine*, 5(2):4–24, April 1988. *Cited on pages 76, 77, 78, and 79.*

[163] M. Viberg, M. Lanne, and A. Lundgren. Calibration in array processing. In T. E. Tuncer and B. Friedlander, editors, *Classical and Modern Direction-of-Arrival Estimation*, chapter 3, pages 93–124. Academic Press, Burlington, MA, USA, 2009. *Cited on pages 18, 20, 23, 25, 28, 29, 72, 75, and 82.*

[164] M. Viberg and B. Ottersten. Sensor array processing based on subspace fitting. *IEEE Transactions on Signal Processing*, 39(5):1110–1121, May 1991. *Cited on pages 6, 24, 81, 86, and 87.*

[165] M. Viberg, B. Ottersten, and T. Kailath. Detection and estimation in sensor arrays using weighted subspace fitting. *IEEE Transactions on Signal Processing*, 39(11):2436–2449, November 1991. *Cited on page 87.*

[166] M. Viberg and A. L. Swindlehurst. Analysis of the combined effects of finite samples and model errors on array processing performance. *IEEE Transactions on Signal Processing*, 42(11):3073–3083, November 1994. *Cited on pages 20, 25, and 82.*

[167] M. Viberg and A. L. Swindlehurst. A Bayesian approach to autocalibration for parametric array signal processing. *IEEE Transactions on Signal Processing*, 42(12):3495–3507, December 1994. *Cited on pages 24 and 25.*

[168] S.A. Vorobyov, A. B. Gershman, and Z. Q. Luo. Robust adaptive beamforming using worst-case performance optimization: A solution to the signal mismatch problem. *IEEE Transactions on Signal Processing*, 51(2):313–324, February 2003. *Cited on pages 25, 26, 80, 81, and 89.*

[169] M. Wax and T. Kailath. Detection of signals by information theoretic criteria. *IEEE Transactions on Acoustics, Speech, and Signal Processing*, 33(2):387–392, April 1985. *Cited on page 17.*

[170] M. Wax and J. Sheinvald. Direction finding of coherent signals via spatial smoothing for uniform circular arrays. *IEEE Transactions on Antennas and Propagation*, 42(5):613–620, May 1994. *Cited on pages 33, 34, and 35.*

[171] M. Wax and I. Ziskind. Detection of the number of coherent signals by the MDL principle. *IEEE Transactions on Acoustics, Speech, and Signal Processing*, 37(8):1190–1196, August 1989. *Cited on page 17.*

[172] A. J. Weiss and B. Friedlander. Array shape calibration using sources in unknown locations - a maximum likelihood approach. *IEEE Transactions on Acoustics, Speech and Signal Processing*, 37(12):1958–1966, December 1989. *Cited on page 23.*

[173] A. J. Weiss and B. Friedlander. Direction finding for diversely polarized signals using polynomial rooting. *IEEE Transactions on Signal Processing*, 41(5):1893–1905, May 1993. *Cited on pages 82, 83, and 84.*

[174] A. J. Weiss and M. Gavish. Direction finding using ESPRIT with interpolated arrays. *IEEE Transactions on Signal Processing*, 39(6):1473–1478, June 1991. *Cited on page 31.*

[175] B. H. Wellenhof and H. Moritz. Introduction to spectral analysis. In Hans Sünkel, editor, *Lecture Notes in Earth Sciences - Mathematical and Numerical Techniques in Physical Geodesy*, volume 7, chapter Part A, pages 157–261. Springer-Verlag, 1986. *Cited on pages 39, 53, and 66.*

[176] Y. Wiaux, J. D. McEwen, P. Vandergheynst, and O. Blanc. Exact reconstruction with directional wavelets on the sphere. *Monthly Notices of the Royal Astronomy Society*, 388:770–788, August 2008. *Cited on page 72.*

[177] S. J. Wijnholds and A. J. van der Veen. Multisource self-calibration for sensor arrays. *IEEE Transactions on Signal Processing*, 57(9):3512–3522, September 2009. *Cited on page 1.*

[178] E. G. Williams. *Fourier Acoustics: Sound Radiation and Nearfield Acoustical Holography*. Academic Press, 296 pages, 1999. *Cited on page 34.*

[179] E. De Witte, H. D. Griffiths, and P. V. Brennan. Phase mode processing for spherical antenna arrays. *Electronics Letters*, 39(20):1430–1431, October 2003. *Cited on pages 32 and 35.*

[180] K. T. Wong, L. Li, and M. D. Zoltowski. Root-MUSIC-based direction-finding and polarization estimation using diversely polarized possibly collocated antennas. *IEEE Antennas and Wireless Propagation Letters*, 3(1):129–132, December 2004. *Cited on page 82.*

[181] J. Zhuang, W. Li, and A. Manikas. Fast root-MUSIC for arbitrary arrays. *Electronics Letters*, 46(2):174–176, January 2010. *Cited on pages 85 and 86.*

[182] I. Ziskind and M. Wax. Maximum likelihood location of multiple sources by alternating projection. *IEEE Transactions on Acoustics, Speech, and Signal Processing*, 36(10):1553–1560, October 1988. *Cited on page 24.*

[183] A. M. Zoubir, V. Koivunen, Y. Chakhchoukh, and M. Muma. Robust estimation in signal processing: A tutorial-style treatment of fundamental concepts. *IEEE Signal Processing Magazine*, 29(4):61–80, July 2012. *Cited on pages 18 and 25.*

Errata

Publication II

In eq. (21), the parameter vector $\boldsymbol{\xi}$ should be given by

$$\boldsymbol{\xi} = [\boldsymbol{\theta}^T, \boldsymbol{\phi}^T, \boldsymbol{\gamma}^T, \boldsymbol{\beta}^T, \boldsymbol{\rho}^T, \sigma_\eta^2]^T,$$

where $\boldsymbol{\rho}$ can be found in [142].

Aalto-DD 149/2013

ISBN 978-952-60-5346-2
ISBN 978-952-60-5347-9 (pdf)
ISSN-L 1799-4934
ISSN 1799-4934
ISSN 1799-4942 (pdf)

Aalto University
School of Electrical Engineering
Department of Signal Processing and Acoustics
www.aalto.fi

BUSINESS + ECONOMY

ART + DESIGN + ARCHITECTURE

SCIENCE + TECHNOLOGY

CROSSOVER

DOCTORAL DISSERTATIONS